

Advances in Civil Engineering

Advancements in Design, Analysis, and Retrofitting of Structures Exposed to Blast

Guest Editors: Chiara Bedon, Claudio Amadio, Li Chen, Vasant Matsagar, Frank Wellershoff, and Xihong Zhang





Advancements in Design, Analysis, and Retrofitting of Structures Exposed to Blast

Advances in Civil Engineering

Advancements in Design, Analysis, and Retrofitting of Structures Exposed to Blast

Guest Editors: Chiara Bedon, Claudio Amadio, Li Chen,
Vasant Matsagar, Frank Wellershoff, and Xihong Zhang



Copyright © 2016 Hindawi Publishing Corporation. All rights reserved.

This is a special issue published in “Advances in Civil Engineering.” All articles are open access articles distributed under the Creative Commons Attribution License, which permits unrestricted use, distribution, and reproduction in any medium, provided the original work is properly cited.

Editorial Board

Maria Cruz Alonso, Spain
Serji N. Amirkhanian, USA
Panagiotis Anastasopoulos, USA
Pedro Arias-Sánchez, Spain
Rafik Belarbi, France
Andrea Benedetto, Italy
William Burgos, USA
Alberto Campisano, Italy
Francesco Canestrari, Italy
Daniel Castro Castro-Fresno, Spain
Noel Challamel, France
Ghassan Chehab, Lebanon
Ottavia Corbi, Italy
Gianmarco de Felice, Italy
Luigi Di Sarno, Italy

Slobodan Djordjevic, UK
Ahmed Elghazouli, UK
Giovanni Garcea, Italy
Kirk Hatfield, USA
John Mander, USA
Giuseppe Carlo Marano, Italy
Christian Mittelstedt, Germany
Hossein Moayedi, Iran
Fabrizio Mollaioli, Italy
Ayman S. Mosallam, USA
Giuseppe Oliveto, Italy
Alejandro Orfila, Spain
Togay Ozbakkaloglu, Australia
Alessandro Palmeri, UK
Ram M. Pendyala, USA

Arnaud Perrot, France
Christophe Petit, France
Sertong Quek, Singapore
Dimitris Rizos, USA
Hamid Ronagh, Australia
Pier Paolo Rossi, Italy
Anna Saetta, Italy
Halil Sezen, USA
Alexandru Sheremet, USA
Sanjay Kumar Shukla, Australia
Claudio Tamagnini, Italy
Yaya Tan, China
Cumaraswamy Vipulanandan, USA
Wei-Chau Xie, Canada
Jianqiao Ye, UK

Contents

Advancements in Design, Analysis, and Retrofitting of Structures Exposed to Blast

Chiara Bedon, Claudio Amadio, Li Chen, Vasant Matsagar,
Frank Wellershoff, and Xihong Zhang
Volume 2016, Article ID 1345478, 2 pages

Blast Protection of Unreinforced Masonry Walls: A State-of-the-Art Review

Lucas Lantz, Joshua Maynez, Wesley Cook, and Claudia Mara Dias Wilson
Volume 2016, Article ID 8958429, 11 pages

Experimental Study of the Effectiveness of Sacrificial Cladding Using Polymeric Foams as Crushable Core with a Simply Supported Steel Beam

H. Ousji, B. Belkassem, M. A. Louar, B. Reymen, L. Pyl, and J. Vantomme
Volume 2016, Article ID 8301517, 13 pages

Modelling Blast Effects on a Reinforced Concrete Bridge

Markellos Andreou, Anastasios Kotsoglou, and Stavroula Pantazopoulou
Volume 2016, Article ID 4167329, 11 pages

Bioinspired Design of Building Materials for Blast and Ballistic Protection

Yu-Yan Sun, Zhi-Wu Yu, and Zi-Guo Wang
Volume 2016, Article ID 5840176, 6 pages

Design of Blast-Loaded Glazing Windows and Facades: A Review of Essential Requirements towards Standardization

Martin Larcher, Michel Arrigoni, Chiara Bedon, J. C. A. M. van Doormaal, Christof Haberacker,
Götz Hüsken, Oliver Millon, Arja Saarenheimo, George Solomos, Laurent Thamie, Georgios Valsamos,
Andy Williams, and Alexander Stolz
Volume 2016, Article ID 2604232, 14 pages

Advanced Concrete Model in Hydrocode to Simulate Concrete Structures under Blast Loading

Guo Hu, Jun Wu, and Liang Li
Volume 2016, Article ID 7540151, 13 pages

Editorial

Advancements in Design, Analysis, and Retrofitting of Structures Exposed to Blast

**Chiara Bedon,¹ Claudio Amadio,¹ Li Chen,² Vasant Matsagar,³
Frank Wellershoff,⁴ and Xihong Zhang⁵**

¹*University of Trieste, Trieste, Italy*

²*PLA University of Science and Technology, Nanjing, China*

³*Indian Institute of Technology, Delhi, India*

⁴*HafenCity University, Hamburg, Germany*

⁵*Curtin University, Perth, WA, Australia*

Correspondence should be addressed to Chiara Bedon; bedon@dicar.units.it

Received 31 August 2016; Accepted 31 August 2016

Copyright © 2016 Chiara Bedon et al. This is an open access article distributed under the Creative Commons Attribution License, which permits unrestricted use, distribution, and reproduction in any medium, provided the original work is properly cited.

The objective of this special issue is to provide an overview on the current trends and recent advancements in terms of design, analysis, experimental testing, and retrofitting of structural systems and assemblies exposed to exceptional loads such as explosions.

Protection of constructed facilities from damaging natural hazards and exceptional loads, as known, has recently become an important issue in common practice. Besides the generalized goal of protective constructions to minimize injuries and improve the probability of survival of people, after the bombing of the Oklahoma Federal Building (1995), the blast design of structures has become a fundamental requirement, so that most of the actual strategic buildings and infrastructures must guarantee appropriate levels of blast resistance. Compared to quasistatic ordinary loads or conventional hazards such as wind gusts, earthquakes, floods, or moderate impacts, blast events are typically characterized by a large-scale, extremely rapid, and sudden release of energy, generally in the order of thousandths of seconds or milliseconds. As a result, specific design methods and advanced computational models able to properly include the effects of several aspects, like high strain rates, nonlinear inelastic material behaviors, and time-dependent deformations, are strictly required. The vulnerability assessment of a given structure exposed to explosive events, moreover, should properly take into account the interaction of the assigned blast wave and the

targeted system, as well as the uncertainties implicitly related to the blast pressure description.

Finite-Element (FE) and Computational Fluid Dynamics (CFD) numerical simulations, in this sense, can represent the first tool for the dynamic analysis of a given structural assembly under air blast waves, as alternative to time and cost consuming far field or laboratory experimental tests. The implementation of both the numerical approaches, however, could result in being particularly difficult in the case of complex structural configurations. Several key input parameters, moreover, are strictly required in them for accurate estimations and appropriate risk analyses.

In some cases, special retrofitting techniques, as well as the implementation of novel passive/active control systems, could be also required to guarantee appropriate levels of resistance in a given assembly subjected to blast events, especially in the case of existing buildings or extremely vulnerable structural typologies.

A multidisciplinary approach, including fluid-structure interaction theories, material sciences concepts, and technological innovation, is thus essential.

The revised papers sent for production and included in the final special issue booklet are related to various topics, such as the blast performance of reinforced concrete structures and bridges, as well as masonry systems or structural glass windows and facades. Careful consideration is also paid

for the performance of special materials under blast impacts, such as polymeric foams or bioinspired materials able to act as protective coatings during explosive events. Additional details and information on the published papers are provided in the following paragraphs.

In the paper by L. Lantz et al., a detailed state-of-the-art review on the actual possibilities for the blast protection of unreinforced masonry walls is presented. Careful consideration, based on some recent literature contributions, is given both to the current mitigation techniques and to the available experimental testing methods for the assessment of the blast vulnerability and resistance of masonry structures. Possible solutions including fiber reinforced polymer (FRP) composites and polyuria, as well as steel sheets or aluminum foams, are then critically discussed.

M. Andreou et al. investigated the blast effects on a two-span, reinforced concrete bridge representative of a highway overpass. The dynamic response of the bridge under a near distance explosive event is first deeply investigated by means of a refined, full three-dimensional numerical model. A simplified, practical to use, modelling methodology is then proposed as a useful tool for a rational but fast evaluation of blast effects on structures. The potential of such simplified approach is emphasized by application to the reinforced concrete bridge object of study.

Attention to the numerical investigation of concrete structures under blast loads is also given by G. Hu et al., with careful consideration for the blast performance of multilayer concrete slabs. The numerical investigations are carried out via computationally advanced and refined three-dimensional models implemented in the hydrocode AUTODYN. Based on parametric numerical investigations and validation towards experimental test results, the potentials and limits of the RHT concrete model are emphasized in the paper. Modified input parameters are also proposed for the same RHT method, in order to obtain a more realistic postpeak softening behavior for concrete under tension and compression.

Numerical models, as known, represent in current practice a high potential for researchers and designers, since allowing simulating even mechanical and geometrical complex structural systems and assemblies under a multitude of boundary and loading conditions. As such, however, careful attention should be given to several aspects, first of all, especially in the case of explosive loads, the implemented damage models for materials, but also the boundary conditions and any possible mechanical interaction between the model components. These topics, if not properly addressed, can result in misleading and even unsafe results, especially in case no provisions or recommendations are provided to design practitioners and software users.

In this regard, the paper by M. Larcher et al. focuses on the design of blast resistant structural glass windows and facades, with careful attention for the role and the requirements of numerical models for such systems. The paper attempts to give a first idea of a possible standardization concerning numerical simulations. Attention is drawn to the representation of the blast loading and to the proper description of the behavior of the material of the mentioned products, to the geometrical meshing of the model components, and to

the modelling of the connections between the glazing system components and between the glass façade and the structural background. The current need to validate such numerical models against reliable experimental test data, some of which are indicated, is also underlined.

Two of the published papers are finally related to research projects aimed at exploring the potential and feasibility of innovative materials able to act as protective coatings for structures and buildings subjected to explosive loads. In the paper from H. Ousji et al., for example, an extended experimental investigation is carried out on sacrificial cladding composed of three different types of polymeric foams (i.e., expanded polystyrene foam, closed-cell polyurethane, and open-cell polyurethane). These foams are expected to be introduced between the main structures and a front plate, so that the crushable core could work as active sacrificial cladding able to protect the main structures themselves. The experimental tests are critically discussed, giving some useful provisions in terms of performance of such foams and highlighting the potential/limits of the explored solutions.

Y. Sun et al., finally, present a review paper aimed at providing state of the art on the mechanisms behind the performance of abalone nacre under several loading conditions, including shear, uniaxial tension, compression, and bending. When used in abalone shells as inner layer, nacre exhibits typically high stiffness and toughness properties, hence suggesting the development of bioinspired building materials able to provide excellent performances under impact loads. This potential is also emphasized on the base of experimental test results. A successful application, in particular, is expected in cement-based and clay-based composite materials.

In conclusion, some final considerations on the full special issue project are given.

Acknowledgments

First of all, all the authors are gratefully acknowledged for their active contribution to the call for papers. The hope is that the readers could find fruitful and high quality research topics in the published papers. Peer reviewers, in this regard, have a key role in the collection of advancing, high quality scholarly journals. As such, the guest editors of the special issue would like to extend special thanks to the reviewers who carefully read all the submitted articles. Their observations and comments represented a great support, both to the authors, to improve the quality of the original papers, and to the guest editors, to make objective decisions with regard to the excellence of the submitted research papers. A final acknowledgement is also extended by the Lead Guest Editor, Dr. Bedon, to the full team of guest editors, for the support provided in the last months through the full process of submission and promotion of the call for papers, up to the publication of the special issue booklet in the journal.

Chiara Bedon
 Claudio Amadio
 Li Chen
 Vasant Matsagar
 Frank Wellershoff
 Xihong Zhang

Review Article

Blast Protection of Unreinforced Masonry Walls: A State-of-the-Art Review

Lucas Lantz, Joshua Maynez, Wesley Cook, and Claudia Mara Dias Wilson

Civil and Environmental Engineering Department, New Mexico Institute of Mining and Technology, 801 Leroy Pl., Socorro, NM 87801, USA

Correspondence should be addressed to Claudia Mara Dias Wilson; cwilson@nmt.edu

Received 23 April 2016; Revised 2 August 2016; Accepted 16 August 2016

Academic Editor: Chiara Bedon

Copyright © 2016 Lucas Lantz et al. This is an open access article distributed under the Creative Commons Attribution License, which permits unrestricted use, distribution, and reproduction in any medium, provided the original work is properly cited.

The recent rise of terrorist attacks has reinforced the need for mitigation of damage caused by blast loading on unreinforced masonry walls. The primary goal of the techniques is to prevent the loss of life while simultaneously preserving the integrity of the structure. This paper presents a compilation of recently available literature on blast protection of unreinforced masonry walls. It seeks to present the state of the art in this field, including mitigation techniques considered as well as testing methods selected. Fiber reinforced polymers and polyurea are the two dominant retrofitting techniques being assessed in the field. Other techniques include but are not limited to polyurethane, steel sheets, and aluminum foam. Since there is no widely implemented standard for blast loading test procedures, direct comparisons between the efficiencies of the mitigation techniques proposed are not always feasible. Although fragmentation is an indicator of the efficiency of retrofits, it is currently measured by subjective observation of postblast debris.

1. Introduction

Recurring individual terrorist attacks and accidental explosive incidents can be cited in the western world such as Texas (2005), London (2005), Connecticut (2010), and Boston (2013) as a reason for a push in blast resistant research of civilian structures. In 2010 alone, there were 13,186 terrorist attacks worldwide [1]. Generally, terroristic acts attempt to cause the most amount of physical and psychological damage to the people present and to the populace as a whole while accidental explosions can undermine the safety of nearby occupants. Therefore, most retrofitting and design techniques aim to diminish the effectiveness of attacks by reducing injury and loss of life or improving safety for occupants. Fragmentation of elements in or as part of a structure is considered “hazardous” by ASCE 51-11 [2] and is assigned the lowest level of performance. Since fragmentation is generally the most deadly part of a blast event [3], aside from building collapse, it is often a key part of the analysis when judging the effectiveness of a retrofit technique. Finding the most cost-effective method to reduce the fragmentation of buildings could be a benefactor for both the industrialized and the developing parts of the globe.

Due to the recent rise of terrorist attacks globally, the purpose of this research is to inform engineers and scientists of the current design and retrofit techniques available for unreinforced masonry. This paper will address the types of retrofitting techniques for unreinforced masonry walls currently being researched in roughly the last 15 years. Buchan and Chen [4] and Malvar et al. [5] conducted state-of-the-art reviews in 2007 related to the topic and most reviewed investigations herein were published at a later date. Reinforced masonry is less susceptible to fragmentation and as a result this study focuses on unreinforced masonry.

This paper reviews the materials investigated, experimental components, numerical simulations, and fragmentation mitigation.

2. Materials Descriptions

A search of the literature in the past 15 years showed that the most prevalent types of retrofitting techniques for unreinforced masonry walls include fiber reinforced polymers and polyurea, with polyurethane, steel sheets, aluminum foam, and engineering cementitious composites all being investigated as well. An overview of these techniques is presented in the following.

2.1. Fiber Reinforced Polymers. Fiber reinforced polymers (FRP) are composite unidirectional fabrics in a matrix which are attached to the surface of the masonry wall usually with epoxy or resin. The fibers add strength to the wall by preventing out-of-plane bending and shear. FRP increases the strength and ductility of the structure while limiting the amount of flying debris. Several different studies have addressed the use of FRP for blast protection of masonry walls in the past 15 years [6–8, 13–19]. Derivatives to FRP are carbon fiber reinforced polymer (CFRP) and glass fiber reinforced polymer (GFRP).

2.2. Polyurea. Polyurea is an elastomer commonly used in a variety of applications for its water, abrasion, and chemical resistance. Polyurea appears to be an effective retrofitting technique because it usually reduces the fragmentation of the masonry wall [9, 10, 12, 14, 20–22]. Generally, researchers chose to apply it as a spray-on material to the interior face of the wall. As of 2016, more recent studies appear to favor finite element estimations or comparisons of the wall's reaction. Polyurea's performance can be adjusted by the use of certain additives [21].

2.3. Polyurethane. Polyurethane is a material that is similar chemically to polyurea, but it comes in a variety of different forms such as a spray-on adhesive and a thin film. Recently, little has been done to evaluate its effectiveness as a retrofit technique.

2.4. Steel Sheets. Steel sheets are another potential retrofitting technique for masonry walls. However, steel sheets are laborious to install, add substantial dead load to the wall, and significantly increase cost [4]. For these reasons, FRP sheets and aluminum foam sheets are considered more attractive alternatives.

2.5. Aluminum Foam. Aluminum foam is a lightweight solid material retaining a lot of aluminum's original properties such as corrosion resistance and strength. Aluminum foam is a promising retrofit material because of its early onset of plastic deformation which allows it to dissipate blast load energy [23].

2.6. Engineered Cementitious Composites. Engineering cementitious composites (ECC) are mixtures of typical concrete ingredients in addition to a small amount of fiber. ECC has good strength and ductility characteristics in addition to high fracture toughness. Variations of ECC have shown the ability to absorb high energy impacts [22]. These characteristics have made ECC a possible candidate for increasing masonry's resistance to blast loading.

3. Experimental Investigations

3.1. Fiber Reinforced Polymers. Urgessa and Maji [13] conducted a study with eight masonry walls. Four of the eight walls were reinforced with an inorganic matrix containing a liquid potassium silicate solution and an amorphous silica powder. Two of the walls had two layers and the other two

TABLE 1: Approximate deflections [6].

Wall	Displacement (mm)
CM1R	0.8
CM1L	0.8
CM3L	0.8
CM4R	1.2
CM4L	1.2
CM5R	1.8
CM5L	0.5
CM6R	1.0
CM6L	1.1

had four layers. The remaining four walls were reinforced with a thixotropic epoxy resin and a 2 : 1 hardener. Both mixes were applied to the walls as FRP sheets. Again, two walls had two layers and two walls had four layers. Each of the eight walls was subject to a blast load of 0.45 kg booster which is equivalent to 0.64 kg TNT. The walls were set up in a circle around the blast source with a radius of 1.83 m. The walls with two layers experienced displacement ranging from 14.5 to 18.8 cm. Large horizontal cracks formed along most of the mortar joints. The walls with four layers experienced displacement of 10.0 cm to 12.9 cm. No visible cracks were seen and fragmentation was contained in all tests.

Tan and Patoary [6] applied a 20.92 GJ (5-ton TNT) blast to three masonry walls and a 112.97 GJ (27-ton TNT) blast to three additional masonry walls. Walls subject to a 112.97 GJ blast were anchored to the ground surface and walls subject to the 20.92 GJ blast were not anchored. Each of these tests was performed three times for a total of eighteen masonry walls. The distances of the test are shown in Figure 1. Each set of walls was assigned a module number in the form of "CM" followed by the wall number. Additionally, "R" and "L" are added to the end to denote which of the walls was being addressed. For example, CM1R refers to the first wall set and the right wall in that particular set. The varying use of carbon FRP, glass FRP, woven roving, and stiffeners can be seen in Figure 1 and the approximate results based on the graphs presented by Tan and Patoary [6] can be seen in Figure 1 and Table 1, respectively.

Some of the walls were designed to experience plastic deformation. However, each of the walls tested showed no visible signs of cracking or delamination and each wall was considered successful. Based on the results presented in Table 1, it can be inferred that glass FRP and woven roving had similar effectiveness.

Baylot et al. [14] conducted a 1/4-scale model of a 1 mm thick glass FRP attached to the back face of a masonry wall. The wall was subject to varying magnitude and distances of the charge. Though the wall became detached from the frame and experienced mortar joint cracking, the wall was still considered a success because the wall remained intact and upright. This particular experiment was unique in that it measured the effectiveness of the retrofit by reading the velocity of the flying debris. Though the FRP did aid in limiting the amount of debris, this method of comparing

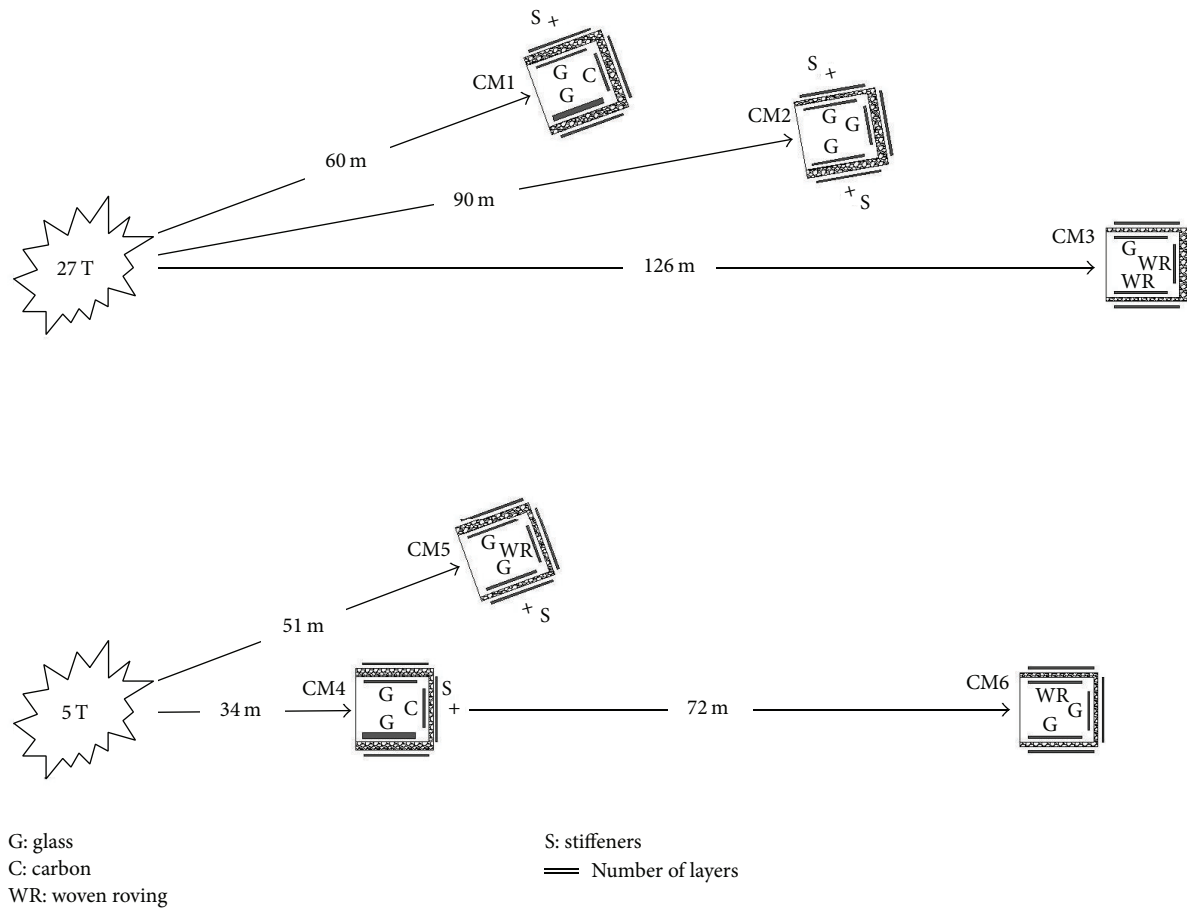


FIGURE 1: Tan and Patoary's [6] test setup.

the velocities was not as effective at indicating the degree of hazard as was originally assumed.

Stanley et al. [7] used two-part spray-on polyurea along with aramid FRP. This test was successful, containing all of the debris. The maximum deflection of the wall was approximately 230 mm. As seen in Figures 2(a) and 2(b), the left wall was the control and had no retrofitting. The wall to the right was the wall reinforced with polyurea and aramid FRP.

Stratford et al. [15] attached glass FRP sheets to clay brick walls and concrete masonry unit walls. The sheets were applied in both the horizontal and the vertical directions to increase the shear strength of the wall. The walls were subject to a prestressed load of 100 kN in the vertical (compressive) direction. The horizontal load was increased in 50 kN increments. The maximum load applied to the clay brick wall and concrete unit wall was 195 kN and 130 kN, respectively.

The corresponding maximum deflections were 1.4 cm and 1.3 cm. Both walls displayed rapid cracking under the load along the mortar joints. Debonding of the fabric from the wall also occurred at some locations along the walls.

Alsayed et al. [16] used $200 \times 200 \times 400$ mm hollow concrete masonry units to construct walls within a 2.1 m long by 1.5 m high reinforced concrete frame. Six masonry walls were included in the experimental procedures, three of which were reinforced with 1.85 mm thick GFRP sheets placed in orthogonal directions. The other three walls were unreinforced. The tests included three different sized charges placed at different distances from the wall: 1.134 kg, 4.8 m; 49.9 kg, 4.8 m; and 14.2 kg, 2.0 m, respectively. Each test used one unreinforced masonry wall and one GFRP reinforced wall. All charges were set off at a height of 0.75 m above the ground. To judge the effectiveness of the retrofit, Alsayed et al. [16] used Department of Defense Minimum Antiterrorism Standards for Buildings' four levels of damage [3]. Both of the walls affected by the 1.134 kg blast showed no damage and were given a protection rating of high. For the 49.9 kg blast, both walls were given a protection rating of medium but showed different types of damage. The unreinforced wall had light damage with blocks pushed out along with minor detachment at the wall-frame interface. The reinforced wall showed debonding at both the wall-frame interface and the

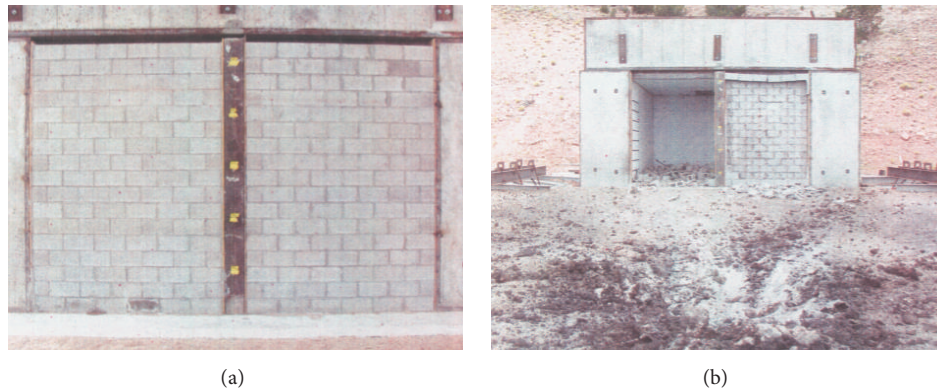


FIGURE 2: Stanley et al.'s [7] blast test (a) before blast test and (b) after blast test.

FRP-frame interface. For the 14.2 kg charge, both walls failed but were graded differently because the GFRP reinforced wall prevented flying debris. The unreinforced wall was given a protection level of very low and the reinforced wall was given a protection level of low. GFRP reinforced masonry walls were concluded to show potential as a retrofit technique and were considered to be effective in preventing fragmentation.

Bui and Limam [17] considered two-way bending of unreinforced masonry due to vertical loads and lateral loads (pressures) for which blast loading can be conjectured. The experiments used hollow concrete blocks sized $20 \times 20 \times 50$ cm to construct the four test wall setups. From the top view, three walls form to make a U with only straight lines. The bottom of the U is the main wall: it is 2.9 m long and 2.0 m tall. The adjacent side walls are 1.0 m long and 2.0 m tall. Two different types of foundation were used for the walls. Wall 1's foundation slab was U-shape dimensioned at $310 \times 120 \times 20$ cm while Walls 2–4 had a rectangular slab sized $350 \times 185 \times 25$ cm. Walls 3 and 4 were retrofitted with a CFRP composite but the amount of CFRP was different. Wall 3 used 7 vertical CFRP strips and 6 horizontal CFRP strips that were 20 mm wide and 2 m long. Wall 4's strips were only 7.5 mm wide. The static pressure on the wall was increased until the displacement of the wall reached 50 mm. The CFRP reinforced walls had noticeable increases in bearing capacity. Wall 4 reached a capacity of 90 kN/m^2 and Wall 3 reached a capacity of 140 kN/m^2 in comparison to unreinforced Wall 2's capacity of 58 kN/m^2 . Wall stiffness was analyzed as the slope of the pressure displacement curve. When the curve became nonlinear, it signaled the development of cracks and their growth. The CFRP improved the walls stiffness and prevented cracks from developing. Walls 1, 2, and 4 had similar main wall crack patterns: vertical cracks in the center of the wall and diagonal cracks forming from the lower corner of the main wall. Wall 3, however, only had small cracks on the main wall. Wall 4 and Wall 3 saw cracks on the adjacent walls because of the flexural bending in the main wall. Bui and Limam [17] concluded that together the walls show that simply supported walls perform better than walls with real boundary conditions and more research under realistic boundary conditions must be conducted in order to properly evaluate the effectiveness of the CFRP retrofit.

Chen et al. [18] conducted 6.5-scale blasting tests on 1.5 m high \times 2 m wide \times 0.2 m thick walls. MU15 P type porous bricks sized 90 mm width \times 90 mm height \times 190 mm length were used to construct the walls. The TNT charge size used on the walls ranged from 0.2 to 34.2 kg. The scaled standoff distance ranged from 1.81 to $10 \text{ m/kg}^{1/3}$. Three types of retrofit material were examined in blast tests: CFRP, steel wire mesh, and steel bars. CFRP strips with a thickness of 1.2 mm and a width of 30 mm were bonded with an epoxy adhesive to the back of the wall in the horizontal and vertical directions. Steel wire mesh was attached to the back of the masonry wall with nails followed by a 10 mm layer of plastered mortar. Steel bars with a 2 mm thickness and 30 mm width were bonded with nails and epoxy adhesive on the back side of the wall. Eight pressure gauges were arranged on the front of the masonry to record measurements. All three retrofitting techniques improved the performance of the wall. Under 3.9 kg, unreinforced masonry walls saw residual displacement of about 3 mm at the center of the wall while the CFRP, steel wire mesh, and steel bar reinforced walls saw 1 mm or less of displacement. Likewise, the retrofitting techniques had about 3 mm of maximum displacement, in comparison to the 6 mm of maximum displacement in the unreinforced walls. Chen et al. [18] noted that the effectiveness of the retrofitting techniques increased with higher charge weights. The CFRP strip retrofitting reduced the residual displacement the most out of any of the retrofitting techniques, reducing displacement by 92%. In comparison, the steel mesh reduced the residual displacement by 67%. Under visual inspection, the walls told a reverse story other than the displacement. The CFRP retrofitted walls had some shear rupture delamination while the steel mesh only had little spallation of the concrete. While all retrofitting materials were able to reduce the scattering of fragments, it was clear that the CFRP and steel bar retrofitting techniques were more damaged than the steel mesh. The steel mesh was therefore concluded to be the most efficient retrofitting technique.

Hamed and Rabinovitch [19] used $400 \times 200 \times 200$ mm concrete masonry units to construct 2 masonry walls 1230 mm wide by 2100 mm tall. Walls were enclosed in a 1.5 m by 2.5 m steel frame and rested upon a reinforced concrete base beam. CFRP was chosen as the retrofit material. The

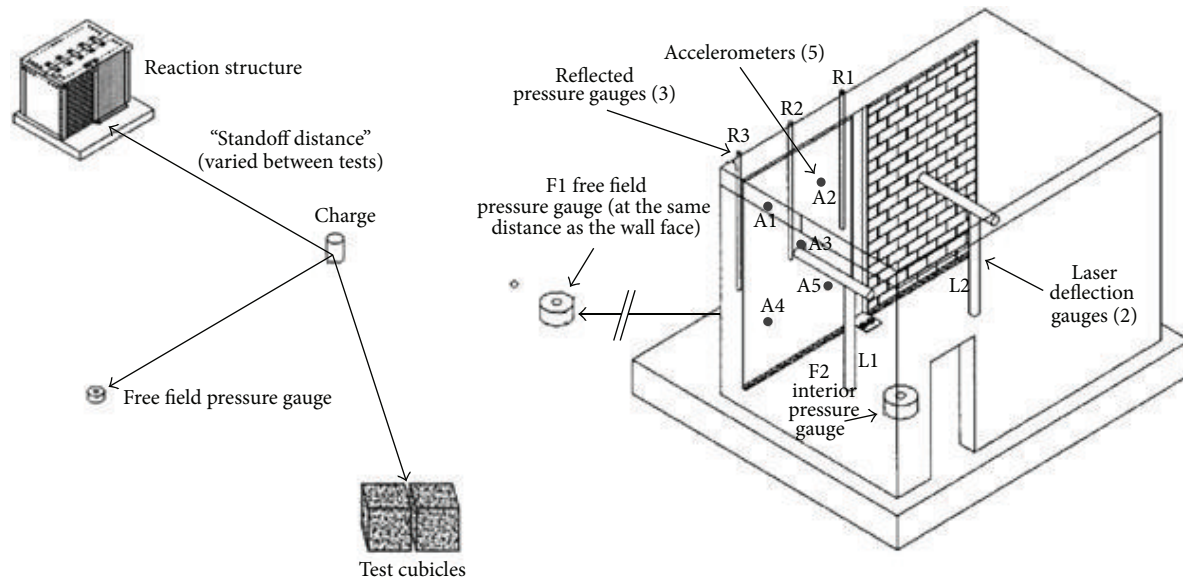


FIGURE 3: Full-scale masonry wall test setup [8, 9].

CFRP strips applied to the wall were 50 mm wide and 1.2 mm thick. CFRP was attached to the walls by applying 3 mm of epoxy to the wall and 2 mm of epoxy to the CFRP strips. The epoxy sides were then attached to each other and allowed to cure for 10 days. The loads applied were two out-of-plane knife-edge loads created by 300 kN hydraulic jack. One wall was a control wall with no reinforcement and the other was reinforced with CFRP. The CFRP wall failed at 1.25 times the load of the unreinforced wall. The behavior of the CFRP and unreinforced wall was different leading up to failure. The unreinforced wall showed a nonlinear behavior in regard to a load-deflection curve while the CFRP reinforced wall did show a linear behavior up to failure. Likewise, the CFRP reinforced wall had 1/3 of the deformation at the point of failure compared with the control wall. The unreinforced wall failed suddenly and was classified as a total collapse failure. The sudden collapse of the unreinforced wall could have been because of the crushing of the masonry units, a shear failure, or both but could not be pinpointed by Hamed and Rabinovitch [19]. Likewise, the cause of failure for the reinforced wall was also hard to determine. Hamed and Rabinovitch [19] gave two possible reasons: debonding of the free edges of the CFRP and shear failure of the masonry units. Although the CFRP did increase the strength of the wall, Hamed and Rabinovitch [19] noted that the increase was smaller than that in other literature, most likely because of the more realistic supporting conditions.

3.2. Polyurea. Davidson et al. [8] judged 21 different polymers that included seven thermoplastic sheets, one brush-on polymer, and 13 spray-on polymers. Out of all the materials, pure polyurea spray-on materials were chosen for their strength, cost, stiffness, ductility, and resistance to fire. This first test had three masonry walls, two of which had polyurea applied only to the interior side of the wall, and the other had polyurea

applied to both sides. The size of the charge was not reported due to sensitivity of the subject. When the treated walls were compared to their unreinforced control counterpart, all of the retrofitted walls appeared to be able to reduce fragmentation well. It is noted that this is most likely due to the polyurea's ability to absorb strain energy, bond to the surrounding structure, and bond to the wall itself. These tests also showed that the walls' mechanism of failure was affected by the support conditions, peak pressure, and duration.

Davidson et al.'s [9] follow-up study addresses complications encountered in the earlier tests. Twelve walls with varying dimensions in the range 2.4 m–3.7 m × 2.3 m–4.9 m were subjected to explosive loads. The test setup is seen in Figure 3. Similar to Davidson et al.'s [8] study, polyurea systematically increased the resistance of the walls to blast loading but some specific behavioral mechanisms were noted on the polyurea walls: (1) stress waves traveled throughout the wall and caused fracture, (2) the direct impact of the blast load caused some immediate fracture, (3) tearing of the polyurea coating occurred near the supports, (4) the front face of the wall suffered fracture due to flexure, (5) the polyurea reinforcement tore under flexure, and (6) the system collapsed when the polyurea tore or lost its adhesive properties to the exterior structure. Individual masonry blocks were placed at different distances and were subjected to the same blast. Notably, a change in distance of roughly 61 centimeters caused notable changes in the blocks ability to resist the blast.

Johnson et al. [20] conducted a study involving two sets of masonry walls in evaluation. The first set of full-scale walls used three different retrofitting techniques, all of which used polyurea as part of the reinforcement. The first used spray-on polyurea in combination with aramid fabric, the second used trowel on polyurea alone, and the third used trowel on polyurea as an adhesive for thermoplastic film.



FIGURE 4: POSS-reinforced wall (a) at maximum deflection and (b) in the final stage [10, 11].

Only dynamic tests were done on full-scale walls. The other set of walls was scaled down by a quarter and had seven different types of retrofit systems applied. This set of walls was evaluated using both scaled static and dynamic tests. Of the seven types, one used spray-on polyurea as the primary retrofitting technique, one used trowel on polyurea with aramid fabrics as additional reinforcement, three more used spray-on polyurea in combination with the aramid fabrics, and the other two did not use polyurea. Johnson et al. [20] had a few main conclusions from the test. First, the static load tests closely resemble the dynamic results for quarter-scaled masonry walls. Also, the quarter-scaled masonry walls performed similarly to the full-scale walls, implying that using scaled masonry walls to judge the effectiveness of a full-scale wall is acceptable. Every type of retrofitting technique appeared to reduce the amount of debris during loading. The unreinforced retrofit systems increased ultimate flexural resistance in comparison to nonretrofitted walls by a factor of 1.9 to 4.0, while the aramid reinforced system increased the ultimate flexural resistance by a factor of 5.5 to 7.5. This implies that using the polyurea in combination with the aramid fabric was the most effective retrofitting technique in terms of ultimate flexural resistance.

Baylot et al. [14] also did 1/4-scale tests using spray-on polyurea. The polyurea was applied to the interior face of the masonry walls at a thickness of 3.2 mm. As previously stated, walls were subject to varying magnitude and distances of the charge in order to get the desired level of peak pressure and impulse. The polyurea was successful at keeping the majority of the debris (interpreted as fragmentation) out of the structure during the blast event. Therefore, polyurea was considered a successful retrofitting technique because it reduced the hazard behind the masonry wall.

Irshidat et al. [10] compared three different polyurea mixes. One is an unreinforced standard polyurea, one is reinforced with exfoliated graphene nanoplatelets (XGnP), and the other is reinforced with polyhedral oligomeric silsesquioxane (POSS). The test used scaled down masonry blocks sized $54 \times 57 \times 115$ mm. The wall was 16 blocks high

and 12 blocks long. The U.S. Army Engineer Research and Development Center's blast simulator was used to perform dynamic tests on each of the wall types. The unreinforced polyurea wall experienced a tensile failure at a blast peak pressure of 208.22 kPa. The XGnP-reinforced wall had a primary horizontal crack form at the peak pressure of 224.91 kPa. The crack caused the wall to split into two pieces and collapse. The POSS retrofitted wall had shear damage and horizontal cracks at its peak pressure of 218.91 kPa. Conclusions were primarily based on isodamage pressure-impulse curves that encompassed all of the tests. Although Irshidat et al. [10] specifically noted that XGnP-reinforced wall's retrofitting system was effective at reducing fragmentation in the blast and the POSS retrofitted wall can be seen to have no fragments in it (Figure 4), Irshidat et al. [10] concluded by saying that fragmentation was not addressed. This is most likely because the blast simulator, like static or other tests, does not cause the same amount of fragmentation on impact as a real explosive.

Wang et al. [12] performed explosive tests on 6 walls, 4 of which were constructed out of $24 \times 11.5 \times 5.3$ cm clay bricks. The other 2 were constructed out of $20 \times 20 \times 60$ cm aerated concrete blocks. Clay walls were 3.6 m wide by 2.8 m tall and the concrete walls were 2.4 m wide by 2.2 m tall. Two gauges were used to measure the peak pressure and impulse due to the blasts on the wall. The first gauge was placed at the center of the wall and the second was placed at a distance of one-fifth of the walls width away from the first gauge. Some of the key statistics are included in Table 2. Note that the burst height for every test was 1.4 m and the standoff is the distance between the charge and the wall. In general, the polyurea retrofitted walls appeared to perform much better than the retrofitted walls. Wang et al. [12] concluded that this was because (a) initial cracking occurred before collapse; (b) the impact force in the reinforced wall was 18 times higher in the aerated brick and 4 times higher in the clay brick; (c) the face of the walls did not fracture. The failure modes were different between the reinforced clay brick walls and the aerated masonry walls. The unreinforced clay masonry wall

TABLE 2: Failure criteria [12].

Test charge weight (kg)	Charge size (kg)	Standoff (m)	Thickness (mm)	Failure criteria
Test 1: Y2	2	1	0	Control wall severely collapsed above burst height without front face fracture.
Test 2: TQ-Z-J-D-5	5	1.0	3 (partially)	Wide crack propagated completely the thickness of the wall with large deformation. The polyurea layer is intact with some tensile strain marks.
Test 3: TQ-Z-J-2-4	8	1.0	3 (fully)	The initial crack occurred at the center of the top without deformation.
Test 4: TQ-Z-J-1	20	1.0	3 (fully)	The wall rotated about bottom and severely collapsed due to overload. Polyurea was torn and separated completely from the front face.
Test 5: TQ-Q-W-2	5	10	0	The wall presented mortar joint separation and would reach the critical state of collapse due to large deformation.
Test 6: TQ-Q-J-2	5	3.0	3 (fully)	The wall underwent large deformation with side parts warping and disengaging from columns. There was no tearing of the polyurea.

failed because of the separation of brick and mortar joint. However, in the reinforced clay masonry wall, vertical and diagonal cracks eventually spread throughout the entire wall.

The aerated masonry walls failed due to mortar joint separation because of the low strength of the mortar brick connection in the aerated masonry wall. Fracture was not observed on the front face of the clay brick masonry walls but was found in the aerated masonry walls. The reinforced walls of both kinds were observed to have successfully contained the debris of the blast. Fully reinforced clay masonry walls had 4.5 to 11 times the blast resistance of the unreinforced clay masonry walls. Fully reinforced aerated masonry walls had 15 times the blast resistance of the unreinforced aerated masonry walls. Clay masonry walls, reinforced or unreinforced, performed much better overall at resisting the blasts than their aerated counterparts.

3.3. Polyurethane. Knox et al. [21] performed tests on both standalone polyurethane and polyurea/polyurethane mixes. All of the polymers in the study were noted to increase ductility and decrease wall fragmentation. In later studies, pure polyurea was used because of strength, flammability, and cost [4, 21]. The most recent study to experiment with pure polyurethane was that of Johnson et al. [20], where polyurethane film was applied to an unreinforced masonry wall with a tape and epoxy system. The polyurethane increased the ultimate flexural strength of the wall, but its ability to reduce fragmentation was not gathered because it was not used in the dynamic tests.

3.4. Steel Plates. Recent investigations of steel plates and unreinforced masonry are rare due to the noted challenges of cost and increased dead load [9].

3.5. Aluminum Foam. Experimental blast loading to aluminum foam and unreinforced masonry is an area of potential research.

3.6. Engineered Cementitious Composites. Maalej et al. [22] created 18 clay brick walls that have a 1000×1000 mm face

and are 100 mm thick. The solid clay bricks used to build the wall were $215 \times 100 \times 70$ mm. The walls were divided into three series of 6 walls. In series 1 and 2, there were two control unreinforced walls while series 3 had just 1 unreinforced wall. Each series contained one reinforced wall with the following configurations: (a) a single-faced 34 mm thick engineering cementitious composite (ECC) layer, (b) a double-faced 34 mm thick ECC layer, (c) a single-faced 34 mm thick ECC layer with 8 mm diameter steel mesh, and (d) a double-faced 34 mm thick ECC layer with 8 mm diameter steel mesh. The ECC used in this study was a hybrid-fiber mix containing 1.5% of high performance polyethylene and 0.5% of steel fibers. The first and second series of walls were subjected to a quasi-static load test while the third was subjected to low-velocity impact load testing. The quasi-static load tests differ in that the first series load was applied on a 100×100 mm patch of the wall while the second series had a 780×780 mm distributed load applied. The quasi-static tests showed that the ECC retrofitting techniques, in general, were able to increase the ultimate capacity of the walls. Series 1 walls showed an increase in the failure loads by 6.5 and an increase in deflection capacity by 17.3 in comparison to the base wall. Series 2 walls showed an increase in the failure loads by 6.5 and an increase in deflection capacity by 17.3 in comparison to the base wall. Under the impact loads, the damage level was assessed based on the average crater diameter, indentation depth, crack propagation, and fragmentation. Walls with steel mesh showed a decrease in crater size and indentation depth in comparison to walls without it. Likewise, double-sided walls also showed increased penetration resistance like their steel mesh counterparts. Maalej et al. concluded that this was because the ECC at the impact face was able to absorb a large amount of impact energy. The ECC strengthened masonry walls were concluded to be able to increase the masonry wall's resistance to impact loads.

4. Numerical Simulations

4.1. Fiber Reinforced Polymers. Ghaderi et al. [24] simulated, in ABAQUS, FRP strips 1.5 mm thick in a vertical, horizontal,

and blended formation on the interior face of masonry walls, a blast loading model. The blast was measured by a scaled distance parameter, Z :

$$Z = \frac{R}{W^{1/3}}, \quad (1)$$

where R is the distance at which the blast is applied and W is the weight of the TNT. The scaled distance was unique to this study. The walls were subject to a scaled distance parameter of $2.2 \text{ m/kg}^{1/3}$, $1.8 \text{ m/kg}^{1/3}$, and $1.5 \text{ m/kg}^{1/3}$. As the distance to the wall decreased, more cracks occurred and more fiber became detached from the wall. Fragmentation was not addressed explicitly by Ghaderi et al.; however, it can be inferred from the modeling that fragmentation would be minimized in the actual field.

Alsayed et al. [16] created a finite element model in ANSYS-AUTODYN to represent their 2.1 m long by 1.5 m high masonry wall surrounded by a reinforced concrete frame. The model contained four distinct Lagrangian parts: the RC frame, RC footing, infill masonry wall, and the GFRP sheets. The RC frame, RC footing, and infill masonry wall were all modeled as 8-node hexahedral elements while the GFRP sheets were 4-node shell elements. Air around the wall was modeled as an Euler ideal gas. Explosives were modeled using the Jones-Wilkins-Lee equation of state. Blast modeling was done with a two-step process involving a 1D radial analysis of the explosion followed by a 3D analysis used to judge the effect of the blast on masonry wall. 1D analysis was done until a reflecting surface is reached. The 1D analysis is then remapped within the 3D model. Alsayed et al. [16] set the model to terminate after 10 ms since it was considered enough time to investigate the effects of the blast. For each of the five tests, the charge size and standoff distance were 1.134 kg, 4.8 m, 49.9 kg, 4.8 m, 14.2 kg, 2.0 m, 113.4 kg, 4.0 m, and 500 kg, 4.0 m, respectively. The FE model used was validated by comparing finite element analysis to ConWep values and to the experimental results of the studies. Alsayed et al. [16] found that the arrival time of the blast, peak incident, and peak reflected overpressures matched between the three and went on to conclude that the numerical solution was a valid way to analyze the FRP-strengthened walls and the unstrengthened walls.

LS-DYNA was employed by Chen et al. [18] to perform structural analysis on MU15 P type porous brick walls. CFRP, steel mesh, and steel bars were evaluated numerically to judge them as possible retrofitting and repairing techniques for masonry walls. The masonry and mortar were modeled as 8-node solid elements. To model the steel mesh retrofit technique, a two-node Hughes-Liu beam element with 2×2 Gauss quadrature integration was used. The steel bars and CFRP were represented as $22.5 \times 22.5 \text{ mm}$ 3D shell elements. In regard to the material model parameter, Chen et al. [18] used Mat.72Rel3 that consisted of three failure surfaces: the initial yield surface, the maximum yield surface, and the residual yield surface. To model the steel and FRP, material models 24 and 54 were used, respectively. Modeling the epoxy adhesive is key to capturing an experimentally confirmed failure mode in LS-DYNA, which is the delamination of the FRP sheets from the masonry wall. Chen et al. [18] used the

Automatic Surface-to-Surface Tiebreak to model the contact of the masonry wall and FRP to the epoxy. Walls were also modeled to be on top of a concrete slab as in the experimental tests. The anchors holding the wall down were modeled using tied node sets with failure using the Contact Tiebreak Node to Surface option. Numerical results were found to be similar to the experimental results performed by Chen et al. [18]. Both the steel bars and the CFRP were almost completely delaminated from the wall, but CFRP performed better by having less fragmentation. The steel mesh retrofitted walls were able to prevent all serious damage. The main form of damage on the steel mesh walls was the spallation of plastered mortar.

Hamed and Rabinovitch [25] presented a theoretical numerical model to properly describe the behavior of FRP-strengthened masonry walls subjected to out-of-plane loads. Numerous equations and conditions are presented to describe some of the behavioral conditions of the masonry walls, including bonding conditions and equilibrium equations. Using the mathematical descriptions, a step-by-step process is presented to find a solution regarding the masonry wall's rigidity. First, an initial guess is made; in this case, the mortar joints of the masonry wall are assumed to be uncracked. Second, using the rigidities derived in the initial guess to allow for the solving of the governing equations, an analysis of the structure is performed. Once an analysis of the structure has been performed, an analysis of the mortar joints is performed as follows: the strain distribution is found with step two's solution, the depth of the active zone in the cracked joint, and then the rigidity of each joint. Lastly, the steps are repeated until the difference between the original rigidity and the calculated rigidity is reasonably small. The numerical model was then used to compare the distribution of internal forces and deflection between an unreinforced masonry wall and one modeled with FRP strips. FRP strips notably had concentrations of shear and tensile stress near joint edges. Hamed and Rabinovitch [25] noted that this coincided well with the debonding failure mechanisms in other papers' experimental studies. Likewise, Hamed and Rabinovitch [25] stated that stiffer FRP tended to increase out-of-plane deflection, internal shear, and axial forces on the masonry walls and FRP strips in their numerical study.

Hamed and Rabinovitch [19] adjusted their previous mathematical model (Hamed and Rabinovitch [25]) to properly describe the nonlinear behavior of materials subjected to failure level loads. Six critical failure mechanisms of the strengthened masonry walls were examined in the numerical analysis. They are as follows: crushing of the masonry units, shear failure of masonry units, rupture of the composite material, debonding of the strengthening system, sliding/shear at the mortar joints, and crushing of the mortar joints. The model followed the same set of steps as Hamed and Rabinovitch [25]: an initial guess regarding the rigidity of the structure, an analysis of the structure, an analysis of the rigidity of the joints, and then convergence where the initial rigidity closely matches the calculated rigidity of the joints. The analytical results of the model agreed fairly well with the experimental tests performed, showing that the control wall's load capacity was about 25% less than that of the CFRP

reinforced wall's load capacity. In this sense, the experimental model validated the analytical model to some degree and led Hamed and Rabinovitch [19] to use a nonlinear model to properly describe the behavior of mortar joint and its interfaces.

4.2. Polyurea. Ghaderi et al. [24], through simulation in ABAQUS, tested polyurea at a range of thicknesses from 5 to 15 mm when applied to both sides of the wall, at the scaled distance of $0.9 \text{ m/kg}^{1/3}$. Polyurea was then tested at a thickness of 15 mm when applied to one side of the wall as well. The impulse ratio for polyurea applied on the interior side of the wall was 859% and for polyurea applied on both sides was 1623%. The means for each wall's maximum impulse were 8.59 and 16.23 times higher, respectively, than an unreinforced wall. Polyurea was concluded to be an effective retrofit technique that has high performance capabilities and is effective at reducing fragmentation. Double-sided carbon FRP had the highest FRP impulse ratio at 465%. Therefore, polyurea performed considerably better than even the most effective FRP method in regard to impulse ratio.

Aghdamy et al. [11] also evaluated the effectiveness of XGnP- and POSS-reinforced polyurea on the same walls Irshidat et al. [10] used. A finite element model was created to compare the physical and computer test results, although it was in LS-DYNA. However, the XGnP-reinforced polyurea performed worse when compared to the unreinforced polyurea according to Aghdamy et al.'s [11] analysis and was concluded to have less blast resistance than both the POSS-reinforced polyurea and the unreinforced polyurea. Based on their impulse-pressure diagrams, Aghdamy et al. [11] were able to conclude that the POSS-reinforced polyurea was the most effective polyurea tested at resisting high pressures under short durations, but all polyurea types were effective in low pressure, long duration events.

Irshidat et al. [10] also created a finite element model with ANSYS-AUTODYN. The finite element model was considerably accurate in its ability to estimate the effects of the test loading with regard to debris velocity, midpoint deflection, and the walls' failure mechanisms. In combination, the tests showed that the POSS-reinforced polyurea had noteworthy improvement over the unreinforced polyurea, while the XGnP-reinforced polyurea showed little to no improvement of the unreinforced polyurea.

Along with the physical tests, Davidson et al. [8] used LS-DYNA3D to improve the understanding of the behavior of the blast loading. The finite element model mostly agreed with the deflection and accelerometer gauges attached to the masonry walls during loading. Together, the tests showed that a thin layer of polyurea applied to the inner face of the wall significantly reduced fragmentation. Polyurea effectively bonded to the masonry, which demonstrates that it is a viable retrofit material. Finally, it was concluded that elongation capacity is more important than high stiffness for a blast retrofitting material.

4.3. Aluminum Foam. Su et al. [23] conducted a finite element analysis on aluminum foam using LS-DYNA. A series of numerical analyses were done with scaled Z values

(see (1)) on unreinforced masonry walls. The aluminum foam was 40 mm thick in the analysis and had a density of 400 kg/m^3 . At $Z = 4 \text{ m/kg}^{1/3}$, the unreinforced masonry wall was blown out immediately by the air-blast load, while the wall reinforced with aluminum foam at $Z = 4 \text{ m/kg}^{1/3}$ appeared to only have light damage. The thickness of the aluminum foam was then tested at 12 mm and 24 mm for $Z = 3 \text{ m/kg}^{1/3}$. The results showed that the larger the thickness of the aluminum foam is, the better it was at mitigating the blast. Overall, the analysis showed aluminum foam to be a promising option for mitigating a blast.

Aghdamy et al. [11] also conducted finite element analyses on aluminum foam using LS-DYNA. Aghdamy et al. [11] modeled foam layers of varying thicknesses, 13 mm, 20 mm, and 25 mm, but constant density, 450 kg/m^3 . Increasing the foam's thickness was found to be effective at increasing its resistance to blast load. Aluminum foam was then modeled on both sides of an unreinforced masonry wall at 13 mm thickness on both sides of the wall. An impulse-pressure diagram was created from this model. From the diagram, aluminum foam was concluded to be an effective retrofitting technique. POSS polyurea was also analyzed in the same way. It was applied to both sides of a wall at a thickness of 4.5 mm. Aluminum foam, in comparison to the POSS polyurea, was more effective in the quasi-static regime while POSS polyurea was better at resisting loads in the dynamic and impulsive regime.

Su et al.'s [23] and Aghdamy et al.'s [11] finite element analyses show that aluminum foam has the potential to be a new material for resisting blast loading. This makes experimental tests of the material desirable.

5. Fragmentation Mitigation

There is no apparent method for determining the amount of fragmentation beyond subjective observation and comparison. Baylot et al. [14] hypothesized that debris velocity could be a viable measure of fragmentation but observations proved velocity to be a poor indicator. The Department of Defense Minimum Antiterrorism Standards for Buildings [3] has developed four levels of protection assessments which account for flying debris in the standard; however, these levels of protection typically were not used, or not reported on, in the various reviewed articles. Regardless, when flying debris is evident, the lowest level of performance is assigned. Thus, fragmentation is a binary response (it either did or did not occur), without regard to the amount or reduction based on treatments. In addition to fragmentation, blast loading and standoff distance varied by the level of performance and with each investigation. Thus, fragmentation mitigation efforts must rely on comparisons conducted within the respective investigations.

5.1. Fiber Reinforced Polymers. FRP is the most widely used material to investigate the performance on unreinforced masonry walls. It has shown good success in both numerical and experimental investigation at reducing the amount of fragmentation during blast events. FRP is an effective method at reducing the amount of fragmentation. In addition, FRP

can increase shear wall ductility and improve structural integrity through collapse prevention.

5.2. Polyurea. Davidson et al. [8] selected pure polyurea spray-on material out of 21 different polymers based on strength, cost, stiffness, ductility, and resistance to fire. From this and from subsequent investigators, polyurea exhibited the most promise to mitigate fragmentation with comparative advantages over other retrofitting materials.

5.3. Polyurethane. Polyurethane was noted to have the ability to reduce fragmentation as well as polyurea and FRP. Knox et al. [21] performed tests on both standalone polyurethane and polyurea/polyurethane mixes, both of which performed well and successfully decreased wall fragmentation. However, polyurethane's ability to reduce fragmentation has not recently been evaluated. Likewise, the type of polyurethane used has the potential to alter its effectiveness.

5.4. Steel Plates. Steel plates have the unique advantage compared to other retrofitting techniques of being a well-known, highly controlled, and predictable material. In addition, construction industry laborers have existing knowledge of steel for installation purposes. Steel is ductile and dense providing excellent protection against fragmentation and spalling of masonry due to blast loading. However, due to the dead load increases, it is best suited for single story buildings in retrofit applications.

5.5. Aluminum Foam. Aluminum foam has yet to be experimentally tested but it shows a high potential to resist blast loading, limits fragmentation, and has a limited increase to the dead load of a structure.

5.6. Engineered Cementitious Composites. ECC were subjected to low-velocity (nonblast) type loadings. ECC are anticipated to have good performance against fragmentation but have yet to be experimentally tested. These composites show promise with the desirable qualities of increased strength, durability, and energy dispersion for retrofitting unreinforced masonry. Regardless, these materials can provide secondary masonry elements such as return walls and interior walls with the ability to contain damage due to blast loads.

5.7. Recommendation. For future investigations analysis relating to the level of protection found in the Department of Defense Minimum Antiterrorism Standards for Buildings [3] or similar standard would provide more comparative data universally.

6. Conclusions

Retrofitting techniques for blast protection of unreinforced masonry walls such as FRP, polyurea, polyurethane, steel sheets, and aluminum foam have been presented in this paper. These techniques have been investigated over the last 15 years to enhance the strength and ductility of unreinforced masonry walls and decrease fragmentation. However, it is

difficult to compare test results and methods since there is no publically set standard for the magnitude of blasts or the distance at which the blast is applied. General findings of the different retrofitting materials include the following:

- (1) FRP and polyurea are the two most widely studied retrofitting techniques because of their effectiveness, lightweight, practicality of application, and cost.
- (2) Fragmentation is a key indicator of the effectiveness [13] of the mitigation techniques employed as binary response flying debris or no flying debris.
- (3) Elongation capacity is more important than high stiffness for a blast retrofitting material [8].
- (4) Results from experimental tests show that glass FRP and woven roving have similar effectiveness [6].
- (5) Direct FEA comparison of FRP retrofitting techniques to polyurea retrofitting techniques showed that interior polyhedral oligomeric silsesquioxane polyurea retrofit had higher impulse ratio of 859% when compared to double-sided carbon FRP's 464% [24].
- (6) Aluminum foam was more effective in the quasi-static test than polyhedral oligomeric silsesquioxane polyurea, while the polyhedral oligomeric silsesquioxane polyurea was more effective in the dynamic and impulsive tests [11].
- (7) Boundary conditions affect the performance of masonry walls subjected to lateral loads. Simulating realistic boundary conditions allows for more accurate interpretation of a retrofitting technique's performance [17].

Competing Interests

The authors declare that they have no competing interests.

References

- [1] M. Nagdy and M. Roser, "Terrorism," 2016, <http://ourworldindata.org/terrorism/>.
- [2] American Society of Civil Engineers (ASCE), "Blast protection of buildings," ASCE/SEI 59-11, 2011.
- [3] DoD, "DoD minimum antiterrorism standards for buildings," Tech. Rep. UFC 4-010-01, US Department of Defense (DoD), 2013.
- [4] P. A. Buchan and J. F. Chen, "Blast resistance of FRP composites and polymer strengthened concrete and masonry structures—a state-of-the-art review," *Composites Part B: Engineering*, vol. 38, no. 5-6, pp. 509–522, 2007.
- [5] L. J. Malvar, J. E. Crawford, and K. B. Morrill, "Use of composites to resist blast," *Journal of Composites for Construction*, vol. 11, no. 6, pp. 601–610, 2007.
- [6] K. H. Tan and M. K. H. Patoary, "Blast resistance of FRP-strengthened masonry walls. I: approximate analysis and field explosion tests," *Journal of Composites for Construction*, vol. 13, no. 5, pp. 422–430, 2009.
- [7] M. Stanley, J. Metzger, and R. Martinez, "UL-like testing of commercial off-the-shelf products that enhance the blast and

- ballistic resistance of structures, quick look report 2,” Tech. Rep. TR-04-48, 2005.
- [8] J. S. Davidson, J. R. Porter, R. J. Dinan, M. I. Hammons, and J. D. Connell, “Explosive testing of polymer retrofit masonry walls,” *Journal of Performance of Constructed Facilities*, vol. 18, no. 2, pp. 100–106, 2004.
 - [9] J. S. Davidson, J. W. Fisher, M. I. Hammons, J. R. Porter, and R. J. Dinan, “Failure mechanisms of polymer-reinforced concrete masonry walls subjected to blast,” *Journal of Structural Engineering*, vol. 131, no. 8, pp. 1194–1205, 2005.
 - [10] M. Irshidat, A. Al-Ostaz, A. H.-D. Cheng, and C. Mullen, “Nanoparticle reinforced polymer for blast protection of unreinforced masonry wall: laboratory blast load simulation and design models,” *Journal of Structural Engineering*, vol. 137, no. 10, pp. 1193–1204, 2011.
 - [11] S. Aghdamy, C. Wu, and M. Griffith, “Simulation of retrofitted unreinforced concrete masonry unit walls under blast loading,” *International Journal of Protective Structures*, vol. 4, no. 1, pp. 21–44, 2013.
 - [12] J. Wang, H. Ren, X. Wu, and C. Cai, “Blast response of polymer-retrofitted masonry unit walls,” *Composites Part B: Engineering*, 2016.
 - [13] G. S. Urgessa and A. K. Maji, “Dynamic response of retrofitted masonry walls for blast loading,” *Journal of Engineering Mechanics*, vol. 136, no. 7, pp. 858–864, 2010.
 - [14] J. T. Baylot, B. Bullock, T. R. Slawson, and S. C. Woodson, “Blast response of lightly attached concrete masonry unit walls,” *Journal of Structural Engineering*, vol. 131, no. 8, pp. 1186–1193, 2005.
 - [15] T. Stratford, G. Pascale, O. Manfroni, and B. Bonfiglioli, “Shear strengthening masonry panels with sheet glass-fiber reinforced polymer,” *Journal of Composites for Construction*, vol. 8, no. 5, pp. 434–443, 2004.
 - [16] S. H. Alsayed, H. M. Elsanadedy, Z. M. Al-Zaheri, Y. A. Al-Salloum, and H. Abbas, “Blast response of GFRP-strengthened infill masonry walls,” *Construction and Building Materials*, vol. 115, pp. 438–451, 2016.
 - [17] T. T. Bui and A. Limam, “Out-of-plane behaviour of hollow concrete block masonry walls unstrengthened and strengthened with CFRP composite,” *Composites Part B: Engineering*, vol. 67, pp. 527–542, 2014.
 - [18] L. Chen, Q. Fang, J. Fan, Y. Zhang, H. Hao, and J. Liu, “Responses of masonry infill walls retrofitted with CFRP, steel wire mesh and laminated bars to blast loadings,” *Advances in Structural Engineering*, vol. 17, no. 6, pp. 817–836, 2014.
 - [19] E. Hamed and O. Rabinovitch, “Failure characteristics of FRP-strengthened masonry walls under out-of-plane loads,” *Engineering Structures*, vol. 32, no. 8, pp. 2134–2145, 2010.
 - [20] C. F. Johnson, T. R. Slawson, T. K. Cummins, and J. L. Davis, “Concrete masonry unit walls retrofitted with elastomeric systems for blast loads,” in *Proceedings of the 24th Army Science Conference*, Orlando, Fla, USA, 2004.
 - [21] K. J. Knox, M. I. Hammons, T. T. Lewis, and J. R. Porter, *Polymer Materials for Structural Retrofit*, Force Protection Branch, Air Expeditionary Force Technology Division, Air Force Research Laboratory, Tyndall Air Force Base, Fla, USA, 2000.
 - [22] M. Maalej, V. W. J. Lin, M. P. Nguyen, and S. T. Quek, “Engineered cementitious composites for effective strengthening of unreinforced masonry walls,” *Engineering Structures*, vol. 32, no. 8, pp. 2432–2439, 2010.
 - [23] Y. Su, C. Wu, and M. Griffith, “Mitigation of blast effects on aluminum foam protected masonry walls,” *Transactions of Tianjin University*, vol. 14, no. 1, pp. 558–562, 2008.
 - [24] M. Ghaderi, V. A. Maleki, and K. Andalibi, “Retrofitting of unreinforced masonry walls under blast loading by FRP and spray on polyurea,” *Cumhuriyet Science Journal*, vol. 36, no. 4, pp. 462–477, 2015.
 - [25] E. Hamed and O. Rabinovitch, “Out-of-plane behavior of unreinforced masonry walls strengthened with FRP strips,” *Composites Science and Technology*, vol. 67, no. 3-4, pp. 489–500, 2007.

Research Article

Experimental Study of the Effectiveness of Sacrificial Cladding Using Polymeric Foams as Crushable Core with a Simply Supported Steel Beam

H. Ousji,^{1,2} B. Belkassem,¹ M. A. Louar,^{1,2} B. Reymen,¹ L. Pyl,² and J. Vantomme¹

¹Civil and Materials Engineering Department, Royal Military Academy (RMA), Av. de la Renaissance 30, 1000 Brussels, Belgium

²Department of Mechanics of Materials and Constructions, Vrije Universiteit Brussel (VUB), Pleinlaan 2, 1050 Brussels, Belgium

Correspondence should be addressed to H. Ousji; hamza.ousji@rma.ac.be

Received 21 April 2016; Accepted 4 August 2016

Academic Editor: Li Chen

Copyright © 2016 H. Ousji et al. This is an open access article distributed under the Creative Commons Attribution License, which permits unrestricted use, distribution, and reproduction in any medium, provided the original work is properly cited.

The present paper focuses on the study of the effectiveness of the sacrificial cladding using polymeric foam as crushable core to reduce the delivered blast energy using a simplified structure. The latter consists of a simply supported steel beam under a localized blast load. The tested sacrificial cladding has a cross-sectional area of $80 \times 80 \text{ mm}^2$. The effect of the front plate mass and the crushable core properties (plateau stress and thickness) is studied. Three polymeric foams are investigated: (a) the expanded polystyrene foam (PS13) with a density of 13 kg/m^3 , (b) the closed-cell polyurethane (PU30) with a density of 30 kg/m^3 , and (c) the open-cell polyurethane (PU50) with a density of 50 kg/m^3 . Four front plate masses are used: 144, 188, 336, and 495 g. All possible combinations are tested to determine their absorption capacity. The obtained results show that the absorption capability increases by increasing the front plate mass, the plateau stress, and the thickness of the crushable core. The open-cell polyurethane PU50 performs better. Disintegration problems are observed on the expanded polystyrene PS13 after the end of the compression process.

1. Introduction

Significant effects are observed after accidental and intentional explosions. This makes protective techniques necessary to ensure survivability. Considerable research has been conducted on the study of protective structures aiming at reducing the transmitted pressure to the main structure. Sacrificial cladding structures receive a lot of attention [1–10]. They consist of a crushable core between the main structure and a front plate. The core material is often a cellular solid allowing large plastic deformation under relatively low constant stress (plateau stress, which is the average stress of the plastic region of the stress-strain curve of the crushable core) [1–8, 11–13]. In order to control the magnitude of the transmitted pressure to the main structure and to guarantee an optimal design of the sacrificial cladding, the study of the effectiveness and the determination of the absorption capacity of a given sacrificial cladding configuration is needed.

Both crushable materials and structures are used as sacrificial cladding core. Aluminium foams and honeycomb

structures receive a lot of attention [1–9, 11, 12]; the absorption mechanism, the dynamic behaviour, the effect of the front plate (mass and rigidity), and the crushable core properties are analysed. However, these cores are characterized by a relatively high plateau stress (between 1 and 10 MPa [14]) to protect a given structure. Wu and Zhou [9] study the use of foam cladding to protect a simply supported reinforced concrete (RC) slab against blast loading. They use an adapted SDOF model supported by a full scale experiment to study the effectiveness of aluminium foam on RC slab. They observe that the aluminium foam is not completely compacted and cracks are significant in depth and along the length of the slab. They explained the obtained results by the higher plateau stress transmitted to the main structure [3]. Xia et al. [8] perform a series of full scale experiments to study the effectiveness of graded density aluminium foam on RC slab under blast loading. The idea of the density-graded foam consists in the use of foam structure with various densities along its thickness in order to increase the overall energy absorbing capacity of aluminium foam while keeping

the transmitted stress at a reasonable low magnitude. Several density combinations test to protect a simply supported RC slab. They observe that an ascending density from bottom to top can improve the blast resistance compared to a foam with a uniform density. Yet, cracks and damage appear even with protection layers. Hence, a crushable core with lower plateau stress such as polymeric foam is required. However, research on the effectiveness of polymeric foams as crushable core is rather limited.

In literature, the pendulum (mainly the four-cable pendulum) is mostly used to experimentally study the effectiveness of several sacrificial cladding configurations [1, 6, 11, 12]. The pendulum system is used to measure the impulse by recording the horizontal displacement of the pendulum mass. However, the absorption capacity cannot be quantified from the available experimental results. For example, using a pendulum setup, Hanssen et al. [1] investigate the absorption capability of aluminium foam in order to reduce the delivered blast energy. They observed that the foam is unable to reduce the global response of the pendulum and thus the absorption capacity of the foam material cannot be calculated. Ma and Ye [3] explain that the results are understandable because the main structure design (the pendulum system) is not appropriate for blast mitigation measurements. To reach an effective protection, the resistance of the main structure and the resistance of the sacrificial cladding, in particular the crushable core, should be comparable [3]. The resistance of the crushable core is governed by the plateau stress. But the resistance of the pendulum system of Hanssen is 500 times lower than the resistance of the aluminium foam [3]. Hence, a design of an appropriate experimental setup, adapted to the investigated crushable material, is needed to evaluate the effectiveness of the sacrificial cladding.

The aim of the present paper is to study the effectiveness of sacrificial cladding using polymeric foam as crushable core by means of an adequate experimental setup. The design of the experimental setup is derived from the Ma and Ye theory [3]. The main structure is simulated by a simply supported steel beam under a localized blast load. The influence of the front plate mass and the crushable core properties (thickness and plateau stress) on the effectiveness is investigated. The studied sacrificial cladding is composed of combinations of the following parts:

- (i) Three polymeric foams: (a) the expanded polystyrene foam with a density of 13 kg/m^3 , (b) the closed-cell polyurethane with a density of 30 kg/m^3 , and (c) the open-cell polyurethane with a density of 50 kg/m^3 , labeled as PS13, PU30, and PU50, respectively.
- (ii) Four metallic front plates with different masses (144, 188, 336, and 495 g) labeled as FP1, FP2, FP3, and FP4, respectively.

The present paper is divided into four parts. First, a description of the material properties of both the main structure and the investigated crushable cores is presented. Second, a brief explanation of the Ma and Ye theory, used to select the adequate experimental setup, is presented. Third, a detailed description of the experimental setup and the

TABLE 1: Mechanical properties of S355JR steel.

$\rho \text{ (kg/m}^3\text{)}$	$E \text{ (GPa)}$	$R_{e0.2} \text{ (MPa)}$	$R_m \text{ (MPa)}$
7830	240	353.85	491.78

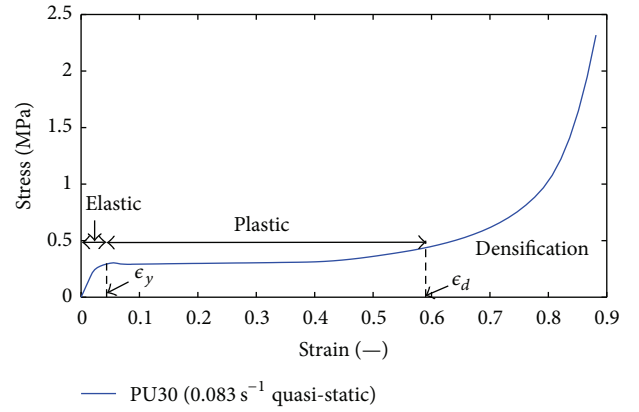


FIGURE 1: Stress-strain response of the closed-cell polyurethane PU30 under quasi-static compression load.

obtained results are presented. The effectiveness of the sacrificial cladding is illustrated. Finally, conclusions and perspectives are given.

2. Test Materials

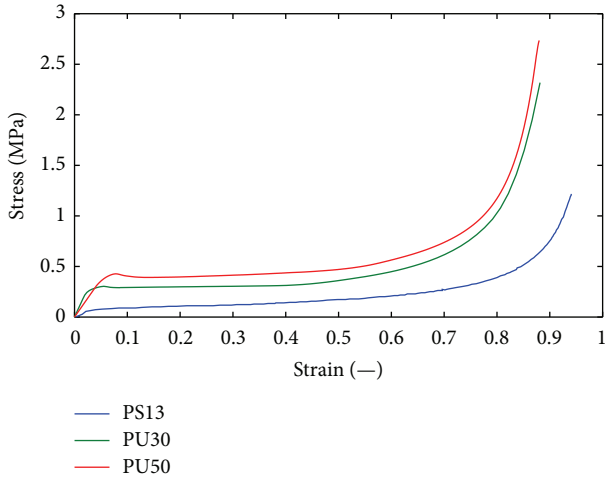
Two material kinds are used: polymeric foams and steel. The polymeric foam is used as crushable core of the sacrificial cladding. The steel is used for the simply supported beam. These materials are selected on the basis of the Ma and Ye [3] theory (see Section 3).

2.1. Steel. S355JR steel is used for the main structure, which consists of a simply supported steel beam. The beam specimens ($700 \times 80 \times 5 \text{ mm}^3$) are cut from 6 m long flat steel bars with a span of 600 mm. Based on tensile test results, the mechanical properties are summarized in Table 1, where ρ stands for the steel density, E is Young's modulus, $R_{e0.2}$ is the yield stress, and R_m is the tensile strength.

2.2. Polymeric Foam. Three polymeric foams are used as crushable core: the expanded polystyrene foam with a density of 13 kg/m^3 , the closed-cell polyurethane with a density of 30 kg/m^3 , and the open-cell polyurethane with a density of 50 kg/m^3 (labeled as PS13, PU30, and PU50, resp.). These materials are used in compression to absorb the generated blast energy. The uniaxial compressive stress-strain response for quasi-static as well as dynamic loading is divided into three distinct regions: elastic, plastic, and densification region (Figure 1). Two main parameters should be taken into account: the plateau stress σ_c which characterizes the relatively constant stress in the plastic region and the densification strain ϵ_d which marks the beginning of the densification behaviour. According to the development of Li et al. [16], the densification strain ϵ_d is the point where the energy

TABLE 2: Mechanical properties of the considered polymeric foams.

Properties		PS13 [15]	PU30	PU50
Density	(kg/m ³)	13	30	50
Young's modulus	(MPa)	2.7	11.36	7.45
Plateau stress	(MPa)	0.153	0.323	0.444
Densification strain	(—)	0.7	0.59	0.63

FIGURE 2: Stress-strain response of PS13 (0.001 s⁻¹) [15], PU30, and PU50 (0.083 s⁻¹) under quasi-static compression.

absorption efficiency, given in (1), reaches a maximum on the efficiency-strain curve. The plateau stress is calculated by means of (2) where ϵ_y stands for the strain corresponding to the start of the plastic behaviour.

$$\eta(\epsilon) = \frac{1}{\sigma(\epsilon)} \int_{\epsilon_y}^{\epsilon} \sigma(\epsilon) d\epsilon, \quad (1)$$

$$\sigma_c = \frac{\int_{\epsilon_y}^{\epsilon_d} \sigma(\epsilon) d\epsilon}{\epsilon_d - \epsilon_y}. \quad (2)$$

The quasi-static responses of the tested foams are depicted in Figure 2. The mechanical properties are summarized in Table 2. The compression test of the expanded polystyrene foam is taken from Chen et al. [15].

3. Sacrificial Cladding and Main Structure Selection

According to the analytical Load-Cladding-Structure (LCS) model developed by Ma and Ye [3], the choice of the sacrificial cladding configuration should be adapted to the main structure properties. The main structure is simplified to a single degree of freedom system (SDOF); see Figure 3, where k stands for the main structure stiffness, m_{se} stands for the equivalent mass of the beam, A stands for the cross-sectional area of the front plate, and $P(t)$ stands for the reflected pressure time history. The transmitted pressure to the main structure before the complete densification of the crushable core is governed by the plateau stress σ_c . The crushable core

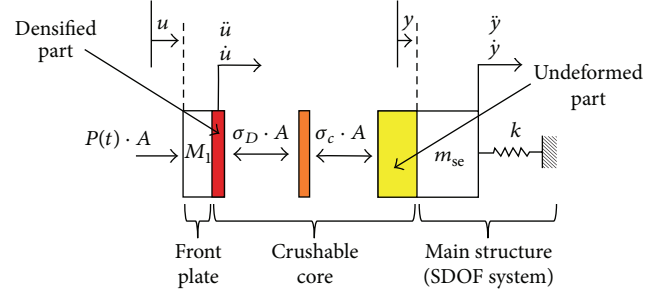


FIGURE 3: Simplified interaction between the sacrificial cladding and the main structure given by Ma and Ye [3].

resistance, the product of the cross-sectional area of the front plate A , and plateau stress σ_c should be comparable with the maximum resistance of the main structure (ky_c). When the plateau stress is very low, $\sigma_c A \ll ky_c$, the foam deforms even at lower load than the structure resistance ($\sigma_c A < P_0 A < ky_c$). When the plateau stress is very high, $\sigma_c A \gg ky_c$, the transmitted pressure to the main structure is higher than the allowable load (structure resistance) leading to a higher deflection of the structure ($> y_c$).

According to the same theory, the front plate should be stopped before reaching the densification region of the crushable core and the critical deflection of the structure. A minimum thickness of the crushable material is needed which depends on the front plate mass M_1 , the plateau stress σ_c , the total impulse I , and the maximum reflected pressure P_0 .

As a conclusion, an optimal combination of the front plate mass, the crushable core properties (plateau stress and thickness), and the main structure is essential to ensure the desirable absorption capacity. In the present work, we have the following:

- (i) The main structure is simulated by a simply supported steel beam under a localized load. The steel beam has a width of 80 mm, a thickness of 5 mm, and a span of 600 mm. It is characterized by a maximum resistance R_{max} of 1.3 kN obtained by applying the SDOF theory (see Section 4.2).
- (ii) The studied sacrificial cladding is composed of combinations of the following parts:
 - (a) Three polymeric foams: (a) the expanded polystyrene foam with a density of 13 kg/m³, (b) the closed-cell polyurethane with a density of 30 kg/m³, and (c) the open-cell polyurethane with a density of 50 kg/m³; the corresponding plateau stresses being compared with R_{max} : $A\sigma_c(\text{PS13}) = 0.98 \text{ kN} < R_{max} < A\sigma_c(\text{PU30}) = 2.07 \text{ kN} < A\sigma_c(\text{PU50}) = 2.84 \text{ kN}$.
 - (b) A steel front plate with four different masses (144, 188, 336, and 495 g).

4. Experimental Study

The goal of the experimental part is to study the effectiveness of sacrificial cladding using a polymeric foam as crushable

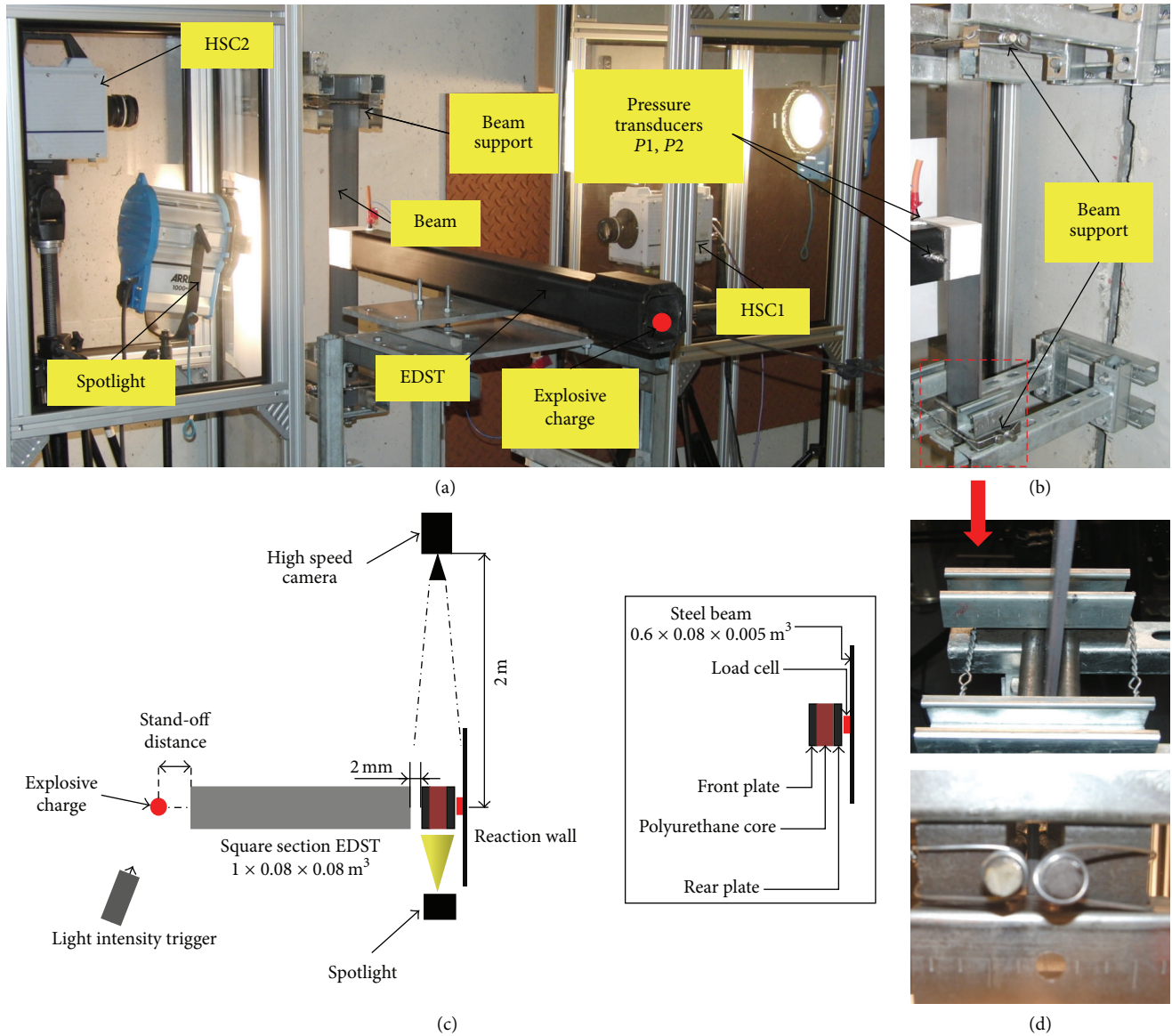


FIGURE 4: (a) Experimental setup, (b) beam support, (c) schematic representation of the experimental setup, and (d) simple support of the steel beam.

core with a simply supported steel beam. To fulfill this aim, three parts are developed:

- (i) First, a description of the experimental setup is presented.
- (ii) Second, the beam response without sacrificial cladding is discussed.
- (iii) Third, the effectiveness of the sacrificial cladding is analysed by studying the effect of both the crushable core properties (plateau stress and thickness) and the front plate mass.

4.1. Experimental Setup. A series of experimental tests are performed using the experimental setup shown in Figure 4. A schematic representation is given in Figure 4(c). A square

section explosive driven shock tube (EDST) is used to generate a planar blast wave at its end [17]. The used EDST is a steel square section tube with an inner edge of 70 mm, a thickness of 5 mm, and a length of 1 m. At the entrance, the tube is reinforced over the first 150 mm. The blast wave at the tube end is governed by the explosive mass (W) and the stand-off distance (the distance between the explosive charge and the EDST entrance). In order to avoid the impact between the beam and the tube during the beam oscillation, the blast load is chosen such as to ensure sufficient plastic deformation. This load is obtained by detonating 10 g of C4 set at 5 mm from the tube entrance. The maximum reflected overpressure and impulse at 2 mm from the tube end are 13.85 MPa and 2250 Pa·s with a standard deviation of 7.75% and 4.31%, respectively. The planarity is checked and reported in [18]. The reflected pressure profile is given in Figure 5. In

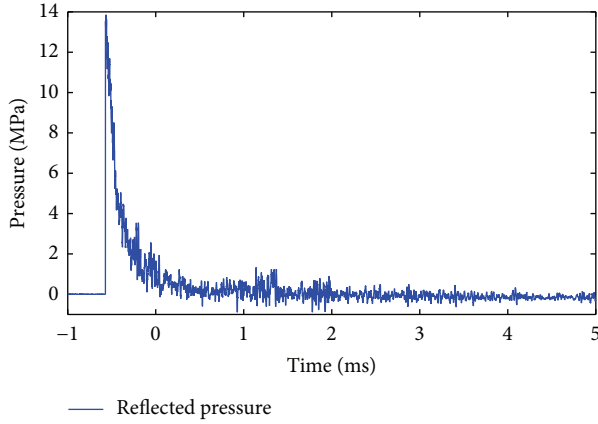


FIGURE 5: Reflected pressure measured at 2 mm after the EDST end generated by detonating 10 g of C4 set at a stand-off distance of 5 mm from the entrance of the EDST.

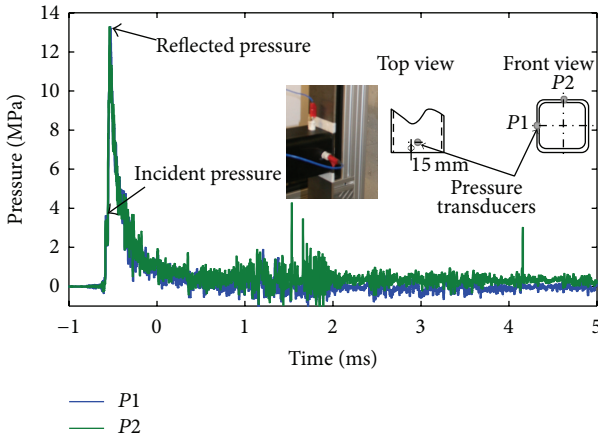


FIGURE 6: Pressure time signal measured at the tube end by pressure transducers P1 and P2 using 10 g of C4 set at a stand-off distance of 5 mm from the entrance of the EDST.

the present work, the pressure-impulse combination is kept identical for all experiments.

At the tube end (Figure 4(b)), two pressure transducers (P1 and P2) are mounted to measure the pressure at two different faces of the tube end. These measurements are used to check the repeatability of the applied over the different experiments. Figure 6 presents typical P1 and P2 measurements where two peaks can be identified: the first one is the incident pressure and the second one is the reflected pressure measured at the locations of P1 and P2.

At 2 mm after the end of the EDST end, sacrificial cladding configuration is fixed to the middle of the steel beam. The sacrificial cladding has a dimension of $80 \times 80 \text{ mm}^2$ (see Figure 4(c)) and is composed of a front plate and a crushable core. These three components (front plate, crushable material, and steel beam) are bonded together by means of double-sided bonding tape. The steel beam is simply supported and has a span of 0.6 m, a width of 80 mm, and a thickness of 5 mm. The steel beam supports are ensured by two steel cylinders for both extremities as shown in

Figure 4(d). Two high speed cameras (HSC1 and HSC2), Photron Fastcam SA5, are used to record the sacrificial cladding crushing and the beam deflection and to check the boundary conditions. Measurements are triggered by a light intensity trigger.

4.2. Beam Response without Sacrificial Cladding. The deflection of the simply supported beam under a localized blast load is discussed. Figure 7(a) illustrates the tracking of a point at midspan using a Labview code. The resulting deflections (three tests are performed for reproducibility) are plotted in Figure 7(c). A maximum deflection of 104 mm and a permanent plastic deflection of 57.57 mm with a relative standard deviation of 4.51% are recorded. The free vibration period T_0 is 32 ms. The time ratio between the positive phase duration ($t_d = 0.324 \text{ ms}$) and the free vibration period of the structure t_d/T_0 is about 10^{-2} which corresponds to an impulsive loading.

For simplicity purposes and in order to limit the needed amount of parameters (Figure 8), the idealized elastic-plastic model is adopted for the resistance function of the beam. Regarding the values of the elastic deflection y_e and the stiffness k , the stiffness is computed and given in Table 3, and the elastic deflection y_e is obtained from the deflection-time history results. Up to the first maximum deflection, two slopes are observed due to the change of the beam resistance from the elastic to the plastic behaviour (Figure 7(c)). The time at which this change occurs is identified from the derivation of the deflection-time history. Hence, the corresponding elastic deflection y_e of 39 mm is found. The maximum structure resistance R_{\max} (ky_e) equals 1.4 kN. The dissipated energy can be obtained from the surface under the response function curve.

The experimental results are compared with the single degree of freedom theory [19]. The case study is simplified to a simply supported beam under a punctual load (Figure 7(b)). The formula and the corresponding values are listed in Table 3. The experimental results are in concordance with the analytical prediction with a maximum relative difference of about 12% (k).

4.3. Beam Response with Sacrificial Cladding. 14 configurations are investigated; see Table 4. Every configuration is repeated three times to check the repeatability of the measurements. A maximum relative standard deviation of the beam deflection of 7.10% is recorded. Several sacrificial cladding configurations are tested to analyse the effect of both the crushable material (plateau stress and thickness) and the front plate mass. The experimental results are summarized in Table 4: the maximum deflection y_{\max} , the permanent plastic deformation y_{plastic} , the free vibration period T_0 , the maximum strain in the crushable core ϵ_{\max} , the initial front plate velocity v_0 , and the absorption capacity Eff of the sacrificial cladding configuration. The absorption capacity Eff is calculated by comparing E_0 , the dissipated energy in the steel beam without sacrificial cladding, with E_{sc} the dissipated energy in the steel beam with sacrificial cladding.

$$\text{Eff} = \frac{E_0 - E_{\text{sc}}}{E_0} 100\% = \frac{y_{\max} - y_{\max}(\text{sc})}{y_{\max} - y_e/2} 100\%, \quad (3)$$

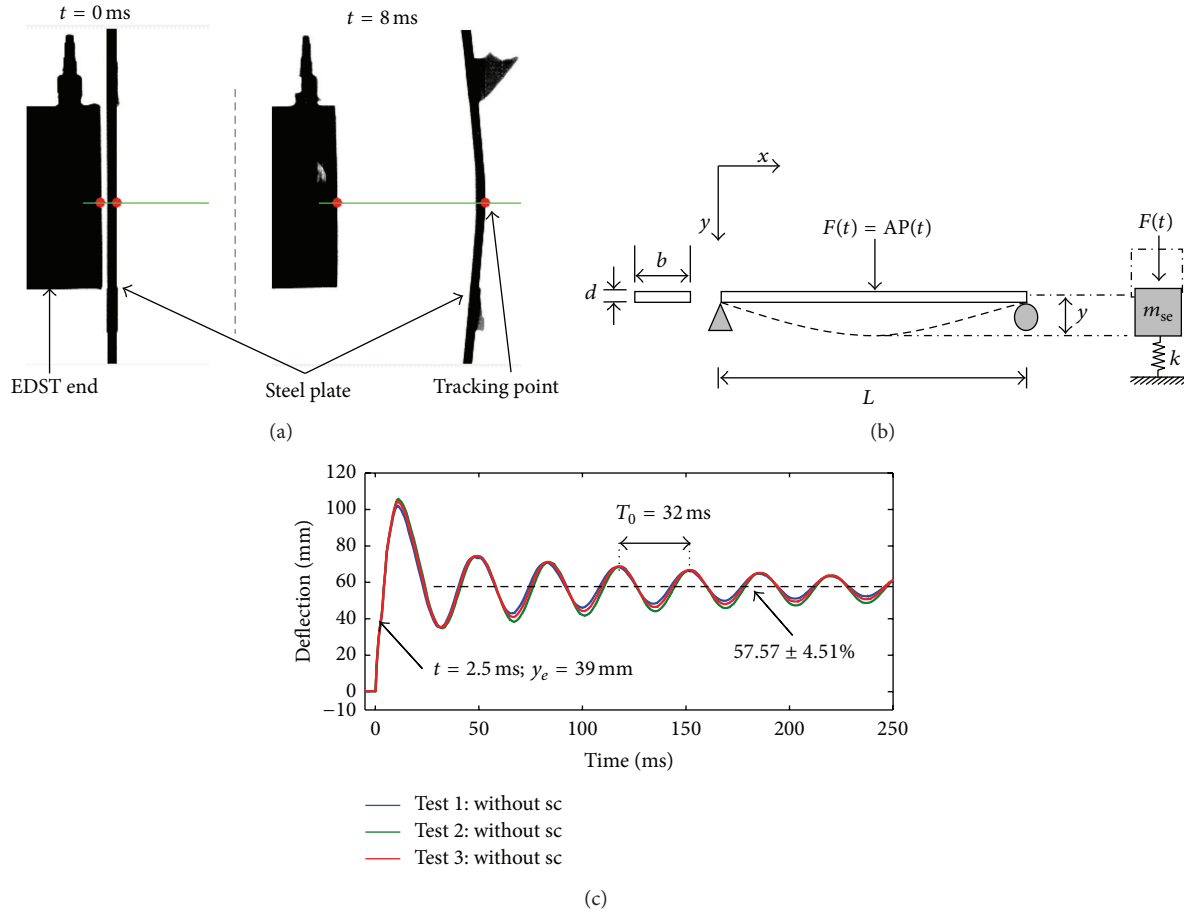


FIGURE 7: (a) Labview code used to track the middle point of the simply supported beam based on the video recorded by HSC1, (b) the equivalent SDOF system, and (c) the midspan response of a simply supported beam under a localized blast load for three tests.

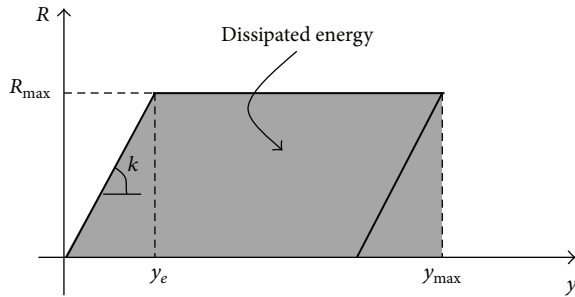


FIGURE 8: The idealized elastic-plastic response function [19].

where $y_{max}(sc)$ stands for the maximum deflection of the steel beam with sacrificial cladding. In order to facilitate the comparison, configurations are labeled as X1-X2-X3 where

- (i) X1 stands for the crushable core (PS13, PU30, PU50, ...),
- (ii) X2 stands for the crushable core thickness, l (mm),
- (iii) X3 stands for the front plate (FP1, FP2, FP3, ...).

The chronological crushing events of the PU30-050-FP1 and PU30-050-FP3 are presented in Figures 9 and 10. After

the detonation of the explosive charge, a blast wave propagates through the explosive driven shock tube. A planar blast wave at the tube end is generated ($t = t_1$). Hence, an impulsive load is applied on the front plate converting the blast energy to kinetic energy.

$$E_k = \frac{I^2}{2M_1}, \quad (4)$$

where I stands for the total impulse (N·s) and M_1 stands for the front plate mass. Assuming that the total blast energy is converted into kinetic energy, the compression of the crushable core starts with an initial front plate velocity $v_0 = I/M_1$. The foam starts to deform ($t = t_2$). The densified part moves with the same velocity as the front plate [1]. The undeformed part of the foam core moves with the steel beam under a load governed by the plateau stress σ_c [3] (Figure 3). Depending on the initial velocity v_0 , the crushable core thickness l , and the plateau stress σ_c , two cases can take place. The first case consists in the complete densification of the crushable core with a nonzero velocity of the front plate ($t = t_3$; PU30-050-FP1). In this case, the front plate and the fully compacted foam come together with the same velocity to impact the steel beam. The second case consists in

TABLE 3: Loading parameters and dynamic properties for an elastic-plastic, simply supported beam.

Parameter	Symbol/formula	Values (unit)	
Peak reflected pressure	P_r	13.85 (MPa)	
Positive phase duration	t_d	0.324 (ms)	
Beam span	L	0.6 (m)	
Beam mass	m	1.87 (kg)	
Beam thickness	d	5 (mm)	
Beam width	b	80 (mm)	
Moment of inertia	$I_t = bd^3/12$	833 (mm ⁴)	
Young's modulus	E	240 (GPa)	
Yield strength	$\mathfrak{R}_{0.2}$	353.85 (MPa)	
Load-mass factor	K_{LM}	0.49 (—)	
		Experimental value	Analytical value
Beam stiffness	$k = 48EI_t/L^3$	35.5	44.4 (kN/m)
Equivalent mass	$m_{se} = K_{LM}m$	0.92	0.92 (kg)
Natural period	$T_0 = 2\pi\sqrt{m_{se}/k}$	32	29 (ms)
Time ratio	t_d/T_0	$9.5 \cdot 10^{-3}$	10^{-2}
Maximum deflection	y_{max}	104	94 (mm)
Permanent plastic deflection	$y_{plastic}$	57.57	63 (mm)
Maximum resistance	R_{max}	1.4	1.3 (kN)

TABLE 4: Experimental results for the investigated sacrificial cladding configurations.

	l (mm)	FP mass (g)	y_{max} (mm)	$y_{plastic}$ (mm)	Std (%)	T_0 (ms)	ϵ_{max} (—)	v_0 (m/s)	Eff (%)
Without sc	—	—	104	57.57	4.51	32	—	—	—
PS13-050-FP3	50	336	105	57.31	4.10	34	0.95	34	—
PS13-050-FP4	50	495	92.53	42.34	3.60	32	0.95	21	13.57
PS13-100-FP3	100	336	84	35.16	5.80	32.5	0.90	30	23.67
PS13-100-FP4	100	495	77	24.75	1.30	32.5	0.85	22	31.95
PU30-050-FP1	50	144	98.03	54.47	3.70	33.8	0.95	68.5	7.06
PU30-050-FP2	50	188	98.13	51.59	5.70	33.7	0.90	37	6.95
PU30-050-FP3	50	336	88.10	38.84	2.30	32.5	0.75	32	18.82
PU30-050-FP4	50	495	67.33	23.69	4.30	33.7	0.51	23	43.40
PU30-100-FP1	100	144	74.96	33.10	4.65	32.6	0.72	68	34.37
PU30-100-FP3	100	336	65.02	12.82	5.51	34.6	0.65	29.5	46.13
PU30-100-FP4	100	495	59.72	12.50	7.10	32	0.30	21.5	52.40
PU30-150-FP1	150	144	70.12	22.49	2.40	32.55	0.48	69	40.09
PU50-050-FP1	50	144	78.25	34.06	6.10	32.5	0.92	68.5	30.47
PU50-050-FP3	50	336	62.27	21.94	3.40	32.5	0.70	31	49.38

the complete deceleration of the front plate (till zero velocity) before reaching the complete densification ($t = t_5$; PU30-050-FP3). In this case, the impulsive blast load is converted to a lower pressure (governed by σ_c) over a longer time duration.

After the end of the compression process, the front plate goes back together with the foam core (depending on the double-side bonding tape). Due to the transmitted pressure, the midspan point of the steel beam continues to move till a maximum deflection y_{max} which is followed by a free vibration behaviour around its permanent plastic deformation $y_{plastic}$. In some cases, the sacrificial cladding remains attached to the steel beam leading to a different free vibration

period T_0 (due to the added mass of the sacrificial cladding to the steel beam).

Several configurations are tested in order to study the effect of both the crushable core properties (plateau stress and thickness) and the front plate mass. The midspan deflection is compared to the configuration without sacrificial cladding. The absorption capacity, reported in Table 4, increases by increasing the front plate mass, the thickness, and the plateau stress of the crushable core. For practical reasons, a light front plate is preferable. Hence, to ensure the expected absorption capacity with a lighter front plate, the plateau stress and thickness should be increased. Due to the low density of

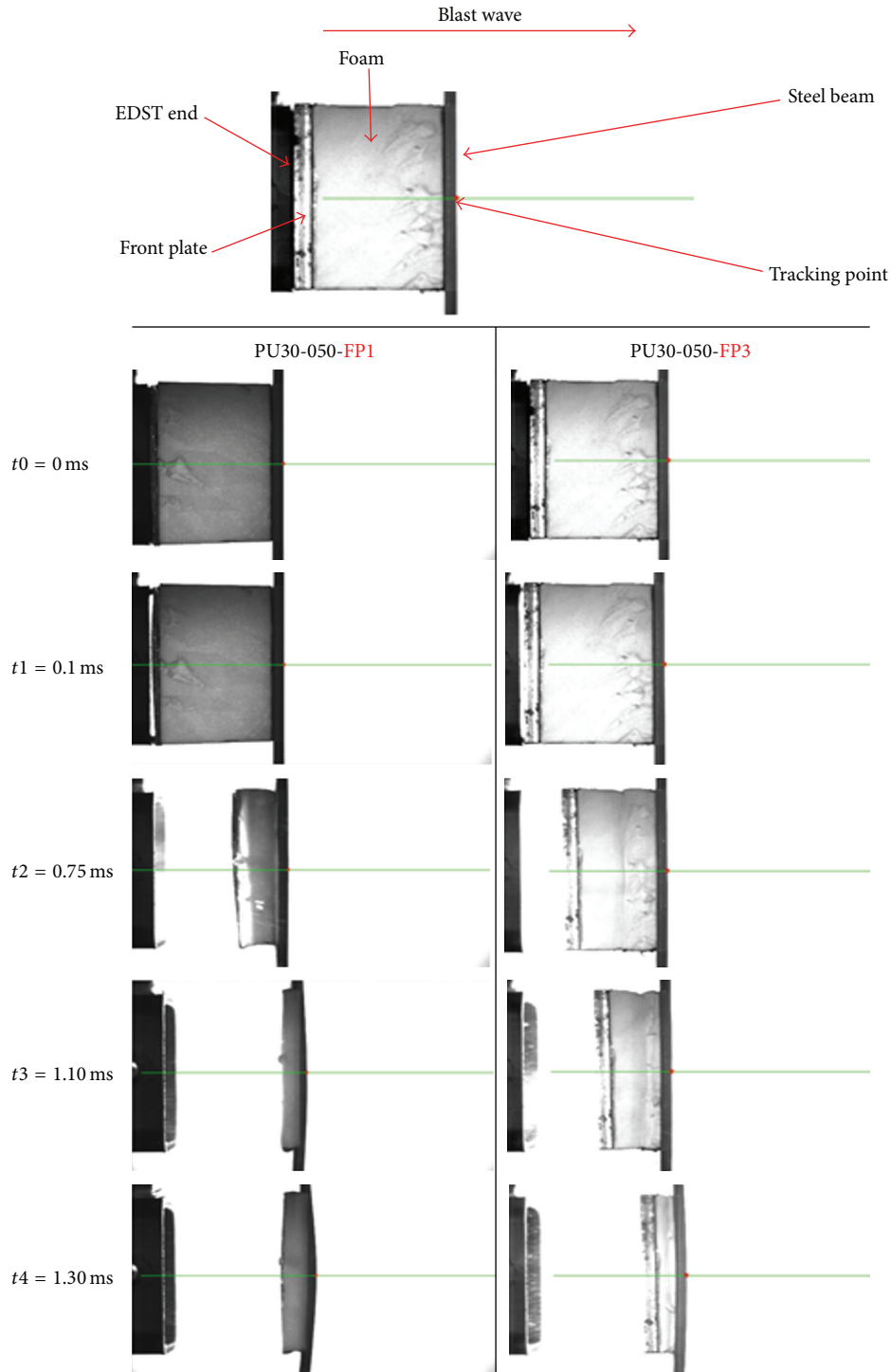


FIGURE 9: The chronological interaction of the simply supported beam with the tested sacrificial cladding configurations: PU30-050-FP1 and PU30-050-FP3.

the tested crushable material, the foam mass is negligible and the thickness can be increased till reaching the desired absorption capacity. However, the increase of the plateau stress is limited by the Ma and Ye criterion (Section 3) and depends on the maximum structure resistance.

4.3.1. Effect of the Crushable Core Thickness. The role of the crushable core is to convert the high reflected pressure generated by the blast wave to a relatively low constant pressure (governed by the plateau stress) over a longer time span. In other words, the role of the crushable material is to stop

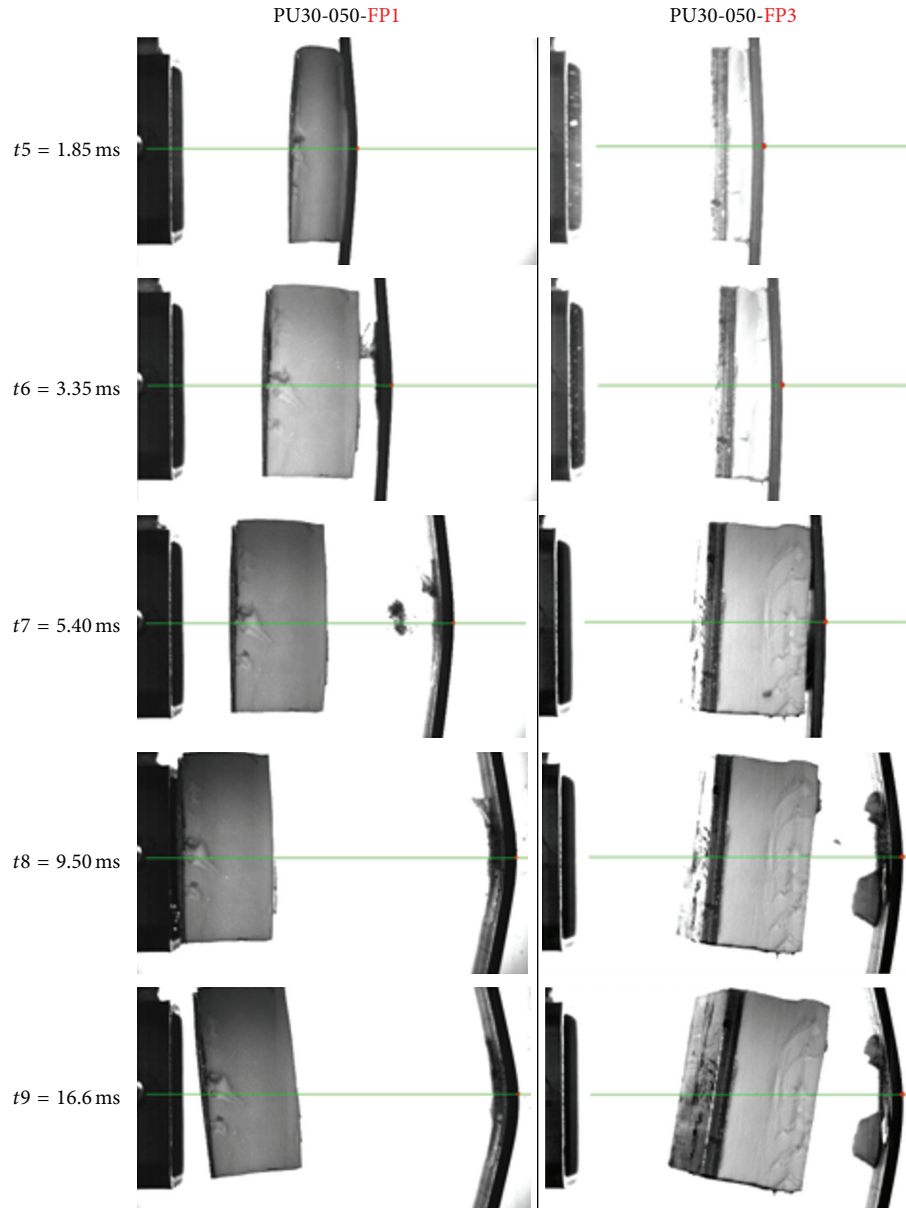


FIGURE 10: The chronological interaction of the simply supported beam with the tested sacrificial cladding configurations: PU30-050-FP1 and PU30-050-FP3.

the accelerated front plate before reaching the densification region (Figure 1). According to Hanssen theory [1], a minimum thickness which depends on the given blast load, the front plate mass, and the plateau stress of the crushable material is needed. Figure 11 illustrates the midspan deflection of the steel beam using sacrificial cladding with the same front plate (FP1) for several PU30 thickness. The dashed lines stand for the permanent plastic deformation of the steel beam.

The results are compared to the beam midspan deflection without sacrificial cladding. Using a thickness of 150 mm, the maximum compression strain is lower than the densification strain ϵ_d (Table 4). The front plate is stopped before the densification region of PU30. The maximum deflection and

the permanent plastic deformation are decreased by 32.5% and 61%, respectively, leading to an absorption capacity of 40%. With a PU30 thickness of 50 mm, the crushable core is fully compacted ($\epsilon_{\max} = 0.95$). Even a thickness of 100 mm is still insufficient to stop the front plate before the densification region ($\epsilon_{\max} = 0.72 > \epsilon_d$) and an absorption capacity of 34.37% is recorded.

Similar results are observed with the expanded polystyrene foam PS13 (see Table 4 and Figure 12). The absorption is not ensured by the PS13-050-FP3 configuration. The resulting midspan deflection is similar to the beam response without sacrificial cladding. After the full compaction, an ejection of the material is observed (Figure 13) which is

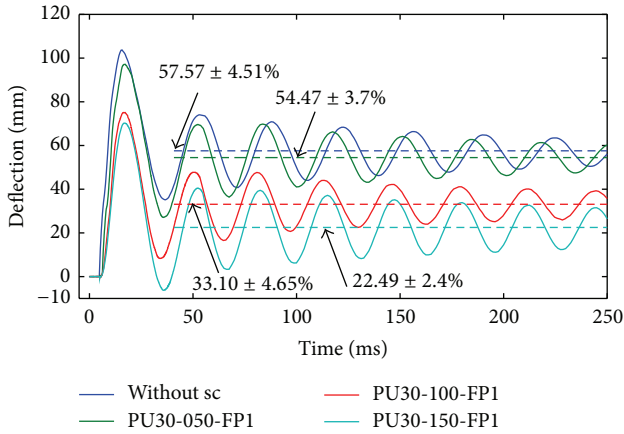


FIGURE 11: The midspan deflection of PU30-050-FP1, PU30-100-FP1, and PU30-150-FP1.

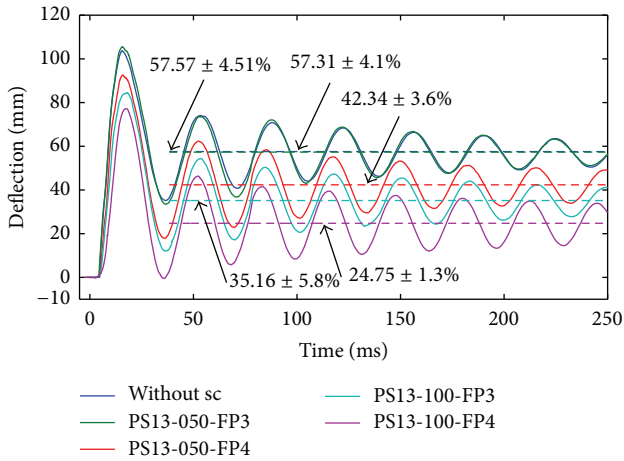


FIGURE 12: The midspan deflection of PS13-050-FP3, PS13-050-FP4, PS13-100-FP3, and PS13-100-FP4.

followed by the impact of the front plate on the structure. An enhancement of the absorption capacity is provided by increasing the thickness and the front plate mass.

4.3.2. Effect of the Crushable Core Plateau Stress. The absorption capacity of the crushable core increases by increasing the plateau stress. Figure 14 displays the midspan deflection for PS13, PU30, and PU50 using the same thickness and the same front plate. Using PU50, the front plate is stopped before reaching the densification strain leading to an absorption capacity of about 50%. For PU30, the densification region is reached without reaching the complete densification. However, as discussed in the previous section, the PS13 is fully compacted and a reduction of the permanent plastic deformation of the steel beam is not ensured.

4.3.3. The Effect of the Front Plate Mass. The role of the front plate is to distribute the loading in a uniform way over the cladding, enabling the crushable core to deform uniformly under compression [6]. The front plate should be rigid

enough to guarantee the uniform distribution. If the front plate is not rigid enough, a nonuniform compression of the crushable core can take place which may lead to an incomplete use of the energy absorption capability [6]. In the present work, the front plates are considered rigid. The mass is an important variable as it affects the total kinetic energy that the cladding system needs to absorb (see (4)). Hence, the bigger M_1 gets, the lower the kinetic energy to absorb will be. Figure 15 illustrates the effect of the front plate mass.

Similar results are observed for PU50 and PS13 and for several crushable core thickness. Figure 16 presents the effect of the front plate on the absorption capacity.

5. Conclusions and Perspectives

The purpose of the present paper is to study the effectiveness of sacrificial cladding using polymeric foam as crushable core by means of an adequate experimental setup. The influence of the front plate mass and the crushable core properties (thickness and plateau stress) on the effectiveness is investigated. Three different polymeric foams are tested: (a) the expanded polystyrene foam PS13, (b) the closed-cell polyurethane PU30, and (c) the open-cell polyurethane PU50. Four front plate masses are used: 144, 188, 336, and 495 g. All possible combinations are tested to determine their absorption capacity.

To fulfill the aim, an experimental setup is designed comprising an explosive driven shock tube, a high speed camera, and a simply supported steel beam. The use of an explosive driven shock tube helps to generate a controlled planar blast wave focused only on the studied sacrificial cladding system. The high speed camera is used to record the crushing of the cellular material and the beam deflection. The main structure is simulated by a simply supported steel beam under a localized blast load. The beam structure properties (material and dimensions) are selected according to the Ma and Ye theory [3].

The steel beam deflection (without sacrificial cladding) under a localized blast load is, first, studied and compared to the single degree of freedom theory. A good concordance is observed. The idealized elastic-plastic model is adopted as a response function of the steel beam and the dissipated energy is calculated. Second, the effectiveness of several sacrificial cladding configurations is studied. The steel beam deflections with sacrificial cladding are measured. Depending on the tested configuration, a reduction of the global response of the main structure is observed. The absorption capacity is calculated by comparing the energy dissipated by the steel beam without protection with the energy dissipated by the steel beam with sacrificial cladding. The absorption capacity increases by increasing the front plate mass, the crushable core thickness, and the plateau stress. But, for practical reasons, it is preferable to use a rigid and lighter front plate. Also, the increase of the plateau stress is limited by the structure resistance. Hence, a minimum thickness of the crushable core may ensure a specific absorption capacity.

Consequently, to achieve a positive protection, the properties of both the foam material and the front plate depend on

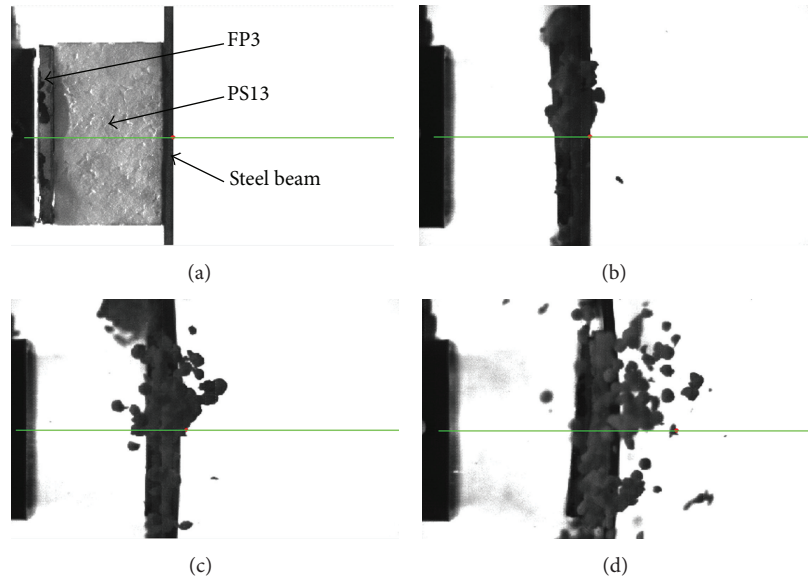


FIGURE 13: The PS13-050-FP3 configuration before and after the blast load: (a) before the blast load, (b) fully compacted expanded polystyrene, (c) material ejection and front plate impact with the structure, and (d) material ejection and front plate recoil.

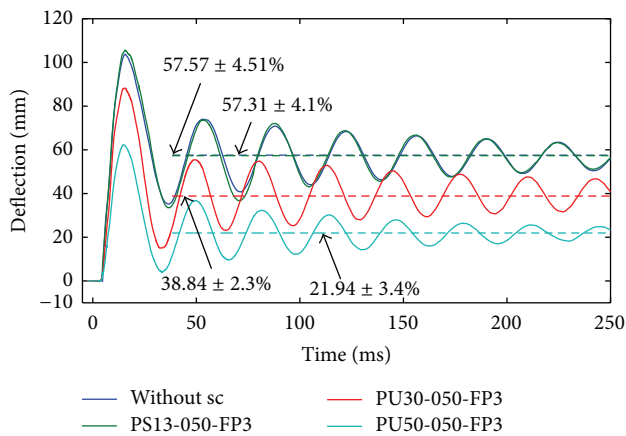


FIGURE 14: The experimental results of the midspan deflection of the steel beam with PS13-050-FP3, PU30-050-FP3, and PU50-050-FP3.

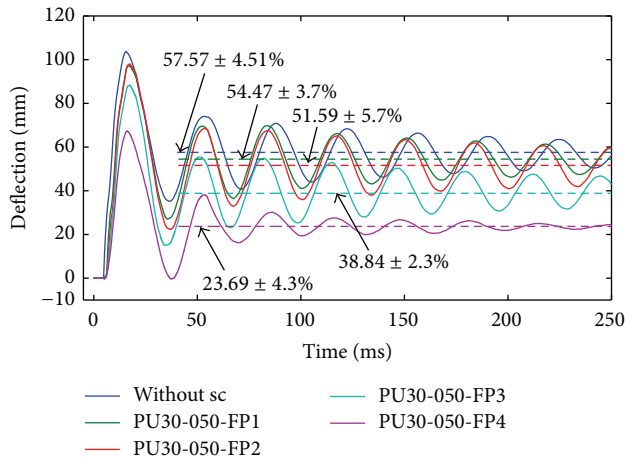


FIGURE 15: The effect of the front plate mass with a thickness of 50 mm of polyurethane PU30.

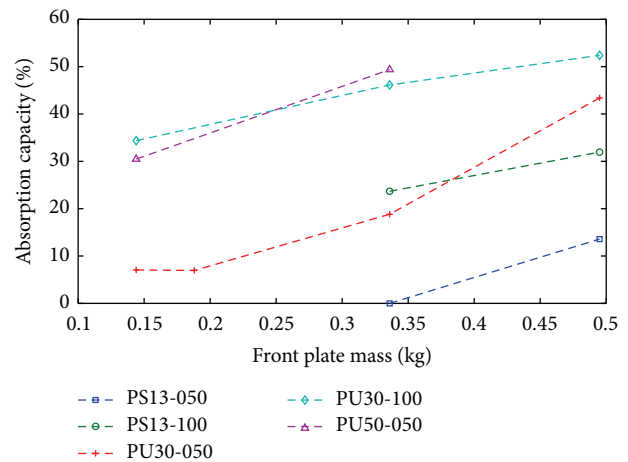


FIGURE 16: The effect of the front plate mass on the absorption capacity.

the main structure. First, the selected foam material should be characterized by a plateau stress comparable to the resistance of the main structure. Second, for practical reasons, the front plate material should be rigid and light. Third, depending on the selected foam material plateau stress, the pressure-impulse load, and the front plate mass, the minimum foam thickness can be selected using the Hanssen model [1].

In the present work, the open-cell polyurethane PU50 ensures the highest protection level due to its high plateau stress. The expanded polystyrene PS13 presents a lower plateau stress leading to an increased thickness to ensure the same absorption capacity as PU50. However, a disintegration problem is observed which limits its absorption capability. The closed-cell polyurethane PU30 presents considerable effectiveness.

The effectiveness of the sacrificial cladding is studied using a small specimen scale of $80 \times 80 \text{ m}^2$ with only one pressure-impulse combination. An extensive study in large scale and with other pressure-impulse is needed to confirm the obtained conclusions.

Nomenclature

ϵ_{\max} :	Maximum strain in the crushable core
η :	Energy absorption efficiency
ρ :	Steel density
A :	Cross-sectional area of the front plate
b :	Beam width
d :	Beam thickness
E :	Young's modulus
E_0 :	Dissipated energy with the steel beam without protection
E_k :	Kinetic energy of the front plate
E_{sc} :	Dissipated energy with the steel beam with protection
Eff:	Absorption capacity of the sacrificial cladding
I :	Total impulse (N·s)
I_t :	Second moment of area
k :	Stiffness of main structure
K_{LM} :	Load-mass factor
L :	Beam span
l :	Crushable core thickness
m :	Beam mass
M_1 :	Front plate mass
m_{se} :	Equivalent mass of the main structure
P_r :	Maximum reflected pressure
R_m :	Tensile strength
R_{\max} :	Maximum resistance of the main structure
$\text{Re}_{0.2\%}$:	Yield stress
T_0 :	Free vibration period of the main structure
t_d :	Positive phase duration of the reflected pressure
u :	Displacement of the front plate
v_0 :	Initial velocity of the front plate
W :	Explosive charge
y :	Deflection of the main structure
y_c :	Critical deflection of the main structure
y_e :	Elastic deflection of the main structure
y_{\max} :	Maximum deflection of the main structure
$y_{\max}(\text{sc})$:	Maximum deflection of the steel beam with sacrificial cladding
y_{plastic} :	Permanent plastic deflection of the main structure
EDST:	Explosive driven shock tube
FP1:	Front plate with a mass of 144 g
FP2:	Front plate with a mass of 188 g
FP3:	Front plate with a mass of 336 g
FP4:	Front plate with a mass of 495 g
HSC:	High speed camera
LCS:	Load-Cladding-Structure

$P(t)$:	Reflected pressure time history
P1:	Pressure transducer 1 set at the tube end
P2:	Pressure transducer 2 set at the tube end
PS13:	Expanded polystyrene with a density of 13 kg/m^3
PU30:	Closed-cell polyurethane with a density of 30 kg/m^3
PU50:	Open-cell polyurethane with a density of 50 kg/m^3
SDOF:	Single degree of freedom.

Competing Interests

The authors declare that they have no competing interests.

Acknowledgments

The authors are grateful to the Nestaan Holland company for providing the polyurethane specimen PU50.

References

- [1] A. G. Hanssen, L. Enstock, and M. Langseth, "Close-range blast loading of aluminium foam panels," *International Journal of Impact Engineering*, vol. 27, no. 6, pp. 593–618, 2002.
- [2] Q. M. Li and H. Meng, "Attenuation or enhancement—a one-dimensional analysis on shock transmission in the solid phase of a cellular material," *International Journal of Impact Engineering*, vol. 27, no. 10, pp. 1049–1065, 2002.
- [3] G. W. Ma and Z. Q. Ye, "Analysis of foam claddings for blast alleviation," *International Journal of Impact Engineering*, vol. 34, no. 1, pp. 60–70, 2007.
- [4] J. J. Harrigan, S. R. Reid, and A. S. Yaghoubi, "The correct analysis of shocks in a cellular material," *International Journal of Impact Engineering*, vol. 37, no. 8, pp. 918–927, 2010.
- [5] M. D. Theobald, G. S. Langdon, G. N. Nurick, S. Pillay, A. Heyns, and R. P. Merrett, "Large inelastic response of unbonded metallic foam and honeycomb core sandwich panels to blast loading," *Composite Structures*, vol. 92, no. 10, pp. 2465–2475, 2010.
- [6] G. S. Langdon, D. Karagiozova, M. D. Theobald, G. N. Nurick, G. Lu, and R. P. Merrett, "Fracture of aluminium foam core sacrificial cladding subjected to air-blast loading," *International Journal of Impact Engineering*, vol. 37, no. 6, pp. 638–651, 2010.
- [7] C. Qi, S. Yang, and R. Gao, "Numerical simulation of force enhancement by cellular material under blast load," *Advances in Mechanical Engineering*, vol. 2013, Article ID 328651, 10 pages, 2013.
- [8] Y. Xia, C. Wu, Z. Liu, and Y. Yuan, "Protective effect of graded density aluminium foam on rc slab under blast loading—an experimental study," *Construction and Building Materials*, vol. 111, pp. 209–222, 2016.
- [9] C. Wu and Y. Zhou, "Simplified analysis of foam cladding protected reinforced concrete slabs against blast loadings," *International Journal of Protective Structures*, vol. 2, no. 3, pp. 351–366, 2011.
- [10] H. Zhou, Z. Zhao, and G. Ma, "Protection against blast load with cellular materials and structures," *International Journal of Aerospace and Lightweight Structures*, vol. 2, no. 1, pp. 53–76, 2012.

- [11] X. Li, P. Zhang, Z. Wang, G. Wu, and L. Zhao, "Dynamic behavior of aluminum honeycomb sandwich panels under air blast: experiment and numerical analysis," *Composite Structures*, vol. 108, no. 1, pp. 1001–1008, 2014.
- [12] X. Li, Z. Wang, F. Zhu, G. Wu, and L. Zhao, "Response of aluminium corrugated sandwich panels under air blast loadings: experiment and numerical simulation," *International Journal of Impact Engineering*, vol. 65, pp. 79–88, 2014.
- [13] S. R. Reid and C. Peng, "Dynamic uniaxial crushing of wood," *International Journal of Impact Engineering*, vol. 19, no. 5-6, pp. 531–570, 1997.
- [14] L. Gibson and M. Ashby, *Cellular Solids: Structure and Properties*, Cambridge Solid State Science Series, Cambridge University Press, 2nd edition, 1999.
- [15] W. Chen, H. Hao, D. Hughes, Y. Shi, J. Cui, and Z.-X. Li, "Static and dynamic mechanical properties of expanded polystyrene," *Materials and Design*, vol. 69, pp. 170–180, 2015.
- [16] Q. M. Li, I. Magkiriadis, and J. J. Harrigan, "Compressive strain at the onset of densification of cellular solids," *Journal of Cellular Plastics*, vol. 42, no. 5, pp. 371–392, 2006.
- [17] H. Ousji, B. Belkassam, M. A. Louar et al., "Parametric study of an explosive-driven shock tube as blast loading tool," *Experimental Techniques*, vol. 40, no. 4, pp. 1307–1325, 2016.
- [18] H. Ousji, B. Belkassam, M. Louar, B. Reymen, L. Pyl, and J. Vantomme, "Numerical and experimental study of polyurethane foam used as core material in sacrificial cladding for blast mitigation," in *Proceedings of the 16th International Symposium for Interaction of the effects of Munition with Structures (ISIEMS '15)*, 2015.
- [19] P. Smith and J. Hetherington, *Blast and Ballistic Loading of Structures*, Butterworth-Heinemann, Boston, Mass, USA, 1994.

Research Article

Modelling Blast Effects on a Reinforced Concrete Bridge

Markellos Andreou,¹ Anastasios Kotsoglou,¹ and Stavroula Pantazopoulou²

¹*Department of Civil Engineering, Laboratory of Reinforced Concrete, Democritus University of Thrace, V. Sofias 12, 671 00 Xanthi, Greece*

²*Department of Civil Engineering, The Lassonde Faculty of Engineering, York University, 4700 Keele Street, Toronto, ON, Canada M3J 1P3*

Correspondence should be addressed to Stavroula Pantazopoulou; stavroula.pantazopoulou@gmail.com

Received 21 April 2016; Revised 27 June 2016; Accepted 28 June 2016

Academic Editor: Chiara Bedon

Copyright © 2016 Markellos Andreou et al. This is an open access article distributed under the Creative Commons Attribution License, which permits unrestricted use, distribution, and reproduction in any medium, provided the original work is properly cited.

The detailed investigation of blast phenomena and their catastrophic effects on existing structures are the main objectives of the present paper. It is well known that blast phenomena may be characterized by significant complexity, often involving complicated wave propagation effects as well as distinguishable material behaviors. Considering the above and in an attempt to provide a simplified modelling approach for the simulation of blast effects, a novel procedure is presented herein based on well-established methodologies and common engineering practices. In the above framework, firstly, the “predominant” deformation shape of the structure is estimated based on elastic finite element simulations under blast loads and then the structural response of the system is evaluated as a result of common computational beam-element tools such as displacement-based pushover analysis. The proposed methodology provides an immediate first estimation of the structural behavior under blast loads, based on familiar engineering procedures. A two-span reinforced concrete bridge was thoroughly investigated and the results provide insightful information regarding the damage patterns and localization.

1. Introduction

Although blasts are considered phenomena of significant severity and potential socioeconomic impact, only recently did the authorities realize the necessity for the formulation of an integrated design and assessment protective framework. Modeling the effects of these phenomena on structures is very demanding, requiring highly sophisticated simulations including advanced constitutive material models. These procedures are resource- and time-consuming. On the other hand, there is a lack of simplifying procedures that could be implemented by practicing engineers through the utilization of common computational tools. Herein, a simplifying procedure is proposed based on common analytical and computational tools that would provide a preliminary but yet reliable estimation of the blast impact to the structural integrity of bridges.

Blasts are short duration dynamic events that generate dynamic pressure waves which propagate radially from the source in space, exciting dynamic response in the structures

that are encountered in their path. The pressures acting on the affected surfaces are impulsive loads that impart significant amount of potential energy which sets damage-causing vibrations in the structure.

The various loads that act on a structure during its lifetime (natural or man-made) are characterized [1] by their range of frequency content and intensity (Figure 1(a)). Dynamic pressures exerted by blast explosions are considered among the most critical loads owing to their high intensity and frequency content, which falls within the range of values associated with fundamental eigenvalues of common buildings. Being a conveyor of potential energy, the blast wave evolves dilating in space (Figure 1(b)) as soon as it emerges. During this process it gets reflected on any surfaces it encounters when colliding with objects or structures or the ground (Figure 1(b)). In the case of surface explosions (where the source is at ground level), the reflection takes place almost simultaneously with the genesis of the wave. A schematic representation of the translation and dilation of the blast wave front caused by a surface explosion on a given structure are illustrated in

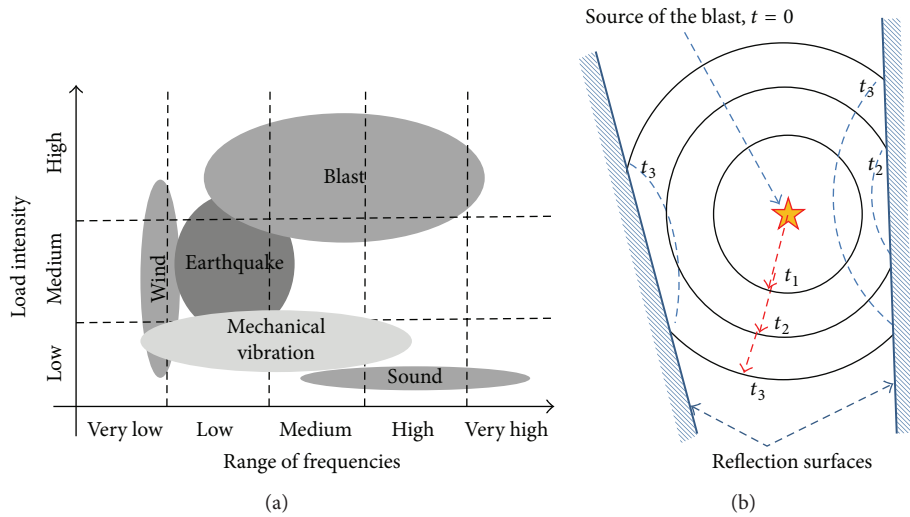


FIGURE 1: (a) Frequency range of different dynamic loads (according to [1]). (b) Collision and reflection of aerial blast waves (t_i are arrival times of the expanding wave front).

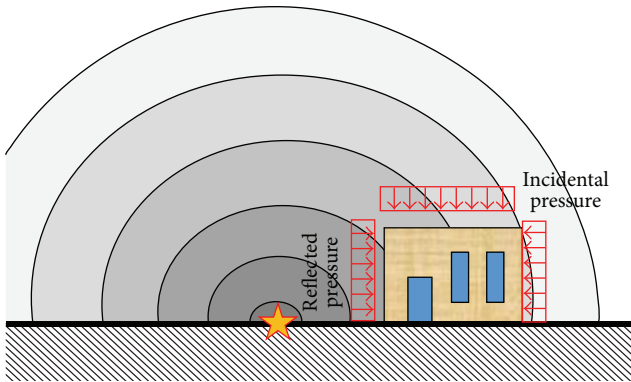


FIGURE 2: Schematic representation of the evolution of a surface blast wave in space; reflected and main pressure blast wave on an adjacent structure.

Figure 2. Note that reflected pressure waves affect surfaces perpendicular to the direction of the blast wave, whereas the incidental pressure wave affects the sides and back-face of the structure.

The effects of explosions are studied in this paper based on a simplifying procedure, with particular emphasis on one type of structure whose operation is vital in emergencies, namely, reinforced concrete highway overpasses. In the simplifying framework, the structure is approximated using concepts from generalized single-degree-of-freedom systems (Clough and Penzien [2]), where the dynamic response of the continuous structure is examined in a predominant shape of response. The proposed two-step methodology utilizes well-established structural engineering procedures as a preliminary design and assessment tool for the estimation of the impact of blast effects on structures. According to the above, the predominant deformation shape under blast loading is firstly evaluated based on ordinary elastic FE analyses and then a displacement-based pushover analysis is conducted to

a simplified beam-element lumped plasticity model in order to evaluate the nonlinear behavior of each structural component for the induced deformation pattern of the previous step. With the above proposed procedure, the complicated blast problem is reduced to a simplified two-step procedure, which may be further simplified if certain characteristic deformation patterns for design purposes would be instantly provided in the future, based on the structural configuration and the blast initiation point.

The first section of the study deals with the mathematical definition of the excitation function exerted by the explosion and its numerical representation in the framework of established structural analysis software, considering both the temporal and spatial definition of the evolving pressure profiles acting on the exposed structural surfaces. The investigation uses a selected bridge case study subjected to a passing blast wave for illustration of concepts. A linear 3D finite element model of the bridge structure was combined with a consistent time history simulation of the explosion pulse, placing particular emphasis on the sequence of contact of the pressure wave with the structure, which depends on the physical distance and the location of the source relative to the structure. An essential ingredient for assessment of deformation demands and damage potential caused by the event is the deformed shape assumed by the structure through the time history of the event; this is extracted from the calculated response results. Next, using this pattern of deformations, the structure was analyzed based on the implementation of a simplified ordinary beam-element structural model so as to enable the use of the results of a nonlinear pushover analysis of the bridge under transient pressure profiles that simulate the explosive loads. This simplification alleviated partly the complexity of the problem associated with the time dependency of the constitutive properties of the materials, whereas it was possible to identify the tendency for damage localization throughout the structure. In this way, it is possible to take advantage of the nonlinear modelling technology that is

stable and convergent when dealing with linear prismatic elements while avoiding convergence problems that would be owing to brittle failures in the continuous 3D finite element model.

2. Effects of Blast Waves on Structures and Material Response

2.1. Effects of Blast Waves on Structures. At any single point, the pressure wave has a time history of the type shown in Figure 3. The primary effect of a blast wave on a structure occurs during the positive phase, where pressure values are high; the negative phase has lesser consequences due to the attenuated pressure magnitudes and is usually neglected (Agrawal and Yi [1]).

An event is classified as blast if, compared with other catastrophic events such as wind and earthquake, the pressure momentum is several orders of magnitude greater than that of other phenomena (FEMA 426 [3]), whereas the pressure caused by the explosion attenuates quickly with increasing distance from the source affecting only a small part of the structure and causing great localized damage. Owing to the short duration of the blast, the mass participating in dynamic response is engaged usually at a later time, that is, until after the impulse has delivered its potential energy to its surroundings (positive phase). So, given that the loading has expired by the time the mass is mobilized in dynamic motion, it is extremely difficult to resonate the system while the load is acting. This definition underscores the difference between more conventional dynamic loads such as earthquake where partial resonance of eigenmodes is of primary significance. In the same context, due to the short duration of the loading exerted by the blast wave which typically ends within few milliseconds, it is possible to excite several additional modes (higher mode contribution) in the free vibration phase that follows, usually neglected in conventional seismic design. Of course this is a theoretical postulate; nonlinearity takes hold of the response as its intensity builds up, damping out quickly the participation of higher modes near failure.

The size and distribution of the applied pressures on the structure depend on the amount and type of released energy (which depend on the explosives used), the position of the source relative to the structure, and the magnitude and possible amplification of the resulting blast pressure owing to its interactions with objects encountered during dilation and propagation of the wave (Birhane [4]). The explosive wave exerts pressure on every exposed point of the structure encountered during its translation. The pressure depends on the arrival time t_a of the wave front at the point of the structure considered. This time includes the time of transfer of the released energy from the explosive material to the environment (Martin [5]). The pressure rises from an initial value p_o (the atmospheric or ambient pressure) to the peak normal pressure p_{so} (peak overpressure) instantaneously and it is subsequently reduced till its value attenuates to return to the initial pressure value. The durations of the positive and negative phases of the wave front are denoted by t_d and t_n (Figure 3): t_d is the time of pressure attenuation from the peak value to the initial value, whereas t_n is the subsequent time

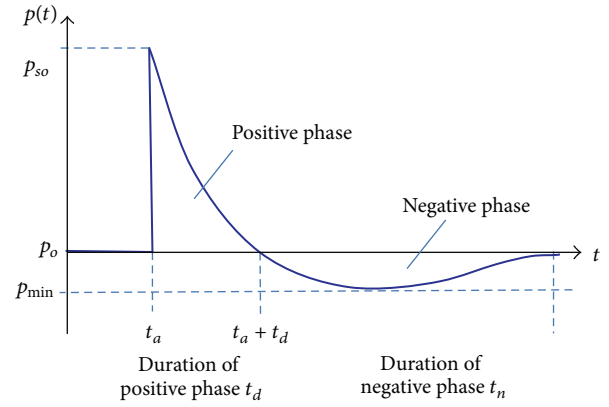


FIGURE 3: Diagram of pressure variation as a function of time.

interval up to the occurrence of the minimum negative value, p_{min} , in the negative phase. The pressure intensity versus time attenuation relationship is approximated by the following expression, known as the Friedlander equation (Baker [6]). The positive phase of the phenomenon concerns the main pressure wave of the blast wave (Figure 3):

$$p(t) = p_o + p_{so} \cdot \left(\frac{t - t_a}{t_d} \right) \cdot e^{-b((t - t_a)/t_d)}; \quad (1)$$

$$p_{so} = \frac{1}{Z} \cdot \left[\frac{1772}{Z^2} - \frac{114}{Z} + 108 \right] \text{ (kPa)},$$

where $Z = R/(W)^{1/3}$ is the scaled distance in $\text{m/kg}^{1/3}$ (obtained after pertinent normalizing; Ngo et al. [7]), W is the amount of the explosive material in [kg], and b is the coefficient of degradation which defines the slope of the attenuation curve (Martin [5]):

$$b = 5.2777 \cdot Z^{-1.1975}. \quad (2a)$$

Variable t_d (the positive phase duration) is defined by (Pandey et al. [8])

$$\begin{aligned} \frac{t_d}{W^{1/3}} &= \frac{980 \cdot [1 + (Z/0.54)^{10}]}{[1 + (Z/0.02)^3] \cdot [1 + (Z/0.74)^6] \cdot \sqrt{1 + (Z/6.9)^2}}. \end{aligned} \quad (2b)$$

For hemispherical explosions, that is, explosions that occur on ground surface, it is recommended that the variable term in (1) be multiplied by a factor equal to 1.8 to account for the reflection of the blast wave which occurs during the explosion (Lam et al. [9]):

$$p(t) = p_o + 1.8 \cdot p_{so} \cdot \left(\frac{t - t_a}{t_d} \right) \cdot e^{-b((t - t_a)/t_d)} \text{ (kPa)}. \quad (3)$$

2.2. Material Response under Strain Rate Loading. High strain rates affect the mechanical properties of the materials and thus the mechanisms of degradation of the various elements

of the structure. The effect of high deformation rate on material strengths is quantified by the Dynamic Increase Factor (DIF), which is defined as the ratio of the dynamic to static strength (Javier and Allen [10]). Blast loading causes excessively high rates of deformation in the order of $10^2/s$ – $10^7/s$, whereas for usual loads the rate of deformation ranges between $10^{-7}/s$ and $10^0/s$ (for reference, note that the rates associated with Creep and Relaxation phenomena are in the range of $10^{-8}/s$ to $10^{-5}/s$; pseudostatic loads occur at strain rates from $10^{-8}/s$ to $10^{-4}/s$; earthquake loads occur at strain rates from $10^{-5}/s$ to $10/s$. Explosions and collisions occur at strain rates from $10/s$ to $10^7/s$, whereas even higher rates correspond to astrophysical phenomena, CEB-FIP, Bulletin 56 [2]).

For reinforced concrete structures subjected to blast loading, the strength of concrete and reinforcing materials may experience a significant increase due to the rate effects. The increase may exceed 50% for the reinforcing steel, whereas it may exceed 100% for concrete in compression and more than 600% for concrete in tension (Javier and Allen [10]). An implication of this disproportional strength increase of the two materials is an alteration in practice of the intended hierarchy of failure modes: thus, a design controlled by flexural yielding under relatively low rates of loading may become controlled by shear or by a combined shear-flexural mode of failure at higher rates (Ngo et al. [7]). Design charts are available to estimate the DIF for the two materials based on the strain rate (CEB-FIP, Bulletin 55 [2]); however, the phenomenon may be also approximated by the following equations.

2.2.1. Rate Effects on Concrete Strength in Compression. Consider

$$\text{DIF} = \frac{f_{c,imp,k}}{f_{cm}} = \left(\frac{\dot{\epsilon}_c}{\dot{\epsilon}_{co}} \right)^{0.014}, \quad \text{for } \dot{\epsilon}_c \leq 30 \text{ s}^{-1} \quad (4a)$$

$$\text{DIF} = \frac{f_{c,imp,k}}{f_{cm}} = 0.012 * \left(\frac{\dot{\epsilon}_c}{\dot{\epsilon}_{co}} \right)^{1/3}, \quad (4b)$$

for $\dot{\epsilon}_c > 30 \text{ s}^{-1}$,

where $f_{c,imp,k}$ is the dynamic compression strength for loading rate $\dot{\epsilon}_c$, f_{cm} is the static compressive strength at loading rate $\dot{\epsilon}_{co}$, $\dot{\epsilon}_c$ is the rate of deformation taking values in the range from $30 \times 10^{-6} \text{ s}^{-1}$ to $3 \times 10^2 \text{ s}^{-1}$, and $\dot{\epsilon}_{co} = 30 \times 10^{-6} \text{ s}^{-1}$ is the rate of deformation under pseudostatic compression loading.

2.2.2. Rate Effects on Concrete Strength in Tension. Consider

$$\text{DIF} = \frac{f_{ct,imp,k}}{f_{ctm}} = \left(\frac{\dot{\epsilon}_{ct}}{\dot{\epsilon}_{cto}} \right)^{0.018}, \quad \text{for } \dot{\epsilon}_{ct} \leq 10 \text{ s}^{-1} \quad (5a)$$

$$\text{DIF} = \frac{f_{ct,imp,k}}{f_{ctm}} = 0.0062 * \left(\frac{\dot{\epsilon}_{ct}}{\dot{\epsilon}_{cto}} \right)^{1/3}, \quad (5b)$$

for $\dot{\epsilon}_{ct} > 10 \text{ s}^{-1}$.

Term $f_{ct,imp,k}$ in (5a) and (5b) is the dynamic tensile strength for loading rate $\dot{\epsilon}_{ct}$, f_{ctm} is the static tensile strength for

loading rate $\dot{\epsilon}_{cto}$, $\dot{\epsilon}_{ct}$ is the rate of tensile deformation in the range from $1 \times 10^{-6} \text{ s}^{-1}$ to $3 \times 10^2 \text{ s}^{-1}$, and $\dot{\epsilon}_{cto} = 1 \times 10^{-6} \text{ s}^{-1}$ (the rate of deformation at pseudostatic tensile loading conditions). Apart from material strength, the high deformation rate affects all other mechanical properties. For example, by definition, the modulus of elasticity of concrete under high deformation rate may be estimated from the following equation:

$$\frac{E_{c,imp}}{E_{ci}} = \left(\frac{\dot{\epsilon}_c}{\dot{\epsilon}_{co}} \right)^{0.026}, \quad (6)$$

where $\dot{\epsilon}_c$ is the rate of deformation under dynamic loading, $E_{c,imp}$ is the dynamic modulus of elasticity, and E_{ci} is the modulus of elasticity of concrete. Combining the above equations (and considering the familiar Hognestad's parabola for the stress strain response in uniaxial compression), the strain at peak stress considering the modulus and strength dynamic enhancement are estimated from

$$\frac{\epsilon_{c1,imp}}{\epsilon_{c1}} = \left(\frac{\dot{\epsilon}_c}{\dot{\epsilon}_{co}} \right)^{0.02}, \quad (7)$$

where $\epsilon_{c1,imp}$ is the deformation at peak stress for a load rate $\dot{\epsilon}_c$ and ϵ_{c1} is the deformation at peak stress under pseudostatic load.

2.2.3. Coefficient of Dynamic Amplification for Steel. Javier and John [11] studied the strength increase of reinforcement through experimental testing under high strain rates. Results followed a nonlinear relationship, where the rate of change of the dynamic amplification increased linearly with strain rate. It was concluded that the logarithm of DIF is at a linear relationship with the logarithm of the strain rate, $\dot{\epsilon}$. The relationship that was used, both for the yield stress and for the ultimate strength, is (Javier and John [11])

$$\text{DIF} = \left(\frac{\dot{\epsilon}}{10^{-4}} \right)^a. \quad (8)$$

Parameter a used for the calculation of the yield and ultimate reinforcement stress is obtained from the following relationships:

$$a = a_{f_y}, \quad \text{where } a_{f_y} = 0.074 - 0.04 \cdot \left(\frac{f_y}{414} \right) \quad (9a)$$

$$a = a_{f_u}, \quad \text{where } a_{f_u} = 0.019 - 0.009 \cdot \left(\frac{f_y}{414} \right). \quad (9b)$$

f_y is the yield stress of the reinforcement and f_u is the ultimate strength of the reinforcement in MPa.

This model applies to reinforcing steel with yield stress ranging between 290 and 710 MPa and for strain rates ranging between 10^{-4} and 225 s^{-1} . The strength increase estimated according to (9a) and (9b) is considered only for passive reinforcement (i.e., it is not valid for prestressing steel. Dynamic amplification is not considered when dealing with the strength of prestressing cables).

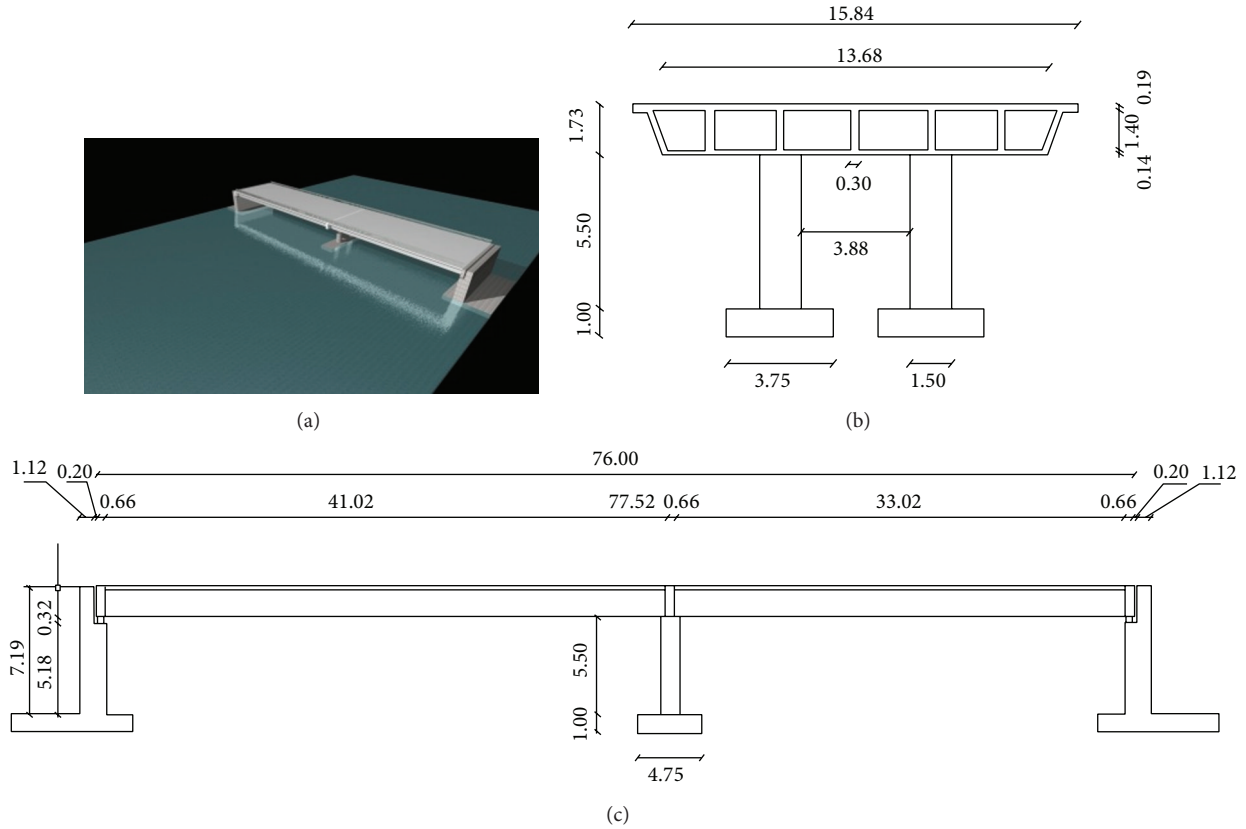


FIGURE 4: (a) Schematic representation of the bridge. (b) Geometric characteristics (transverse cross section). (c) Lengthwise cross section of the bridge.

3. Investigating the Effects of Blast Waves on a Highway Overpass

Blast effects on bridges are studied on a model bridge highway overpass, as illustrated in Figure 4(a). The bridge superstructure selected for study has the geometric properties of an actual bridge system (Kotsoglou and Pantazopoulou [12]) with monolithic connection at the central bent and the edge abutments (Figure 4(b)). The bridge has two unequal spans with a two-column central bent. The deck comprises a box section of multiple cells. Span lengths are 42.00 m and 34.00 m (Figure 4(c)). The box cross section is divided to cells through 5 beams of I cross section, having a web width of 0.3 m, whereas the superstructure height is 1.73 m.

The central bent columns have a circular cross section of 1.50 m diameter supported by separate pile caps resting on pile groups; each foundation block was a 3.75 m × 4.75 m × 1.00 m rectangular block. Clear height of the columns was 5.50 m. The portal frame bent was centered at the midpoint of the deck width with no eccentricity, whereas the clear transverse distance between columns was 3.88 m. Columns were monolithically connected with a bent cap beam (transverse beam) which in turn was connected monolithically with the adjacent deck superstructure. In the analysis of the bridge case study, the following parameter values were assumed: C30/37 concrete class (Eurocode 2, 2004) with a characteristic

compressive strength $f_{ck} = 30$ MPa and a nominal elastic modulus $E_c = 32$ GPa, whereas S500B steel was taken for all loose reinforcement (characteristic steel yield strength $f_{yk} = 500$ MPa). Self-weight and support reactions were estimated from the available architectural drawings of the bridge.

3.1. Variation of Simulated Blast Pressure on the Bridge. The problem considered in this study concerns the dynamic response of the bridge described above, owing to a surface explosion at near distance. A key issue to resolve first is the pressure profile occurring throughout the bridge structure and how the pressure wave propagates in space and time.

At the moment of the explosion the main pressure wave is transmitted uniformly in all directions. Over the duration of the transmission process the pressure varies with time: the peak pressure that occurs in each point in space depends on the distance from the source and the amount of the explosive material (Figure 5). It has therefore, for each explosion, the same value for all the points that are located at specific distance from source (spherical distance from the source as illustrated in Figure 2). In this representation p_{so1} , p_{so2} , p_{so3} , and p_{so4} are the peak values of the blast wave at distances R_1 , R_2 , R_3 , and R_4 from the source for the respective arrival times t_1 , t_2 , t_3 , and t_4 . Note that the values of the peak pressure are inversely proportional to the normalized distance, Z . For small values of normalized distance the pressures that

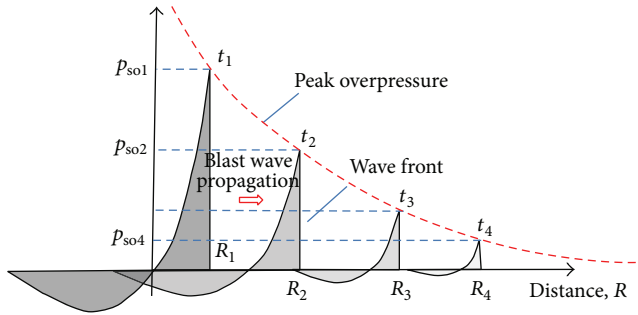


FIGURE 5: Attenuation of peak overpressure with distance from source: blast wave propagation.

develop are much higher relative to the peak pressures at points at a greater normalized distance.

Furthermore, the pressure of the blast wave does not attenuate at the same rate in all points in space since it depends on the coefficient of degradation b which is a function of Z . It is easy to demonstrate that the value of b increases, while the normalized distance decreases; that is, for small distances from the source and large amounts of explosive matter the coefficient is large, and the pressure decays quickly. This is the physical significance of b , whereas its calculation is related to the impulse (potential energy release) of the blast wave.

The effect of the pressure on the structure begins at the instant when the blast wave arrives at a specific point on its exposed surface, denoted henceforth as the “arrival time.” Pressure value is maximum for any given spatial point in consideration at the arrival time. The pressure magnitude attenuates from that peak value according to (1).

The duration of the time period over which the pressure values exceed the atmospheric pressure also depends on Z . The so-called positive phase begins at the time of arrival and ends at the instant where the pressure becomes equal to the atmospheric value for the first time. The instantaneous equilibrium that takes place heralds the beginning of the second phase of the phenomena, referred to as “negative phase.” The negative phase has a significantly longer duration as compared with the positive phase; however, its implications on the structure are significantly lower and often are neglected, while the values assumed by the negative pressure are comparatively much lower than those of the positive phase. The wind suction that follows the blast wave during its motion is related to the dynamic pressure, with the value always being equal to or greater than the atmospheric one (i.e., it does not assume negative values).

Regarding the bridge under consideration, the source of the explosion was assumed to be located on ground surface. Thermal radiation released upon the explosion and its effects on the material response were ignored in the present study. Surfaces that lie on the path of the wave front receive the reflected pressure, whereas the others receive the incidental pressure (Figure 2). To calculate the reflected pressure a coefficient equal to 1.8 was used on peak pressure in the Friedlander equation (see (6)). Material properties used in dynamic analysis of the FE model of the bridge were adjusted to

account for the effects of dynamic amplification; note that for blasts of moderate and high intensity (i.e., for strain rates higher than the reference value of $3 \times 10^2 \text{ s}^{-1}$) the DIF may be estimated from (4a)–(9b). For the case study considered herein the assumed explosive material was 500 Kgs TNT at a transverse distance of 3 m from the bridge’s central bent (Figure 6(a)).

4. Methodology in Modelling the Blast Wave

In the present section, a two-step simplifying methodology for the evaluation of blast effects on structures is proposed and implemented. The main scope is to provide an approximate yet reliable tool for instant estimations of the above effects based on well-established engineering design and assessment strategies. According to the methodology, a corresponding *predominant deformation shape* is initially estimated based on a simplified elastic analysis to be used as a displacement loading pattern in a detailed lumped plasticity beam-element computational model of the bridge [13]. The latter is considered to be a displacement-based pushover analysis in that instead of a fixed pattern of loads of gradually increasing intensity, the structure is subjected to a fixed pattern of displacements of gradually increasing intensity. The target displacement intensity level is that attained in the elastic analysis when accounting explicitly for the pressure front evolution. The above simplification is advantageous, not only because many engineers worldwide are familiar to the “pushover analysis” concept, but also because it reduces a multiparametric problem into a simplified structural engineering problem. Furthermore, when compared with detailed FE inelastic simulation models, a wide range of computational shortcomings may be eliminated, such as convergence due to ill-conditioning of material stiffness after brittle cracking, time and resource consuming problems, and so forth. Herein, the corresponding deformation shape of the system, under blast loads, was evaluated based on an elastic, time-dependent FE model of the case study bridge [14], but note that simplified, rational deformation shape approximations could be used instead.

Therefore, based on the deformation shape pattern obtained in the initial step, a displacement-based pushover analysis is conducted on a detailed beam-element computational simulation. Lumped plasticity or even brittle failure [13] properties (e.g., moment-curvature and shear failure criteria) were incorporated to each structural element in order to account for the induced damage.

4.1. Calculating the Load of the Blast Wave Front. Let time be defined with the reference starting point set at the instant of the explosion ($t_i = 0$); at that instant the wave begins to dilate in space evolving in all directions (Figures 1 and 6(a)). At time t_a the blast front reaches the nearest point of the structure (the point at shortest travel distance from the source; Figures 6(b) and 6(c)). In the bridge case study and for the blast event under consideration, this point is at the base of the central bent on the exposed side. At time $t_1 = t_a$ during which the blast wave has come in contact with the structure, the column base at the central pier support is the only point subjected to

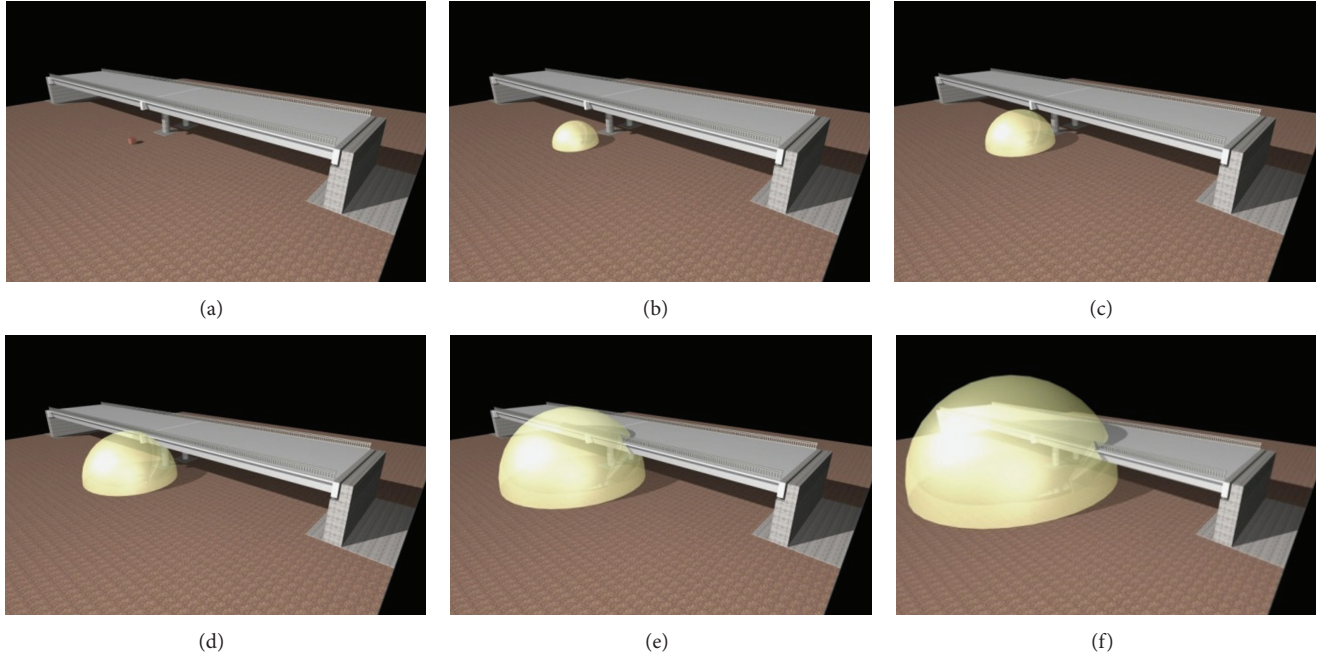


FIGURE 6: Schematic representation of contact of the blast wave with the bridge superstructure.

normal pressure. The intensity of this pressure applied at time t_1 on this point is equal to p_{so1} (Figure 5), whereas the rest of the structure remains unloaded.

During time $t_2 > t_1$, the wave has dilated and comes in contact with a new surface (loading surface) which is defined by the common points that lie on the cross section of the sphere that represents the wave front and the structure (Figure 6(d)) and are also at a distance greater than that of the initial point of contact. This distance depends on the speed of evolution of the blast front. At this instant of time this specific surface is loaded by pressure p_{so2} (Figures 6(c)–6(f)). Simultaneously the initial point is loaded by pressure $p_1 < p_{so1}$, where p_1 is calculated according to the curve of Figure 3, for $t = t_2$. Such surfaces, as they have not been met by the blast front at the time in consideration, remain unloaded.

The same thing holds at time instances, t_3, t_4, \dots, t_n , when the peak pressures occur, $p_{so3}, p_{so4}, \dots, p_{son}$, for n surfaces as they come progressively in contact with the wave front, whereas surfaces through which the wave has already passed are loaded by attenuated pressure magnitudes. These are estimated by the model of pressure variation as shown in Figure 3 after introducing properly the parameter values. Thus each new surface of the structure which is intersected by the spherical wave front is loaded by the peak pressure at the instant of contact, whereas afterwards it continues to be loaded by the pressure estimated from the attenuation relationships until it becomes eliminated.

The set of contact points which are loaded simultaneously is evaluated automatically by calculating their normalized distance from the source based on the assumption that the blast wave evolves at constant speed radially (the geometric distance and the amount of the explosive matter are combined to calculate the normalized distance; this is then

introduced in the corresponding relationships for calculation of pressure at every point in a given time). As illustrated in Figures 6(c)–6(f), there are surfaces in different elements of the structure that are loaded simultaneously.

The speed of the wave front is calculated from the following equation (Ngo et al. [7]):

$$v_s = a_o \cdot \left(\frac{6p_{so} + 7p_o}{7p_{so}} \right)^{1/2}, \quad (10)$$

where p_{so} is the peak positive pressure, p_o is the ambient atmospheric pressure before the explosion, and a_o is the speed of sound at the ambient conditions.

The magnitude of the pressure felt by each surface depends on its position relative to the direction of evolution of the wave front. Surfaces located at the forefront of the wave transmission receive the reflected pressure, whereas all other surfaces receive the incidental pressure (Figure 2).

Calculating in this manner the pressure that acts on the various points of the structure in time, the problem is reduced to a classical problem of structural dynamics which may be solved numerically using established procedures (e.g., with finite elements); the boundary of each finite element lying on the perimeter of the structure is loaded by a time-varying pressure function depending on its distance from the source. The volume of data that must be calculated is proportional to the size and complexity of the structure, and thus significant computing capacity is required for a usual structure. To deal with this problem, in the present investigation, a collection of geometric loci representing the intersection of the advancing hemispherical wave front with the structure were determined at no loss of accuracy. Based on the consecutive,

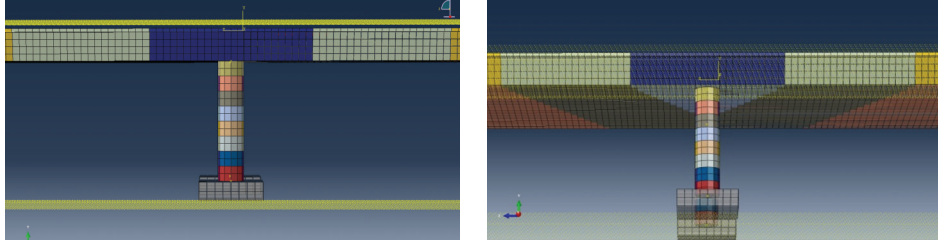


FIGURE 7: Separation of the loading surfaces of column and bridge deck to model the spherical propagation of the blast wave.

time-dependent contact patterns with the bridge depicted in Figure 7, discrete loading surfaces were defined on each critical structural component (i.e., columns and deck surfaces) in order to simulate the wave propagation with time. From the diagram of pressure variation with time depicted in Figure 3 and considering the wave propagation pattern of Figure 6, each loading surface is characterized by a discrete arrival time t_a which depends on the distance from the source and the speed of the wave as estimated by (10). Figure 7 illustrates the loading surfaces defined on the bridge, whereas pressure was taken as constant within each step. The pressure value was set equal to the mean, that is, the value associated with the average distance of the points on the surface of the bridge to the source. For the column, surfaces had a smaller area as initially, after arrival, pressure shows a faster rate of attenuation, whereas for the deck these surfaces were substantially larger as, with increasing time, the rate of pressure reduction drops as illustrated in Figure 3. Based on the above, deck and column surfaces were defined symmetrically around the initial contact point and were discretized into five and eight segments, respectively (Figures 7 and 8(a)). Note that reflected pressure waves affect the surfaces (Figure 8(b)) at the forefront (i.e., front-face of the columns, bottom, and front-face of the bridge deck), whereas the incidental pressure wave affects the sides and back-face of the structure (back-face of the columns, upper surface of the superstructure).

4.2. Proposed Simplifying Methodology. In the present section, a simplifying methodology is proposed for a fast evaluation of blast effects based on the utilization of common analytical tools. In general, such complicated phenomena as blast effects would demand modelling and analytical approaches with significant computational cost. The dynamic nature of the problem, in conjunction with the advanced material constitutive properties, would drive to extremely complicated FE models with very large number of nodes, significant computational cost, and questionable results (e.g., convergence problems during inelastic finite element analysis). Based on the above, a simplifying, easy to use methodology was developed herein in order to reduce the computational cost and at the same time provide reliable solutions based on widely used software packages. The core of the proposed methodology is to define the predominant deformation shape of the structure under the blast wave and then to proceed with ordinary pushover analysis based on simplified, ordinary structural

beam-element models with lumped properties. The entire method may be summarized in the following steps:

- (a) Based on the theoretical background presented herein (Section 2), evaluate all acting pressures on the existing structural elements and their distribution along the bridge deck and substructure.
- (b) Evaluate the structural behavior of all critical components (columns and beams) through the implementation of established analytical methodologies (i.e., moment-curvature section diagrams, shear and axial tension/compression ultimate strength values). The above-mentioned values will be used as an input to the lumped plasticity beam-element model and at the same time will form the failure/yielding criteria for the selection of a valid deformation pattern on the FE model of the next step. Strain rate phenomena should be also considered herein for concrete and steel, based on the provisions of Section 2.2.
- (c) Generate a finite element model (simplified or detailed) and, through the implementation of elastic analytical tools, find the predominant deformation shape of the structure due to blast wave effects at peak dynamic displacement response. The detailed 3D finite element modelling approach presented in Section 4.1 is considered to be the most reliable solution, while other less time consuming strategies would be also acceptable (e.g., the use of 2D elements in widely used commercial software). Considering that the deformation shape is intended for use during a pushover analysis, the selection should correspond to the failure/yielding state of the structure based on appropriate yielding/fracture criteria defined for each critical structural component in the second step.
- (d) Using the evaluated predominant deformation shape of the previous step, proceed with the conventional displacement-based pushover analysis in a simplified beam-element structural model with lumped properties. Detailed section properties and interactions are necessary to be incorporated in the model, based on ordinary structural modelling strategies (Step (b)). In any case, the resulting total force should be equal to or less than the maximum estimated applied force extracted from the FE model.

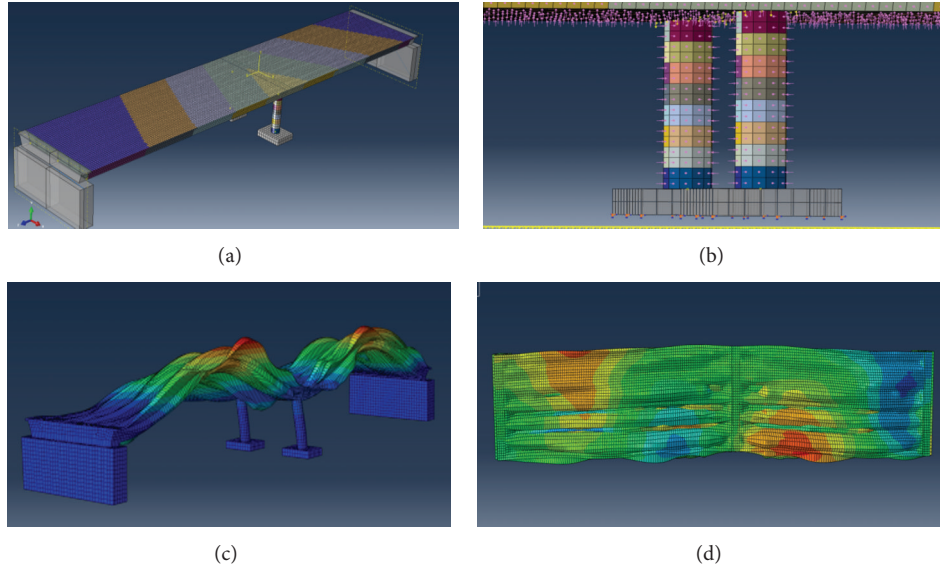


FIGURE 8: FE elastic analysis for a case with monolithic connections in the abutments and central pier. (a and b) Loading surfaces on the structure to model the wave transition. (c and d) Snapshots of the deformed state of the structure at the deck and around the central bent at peak displacement response.

4.3. Predominant Deformation Shape. A key issue for the implementation of the proposed methodology is the estimation of a representative, predominant deformation shape of the structure, under the induced blast loads. For this reason the “predominant” deformation shape is defined herein as the elastic deformation state of the structural system just before brittle failure or yielding of the selected, important for the stability, structural components. Considering the severity of the induced loads and the corresponding instant brittle failures in critical structural components, the above-mentioned deformation shape approximation usually provides representative patterns of force distribution along the structure. Note that local yielding of structural elements under blast loads is rare, while brittle failure modes are usually the dominant pattern of damage. According to the preceding, based on the anticipated failure characteristics of each critical structural component of the bridge (e.g., shear failure, axial force, or moment capacity), the elastic deformation shape is extracted from the implemented FE computational study. For the structural system under examination (post-tensioned concrete bridge), the critical components that control the entire response are the post-tensioned beams as well as the central bent columns and the dominant deformation shape of the system is depicted in Figures 8(c) and 8(d).

4.4. Application to the Model of the Case Study and Results. As it has been already stated in Section 4.2, in order to minimize the computational cost, an elastic analysis (Figure 8(c)) was first conducted in order to determine the “predominant” deformation shape assumed by the structure which was then scaled to yielding in the plastic hinge regions of the central pier columns. The results of the analysis are illustrated in Figure 8 for the peak estimated response. The structure is initially at rest as shown in Figures 8(a) and 8(b), where the loading

surfaces to which the structure has been subdivided are illustrated. Based on the results of the elastic analysis it was found that the most critical pattern of deformation assumed by the structure resembles the shape of the fundamental mode for shaking in the transverse direction (Figures 8(c) and 8(d)). It was found that this pattern occurs while the explosive wave moving from the base pushes the entire structure upwards. In order to proceed with the implementation of the proposed methodology and to extract the response into the nonlinear range without excessive calculation complexity, the simplified nonlinear frame model was assembled for the analysis of the structure. Actually, using the proposed modelling approach, it is possible to reduce the size of the problem, so as to enable the assessment of blast effects on the bridge while using simplified constitutive laws and material properties. Based on the above, the structure was subjected to the evaluated predominant deformation pattern shown in Figure 8(c) after this had been normalized to the peak value so as to represent a shape function (considering the shape shown in Figure 8(c), it may be said here that an analysis resembling in principle the standard “pushover” was attempted, with the approach being motivated from earthquake engineering practices and intended to be used to blast events). Based on the above defined deformation pattern, the intensity of deformation was gradually increased using a step by step nonlinear static procedure. This enabled inelastic state determination at different intensities of displacement of the deck when deforming according to the pattern shown in Figure 8(c). In any case, the resulting total force should be equal to or less than the maximum estimated applied force extracted from the FE model.

Considering that the problem under investigation was reduced into a model comprising typical frame elements, appropriate inelastic hinge properties were evaluated for each

structural component of the model. Based on well-known structural engineering evaluations, a wide range of possible constitutive behaviors (brittle or ductile) were modelled analytically for each existing critical component (shear and axial compression/tension ultimate forces, moment-axial load interaction diagrams, moment-rotation envelopes for lumped plastic hinges, and plastic hinge lengths and moment-curvature relationships for member sections where a more detailed idealization was needed). Objective of this approach was to quantify the extent of damage in terms of values of established stress and strain resultants in the critical elements of the bridge (Figure 9).

From the pushover analysis results it was found that plastic hinges form quickly in the structure, the most immediate being those at the top and the base of the two pier columns. Upon further examination of the estimated values it was concluded that columns would fail by a combination of shear and axial tension (as a result of the upwards pressure applied in the underside of the deck) after flexural yielding in the ends of the members. Considering the brittleness of the estimated mode of failure, the anticipated damage in the column could be extensive depending on the intensity of the blast wave. Beyond that point, a sequential formation of plastic hinges at various points in the structure is observed, owing to the vertical component of the blast wave throughout the span. The deck beams near the abutments and the central pier attain shear failure over an extensive portion of the span; no flexural failure is observed at mid-span suggesting that shear failure precedes flexural modes leading directly to nonproportional damage and collapse.

For the case under consideration, it is evident that, in contrast with ordinary seismic events, blast actions induce excessive loads which are distributed based on significantly different patterns along the superstructure and the substructure elements. Early axial tension and shear brittle failures dominate the response of the entire system, while flexural yielding phenomena, which are commonly considered to be critical in earthquake design practices, seem to be of minor importance.

Based on the above, it is evident that common earthquake design and detailing practices do not cover at all blast actions, as the developed mechanisms are significantly different from those considered in conventional load combinations including earthquake. Therefore, it should be underscored that existing infrastructure elements which are designed based on ordinary structural/earthquake design practices and provisions are vulnerable to significant blast loads and that additional measures need to be taken (active or passive protection) in order to secure the structural integrity of those bridge systems that would be considered critical for continuous functionality in an emergency situation.

5. Conclusions

A simplified modelling procedure for the fast assessment of the effects of blast loads on bridges is proposed. The methodology is a versatile tool for first-order estimation of the effects of blast explosions on structures, which would otherwise require an extensive and complicated nonlinear time history analysis. First the evolving pressure wave front was

Results from inelastic analysis of bridge case study

Early failure of the column joints as a result of axial tension and shear

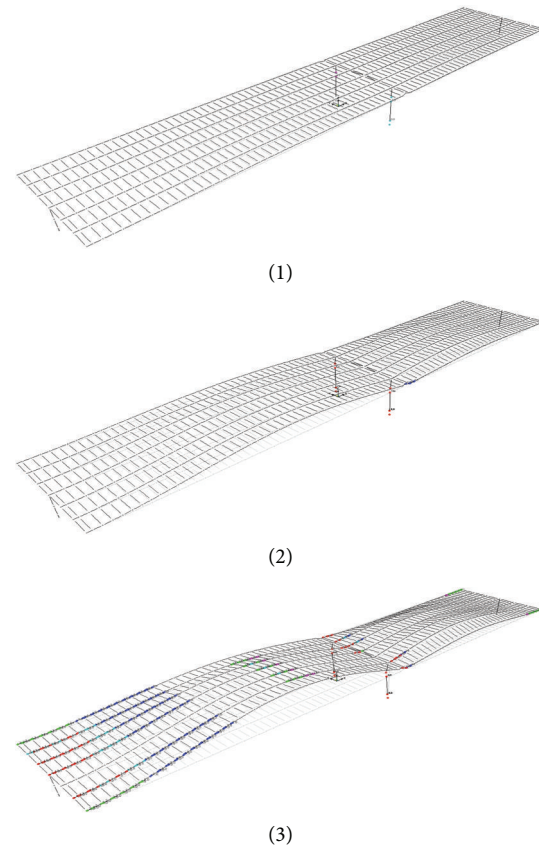


FIGURE 9: Analysis results for a case with fixed supports: monolithic connections in the abutments and central pier (obtained using nonlinear static analysis).

described mathematically in space and time so as to define its loci with the exposed structural surfaces. This enabled definition of the pressure forcing functions on the structure. This was applied using linear dynamic analysis on a detailed elastic finite element model of the structure in order to identify the predominant displacement profile experienced by the structure. Deformations were normalized to the peak response so as to develop a shape function for the bridge structure at the extreme displaced response. The identified displacement pattern was then applied on a nonlinear frame model of the structure. Through this modelling option, nonlinear static analysis was possible at a much reduced computational cost as compared to 3D solid nonlinear finite element modelling which is still, today, prohibitively time-consuming and computationally inaccessible when used to conduct time history investigation of the complete structure; a reason for this is lack of pertinent nonlinear cyclic brick FE models appropriate for modelling 3D solid reinforced concrete structures of realistic complexity, whereas brittle nonlinearity causes insurmountable convergence problems in 3D solid FE models. The frame model was subjected to the identified displacement pattern, with the intensity being increased gradually to

the displacement levels identified by the elastic analysis. Note that the concepts used are extended from earthquake engineering where performance is established from a displacement-based pushover analysis up to the anticipated level of displacement demands. Nonproportional damage is the characteristic consequence of surface, near field explosions such as the example considered in the present study for a two-span typical highway overcrossing. It was found that axial tension as well as shear failure in the columns and deck owing to the excessive displacements caused by the blast having the intensity examined would lead to catastrophic collapse of the bridge. Clearly, blast actions induce severe loads on the structure which are distributed based on different patterns along the superstructure and the substructure elements. Considering that conventional structural and earthquake design fails to provide a solid framework against blast actions, additional measures are necessary to be implemented (e.g., active or passive protection of the system). Based on the simplicity and the reduced computational cost, the proposed method could form the basis for future investigations of blast phenomena as it is intended for a fast assessment procedure of structures subjected to accidental explosions.

Competing Interests

The authors declare that they have no competing interests.

References

- [1] A. K. Agrawal and Z. Yi, *Blast Load Effects on Highway Bridges*, University Transportation Research Center, Department of Civil Engineering, The City College of New York, New York, NY, USA, 2008.
- [2] R. W. Clough and J. Penzien, *Dynamics of Structures*, McGraw Hill, New York, NY, USA, 2nd edition, 1993.
- [3] FEMA 426, *Risk Management Series, Reference Manual to Mitigate Potential Terrorist Attacks Against Buildings*, U.S. Department of Homeland Security, Southwest, Wash, USA, 2003.
- [4] T. H. Birhane, *Blast Analysis of Railway Masonry Bridges*, University of Minho, Braga, Portugal, 2009.
- [5] L. Martin, "Simulation of the effects of an air blast wave," JRC European Commission Technical Notes, 2007.
- [6] W. E. Baker, *Explosions in Air*, University of Texas Press, Austin, Tex, USA, 1973.
- [7] T. Ngo, P. Mendis, A. Gupta, and J. Ramsay, "Blast loading and blast effects on structures—an overview," *Electronic Journal of Structural Engineering*, vol. 7, pp. 76–91, 2007.
- [8] A. K. Pandey, R. Kumar, D. K. Paul, and D. N. Trikha, "Non-linear response of reinforced concrete containment structure under blast loading," *Nuclear Engineering and Design*, vol. 236, no. 9, pp. 993–1002, 2006.
- [9] N. Lam, P. Mendis, and T. Ngo, "Response Spectrum Solutions for Blast Loading," *Electronic Journal of Structural Engineering*, vol. 4, 2004.
- [10] M. L. Javier and R. C. Allen, "Review of strain rate effects for concrete in tension," *ACI Structural Journal*, vol. 95, no. 6, 1998.
- [11] M. L. Javier and C. E. John, "Dynamic increase factors for steel reinforcing bars," in *Proceedings of the 28th DDESB Seminar*, Orlando, Fla, USA, August 1998.
- [12] A. Kotsoglou and S. Pantazopoulou, "Response simulation and seismic assessment of highway overcrossings," *Earthquake Engineering and Structural Dynamics*, vol. 39, no. 9, pp. 991–1013, 2010.
- [13] N. Priestley, F. Seible, and G. M. Calvi, *Seismic Design and Retrofit of Bridges*, John Wiley & Sons, 1996.
- [14] H. Hibbitt, B. Karlsson, and P. Sorensen, *Abaqus Analysis User's Manual. Version 6.9*, Dassault Systemes Simulia Corporation, Providence, RI, USA, 2010.

Review Article

Bioinspired Design of Building Materials for Blast and Ballistic Protection

Yu-Yan Sun,¹ Zhi-Wu Yu,¹ and Zi-Guo Wang²

¹School of Civil Engineering, Central South University, Changsha 410004, China

²College of Resources and Planning Sciences, Jishou University, Zhangjiajie 427000, China

Correspondence should be addressed to Zhi-Wu Yu; 114811003@csu.edu.cn

Received 27 March 2016; Revised 9 July 2016; Accepted 11 July 2016

Academic Editor: Chiara Bedon

Copyright © 2016 Yu-Yan Sun et al. This is an open access article distributed under the Creative Commons Attribution License, which permits unrestricted use, distribution, and reproduction in any medium, provided the original work is properly cited.

Nacre in abalone shell exhibits high toughness despite the brittle nature of its major constituent (i.e., aragonite). Its specific structure is a major contributor to the energy absorption capacity of nacre. This paper reviews the mechanisms behind the performance of nacre under shear, uniaxial tension, compression, and bending conditions. The remarkable combination of stiffness and toughness on nacre can motivate the development of bioinspired building materials for impact resistance applications, and the possible toughness designs of cement-based and clay-based composite materials with a layered and staggered structure were discussed.

1. Introduction

Abalone nacre is the inner layer of abalone shell, which can help to maintain the integrity of the shell under external loads and thus protect the mollusk. Although composed of at least 95% of aragonite by weight, nacre exhibits high toughness which is 1000 times that of the aragonite without compromising strength [1]. Moreover, the ratio of compressive strength to tensile strength of nacre ranges from 1.5 to 3, which is much smaller than those of the conventional monolithic ceramics (range: 8–15) and plain concrete (range: 9–15) [2]. The outstanding mechanical performance of nacre is generally considered to be due to the hierarchical structure of nacre at the nano- and microlevels. Inspired by the structure of nacre, man-made composite materials have been developed with enhanced toughness, such as bioinspired glass and technical ceramic [3–7]. However, very limited work has been carried out to apply this natural principle to the toughness design of building materials such as cement-based and clay-based materials.

This paper discussed the effects of the hierarchical structure on the mechanical behavior of nacre based on the existing publications. Learning the underlying mechanisms of the performance of abalone nacre would help to design nacre-like building materials that combine strength and toughness. When the building was subjected to seismic, impact, or blast

loading, these materials can help reduce the incidences of failures and enhance public safety.

2. Abalone Nacre

2.1. Structure Features. Abalone nacre is a material of hierarchical structure formed by aragonite tablet layers and thin biological organic interlayers, as shown in Figure 1. Each tablet layer consists of polygonal aragonite tablets which are about 5–8 μm in diameter and 0.5 μm in thickness; the spacing between the neighboring tablets is about 5 nm [2]. Moreover, tablets in adjacent layers are slightly staggered rather than stacked randomly or exactly [8]. Transmission electron microscopy (TEM) shows that the surfaces of the aragonite tablets are not flat but significantly wavy, their roughness can reach amplitudes exceeding 200 nm when the average thickness of the tablets was 450 nm, and the waviness of the tablets is highly conformal so that the tablets of adjacent layers fit perfectly together [9].

At the nanoscale, the organic interlayer is about 20–50 nm thick, which is porous and possesses holes of about 50 nm in diameter [2]. Aragonite bridges (Figure 2(a)) connect the aragonite tablet layers through the interlayer [10], and aragonite asperities on the surface of the tablets (Figure 1(c)) form nanoscale islands that are around 30–100 nm in diameter, 10 nm in amplitude, and 60–120 nm apart [11]. Moreover, at the periphery of some tablets, dovetail-like features

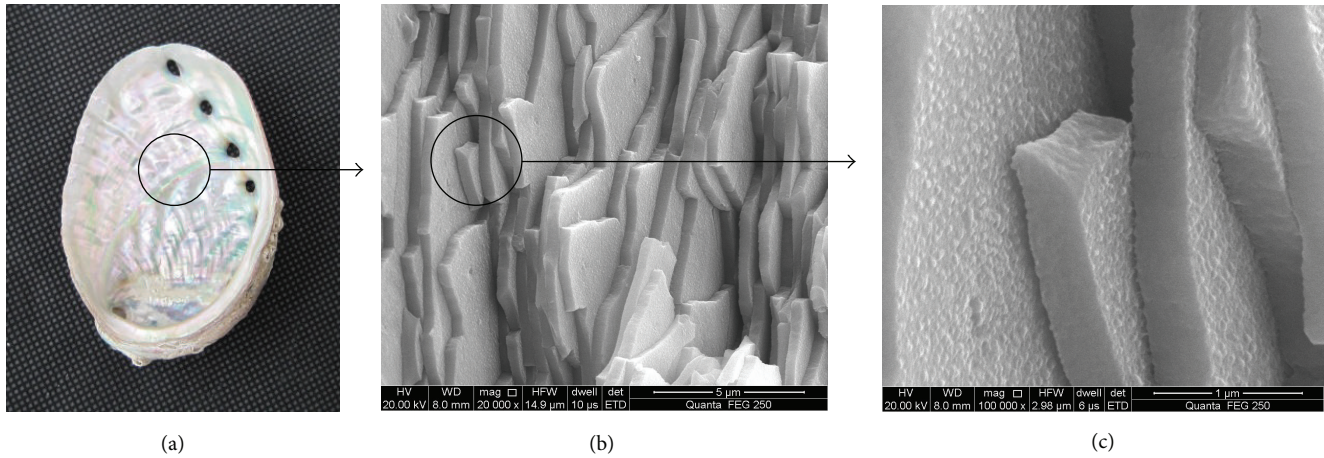


FIGURE 1: The structure of abalone nacre at different length scales: (a) the inside view of an abalone shell, (b) SEM image showing the fractured surface of nacre, and (c) the asperities on the surface of aragonite tablets.

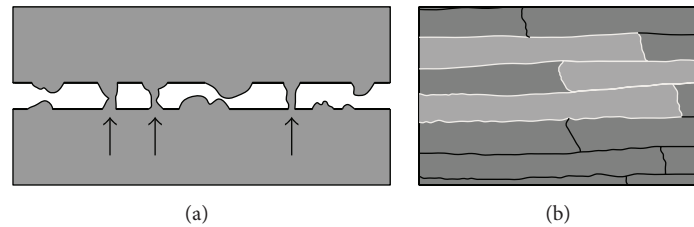


FIGURE 2: Schematic illustrations of (a) aragonite bridges (marked by arrows) between tablets and (b) dovetail-like features at the periphery of tablets.

(Figure 2(b)) generated by the waviness of the interface can be observed in two-dimensional cross sections of nacre [8]. Furthermore, rotated nanograins with an average grain size of 32 nm within the aragonite tablets were found by Li et al. [12] using in situ dynamic atomic force microscope (AFM).

2.2. Mechanical Responses. The outstanding mechanical properties of nacre were first demonstrated by Currey [13] and have been intensively studied over the past two decades. Sarikaya [14] conducted bending tests on red abalone nacre and obtained a fracture toughness of $8 \pm 3 \text{ MPa}\cdot\text{m}^{1/2}$, which is eightfold higher than that of monolithic CaCO_3 and much higher than that of concrete (about $0.2 \text{ MPa}\cdot\text{m}^{1/2}$ [15]). Some experimental data obtained from mechanical tests (e.g., tension, compression, shear, and bending) are collected based on the available references and shown in Table 1. Although the values among different references in Table 1 are slightly or even significantly different probably due to the diversity of lab equipment or specimens, some consistence can still be found: (i) the mechanical response of nacre is anisotropic, depending on the orientation of the imposed forces relative to the surface of the aragonite tablets; (ii) under tension and shear loadings, abalone nacre exhibits relatively large inelastic deformation prior to rupture; (iii) the linear elastic response ($E = 10\text{--}80 \text{ GPa}$) is remarkable, considering low Young's modulus ($2.84 \pm 0.27 \text{ GPa}$ [16]) of the soft interlayer. Moreover, Table 1 also shows that the dynamic compressive strength of nacre is about 50% higher than its quasi-static compressive strength.

2.3. Underlying Mechanisms

2.3.1. Shear. Table 1 shows that the shear strength of abalone nacre is much lower than the compressive and tensile strengths but accompanied by a relatively large inelastic deformation. It appears that the shearing of interfaces between tablets dominates the shear resistance and deformation mechanism of nacre. When subjected to shear loading, the interfaces yield first followed by the relative sliding of tablet layers [18]. The microscale waviness of the tablets may act as obstacles to the tablets sliding, and a transverse expansion of the tablets is generated due to the compression (Figure 3(a)), which can further hinder the tablets sliding. These mechanisms are favorable for nacre to initiate new sliding sites, uniformly distribute inelastic strains, and mitigate damage localization.

Wang et al. [11] reported that the asperities on the surface of the tablet were the principal source of the shear resistance of nacre and also a major contributor to its initial strain hardening. However, the significance of the asperities was not supported by Barthelat et al. [16], since the sliding distance attributed to the asperities (20–25 nm) is much smaller than the observed tablet sliding distance (100–200 nm) under shear loading.

The thin porous organic material in nacre is traditionally regarded as glue to maintain the cohesion of the tablets over a large separation distance [11, 19]. However, Meyers et al. [2] reported that the primary role of the organic layer on the mechanical behavior of nacre was to subdivide the aragonite matrix into tablets, and the glue effect was not significant.

TABLE 1: Some experimental data collected from literature on abalone nacre.

Reference	Test	σ_1 /MPa	σ_2 /MPa	ε_t /%	E /GPa
[17]	Quasi-static compression	540	235
	Dynamic compression	735	548
	Shear	...	30	45	...
	Three-point bending	197	177
[11]	Shear-compression*	73	...	8	...
	Three-point bending	223 ± 7	194 ± 8	...	69 ± 7
	Four-point bending				
	Compressive	370	70
	Tensile	105	...	1	60
[12]	Tension	1-5	...
[9]	Shear	...	50	15	10
	Shear-compression*	60	...	1.5	...
[1]	Tension	...	90	1	80

σ_1 and σ_2 : the strength obtained from loading perpendicular and parallel to the tablets surface plane, respectively.

E : Young's modulus.

ε_t : inelastic strain.

*The strength obtained with the boundaries at 45° to the load axis.

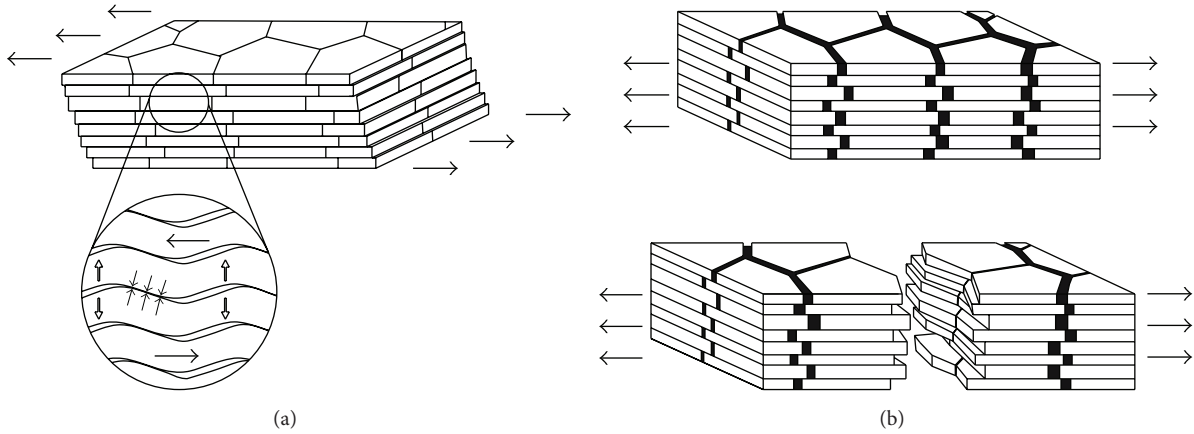


FIGURE 3: (a) Deformation mechanism of nacre under shear stresses; (b) deformation mode of nacre under tensile stresses.

2.3.2. Tension. The response of abalone nacre to tension is critical to prevention of pullout failure. Under tensile loading applied along the tablet plane (Figure 3(b)), the strain hardening rate and observed tablet sliding distance are both less than those in shear, as in tension the shearing interfaces (overlap areas) account for only 30% of the interface area. The inelastic deformation spreads over large volumes around cracks and defects, which generates many “white tension lines” [11].

The dovetail-like feature at the end of some tablets is generally considered as a key contributor to nacre's performance in tension, as it can generate progressive interlocking and lead to a triaxial state of stress in the sliding region to impede the tablet separation [8]. However, Barthelat and Espinosa [1] reported that the angle of the dovetails was rather small (about $1-5^\circ$), so that the locking and hardening functions were weak.

Song et al. [20] reported that the mineral bridges between tablet layers significantly reinforced the weak organic inter-

layers and consequently enhanced the tensile strength of nacre. However, Lin and Meyers [21] disapproved of the existence of such mineral bridges, and Katti et al. [22] concluded that the mineral bridges had marginal effect on both linear and nonlinear responses in nacre, as the mineral contacts broke long before yield initiated in nacre.

The results of tension test conducted by Li et al. [12] showed that the rotation and deformation of nanograins significantly benefitted the energy dissipation in nacre. However, Barthelat et al. [9] pointed out that the primary role of the nanograins was to preserve the tablet integrity in the deformation process rather than directly influence the overall deformation in nacre.

2.3.3. Compression. When nacre is subjected to compressive loading that is perpendicular to the tablet surface plane, the failure occurs gradually due to crack deflection along the organic interlayer [17]. The mechanism is that if a crack occurs and attempts to pass through the nacre, its direction

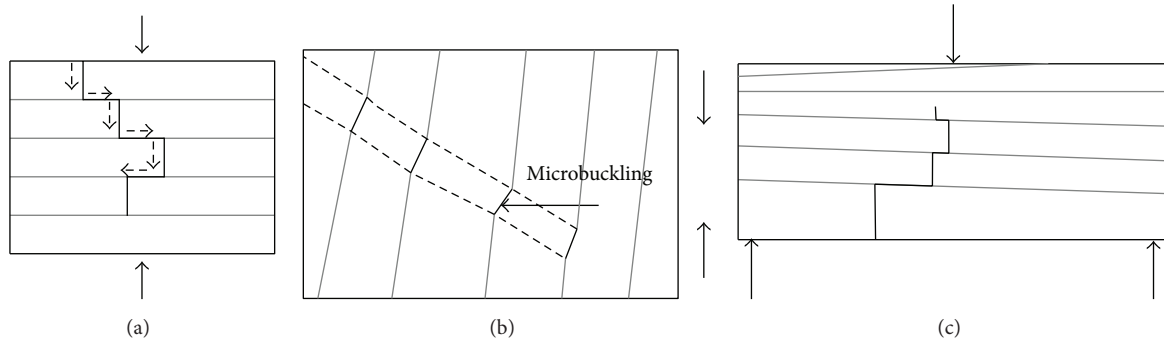


FIGURE 4: Schematic illustrations of (a) crack deflection along organic layers of nacre under compression, (b) microbuckling in nacre under compression (parallel), and (c) crack deflection in an abalone shell under three-point bending.

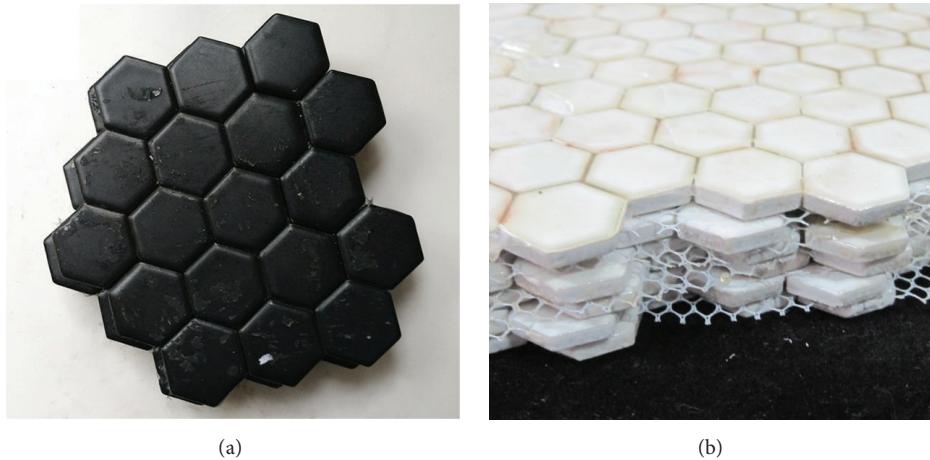


FIGURE 5: (a) A building ceramic composite sample with a layered and staggered structure; (b) the side view of a composite sample.

will be forced to change along the weak protein layers rather than develop rapidly through the relatively stiff tablets. As such, a tortuous path will be formed, and a single sharp crack will be replaced by a large number of small cracks within a broad region (Figure 4(a)), which disperses the imposed force and alleviates stress concentrations. When the compressive loading is parallel to the tablets surface plane, the value of compressive strength is lower than that in perpendicular condition, which can be explained by the microplastic buckling (Figure 4(b)).

2.3.4. Bending. When an abalone shell is subjected to a localized pressure normal to the outer shell surface, the overall shell can be idealized as experiencing bending stress. In this situation, the hard outer layer of the shell is in compression and the inside nacreous layer is in tension (Figure 4(c)); thus the damage mechanisms for abalone shell in bending may involve the compressive and tensile strengths of outer and inner shells, respectively.

3. Toughness Design for Building Materials

Cement-based and clay-based materials such as concrete and building ceramic tiles are commonly used as construction materials in civil engineering. Although they can possess high compressive strength, they are susceptible to catastrophic

failure due to their inherent brittleness. Inspired by the fracture mechanisms of nacre, we suggest that cement-based and clay-based building composites having a layered and staggered structure like nacre may have improved fracture toughness. To achieve this structure, thin and weak interlayers should be introduced in the building composite to facilitate layer sliding and deflect growing cracks, and the hard layers should be partitioned into multiple tiles to prevent fracture surfaces crossing the entire layer. Besides, the ratio of length to thickness of an individual tile should be high enough to enhance interlayer cohesion but not too high to cause premature tile failure.

Authors of this paper have recently studied the impact response of the building ceramic composite with a nacre-like structure by drop weight test and also explored the potential use of this ceramic composite as protective covering on concrete against high-speed projectile impact [23]. The layered and staggered structure of the composite consisted of building ceramic mosaic tiles (CMTs) and soft adhesive, which mimic the stiff aragonite tablets and the organic material in nacre, respectively (see Figure 5). The experimental results showed that this ceramic composite exhibited significantly improved impact resistance compared with the simple layered ceramic composite consisting of nonpartitioned tile layers and concrete targets with the protective

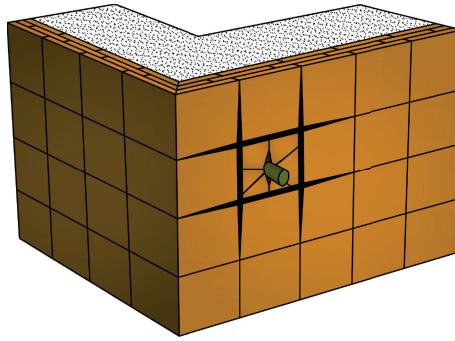


FIGURE 6: The protective covering on concrete member can confine the crater damage within the impacted tile.

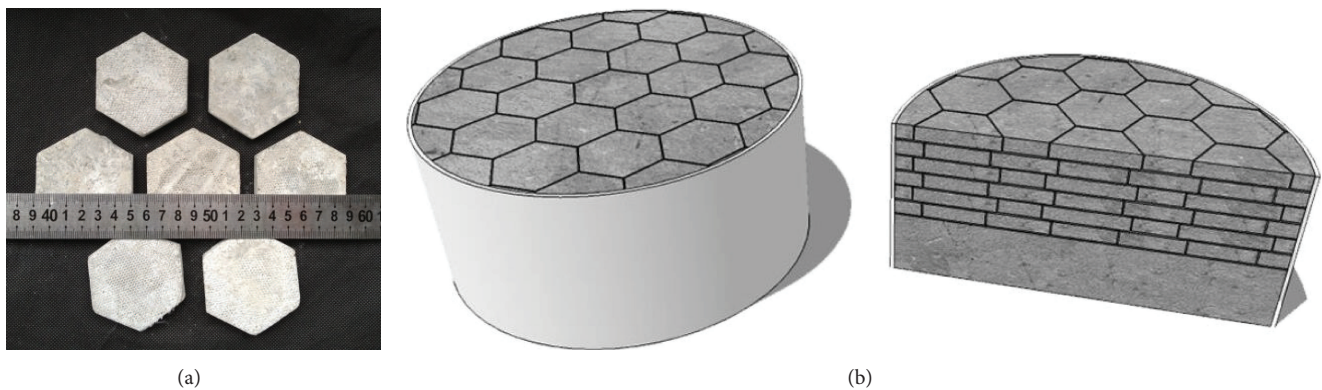


FIGURE 7: (a) Concrete tiles of hexagonal shape; (b) schematic illustrations of concrete target with cement-based composite protective covering.

covering displayed superior integrity and highly reduced penetration depth compared with those without protective covering. Since the CMTs in the building materials market have various sizes, shapes, and thicknesses, they will favor the future experimental studies on the optimal polygon shape, aspect ratio, and overlap length of the tiles in the layered and staggered structural composites.

According to the ballistic test results in [23], the penetration depth of the projectile in concrete can be reduced by up to 77.3% in the presence of the protective covering. That means the design thickness of the concrete member under protection can be greatly decreased, which will help to lower the costs of the concrete material. Besides, as the crushed tile can be separated from the adjacent tiles while confining the radial cracks within the impacted tile when the adhesive possesses a relative large elongation at break (see Figure 6), the repair costs in war time will be decreased. However, the selling price of CMTs is about 70 RMB/m², which is higher than that of concrete; although only a small amount of adhesive material is required to prepare the building ceramic composite, the unit prices of both epoxy adhesive and silicone sealant are relatively high; additionally, the production procedures of the building ceramic composite are complex; therefore, the material and construction costs may limit the application of the composite. To reduce the

material costs, it is necessary to find alternative materials, and the cement-based material is a good choice due to its relatively low cost and high strength.

The impact resistance of multilayer cement-based composites has been studied in recent years [24, 25]. It was reported that the layered or functionally graded cement-based composites showed better performance against high velocity impact compared with the monoblock cement-based materials. However, the layered structure was not sufficient to provide inelastic deformation. Learning from nacre, cement-based composite can be designed into a layered and staggered structure by using concrete or mortar tiles (Figure 7(a)), and such composite may also be used as a protective covering on concrete against impact loading (Figure 7(b)). Moreover, properties of the thin interlayer materials can affect the failure behaviors of the composites: rigid interlayers (such as cement mortar with high elastic modulus) can facilitate energy transmission but reduce the multihit capability of the composites; elastic interlayer (such as rubberized mortar with low elastic modulus) is able to support large deformation but at a cost of decreased stiffness of the composite. Therefore, the choice of the interlayer material should depend on the loading condition and service requirements of the composite. The efficacy of the cement-based composite protective covering needs to be investigated in the further studies.

4. Conclusion

Nacre in abalone shell, consisting mainly of brittle aragonite, shows high toughness and remarkable inelasticity. Mechanisms at distinct length scales contribute to the overall mechanical responses of nacre. At the microlevel, the well-formed hierarchical structure of nacre can deflect cracks and prolong the crack propagation, which consumes a significant amount of energy; at the nanoscale, tablet sliding is considered the prominent inelastic deformation mechanism.

The structure of nacre can serve as a biomimetic model for the toughness design of cement-based and clay-based building composite materials. This structure can lead to deflection of cracks and delay failure of the composite. The building ceramic composite with a nacre-like structure showed improved impact resistance, and it also has the potential to be used on structural surface and subsurface for blast and ballistic protection. The efficacy of concrete with a layered and staggered structure for impact resistance application needs further investigation.

Competing Interests

The authors declare that they have no competing interests.

References

- [1] F. Barthelat and H. D. Espinosa, "An experimental investigation of deformation and fracture of nacre-mother of pearl," *Experimental Mechanics*, vol. 47, no. 3, pp. 311–324, 2007.
- [2] M. A. Meyers, A. Y.-M. Lin, P.-Y. Chen, and J. Muyco, "Mechanical strength of abalone nacre: role of the soft organic layer," *Journal of the Mechanical Behavior of Biomedical Materials*, vol. 1, no. 1, pp. 76–85, 2008.
- [3] G. Mayer, "New classes of tough composite materials—lessons from natural rigid biological systems," *Materials Science and Engineering: C*, vol. 26, no. 8, pp. 1261–1268, 2006.
- [4] E. Munch, M. E. Launey, D. H. Alsem, E. Saiz, A. P. Tomsia, and R. O. Ritchie, "Tough, bio-inspired hybrid materials," *Science*, vol. 322, no. 5907, pp. 1516–1520, 2008.
- [5] I. Corni, T. J. Harvey, J. A. Wharton, K. R. Stokes, F. C. Walsh, and R. J. K. Wood, "A review of experimental techniques to produce a nacre-like structure," *Bioinspiration and Biomimetics*, vol. 7, no. 3, Article ID 031001, 2012.
- [6] F. Bouville, E. Maire, S. Meille, B. Van De Moortèle, A. J. Stevenson, and S. Deville, "Strong, tough and stiff bioinspired ceramics from brittle constituents," *Nature Materials*, vol. 13, no. 5, pp. 508–514, 2014.
- [7] S. M. M. Valashani and F. Barthelat, "A laser-engraved glass duplicating the structure, mechanics and performance of natural nacre," *Bioinspiration and Biomimetics*, vol. 10, no. 2, Article ID 026005, 2015.
- [8] H. D. Espinosa, J. E. Rim, F. Barthelat, and M. J. Buehler, "Merger of structure and material in nacre and bone—perspectives on *de novo* biomimetic materials," *Progress in Materials Science*, vol. 54, no. 8, pp. 1059–1100, 2009.
- [9] F. Barthelat, H. Tang, P. D. Zavattieri, C.-M. Li, and H. D. Espinosa, "On the mechanics of mother-of-pearl: a key feature in the material hierarchical structure," *Journal of the Mechanics and Physics of Solids*, vol. 55, no. 2, pp. 306–337, 2007.
- [10] F. Song, X. H. Zhang, and Y. L. Bai, "Microstructure and characteristics in the organic matrix layers of nacre," *Journal of Materials Research*, vol. 17, no. 7, pp. 1567–1570, 2002.
- [11] R. Z. Wang, Z. Suo, A. G. Evans, N. Yao, and I. A. Aksay, "Deformation mechanisms in nacre," *Journal of Materials Research*, vol. 16, no. 9, pp. 2485–2493, 2001.
- [12] X. D. Li, Z.-H. Xu, and R. Z. Wang, "In situ observation of nanograin rotation and deformation in nacre," *Nano Letters*, vol. 6, no. 10, pp. 2301–2304, 2006.
- [13] J. D. Currey, "Mechanical properties of mother of pearl in tension," *Proceedings of the Royal Society of London B—Biological Sciences*, vol. 196, no. 1125, pp. 443–463, 1977.
- [14] M. Sarikaya, "An introduction to biomimetics: a structural viewpoint," *Microscopy Research and Technique*, vol. 27, no. 5, pp. 360–375, 1994.
- [15] W. D. Callister, *Materials Science and Engineering: An Introduction*, John Wiley & Sons, New York, NY, USA, 5th edition, 2000.
- [16] F. Barthelat, Ch.-M. Li, C. Comi, and H. D. Espinosa, "Mechanical properties of nacre constituents and their impact on mechanical performance," *Journal of Materials Research*, vol. 21, no. 8, pp. 1977–1986, 2006.
- [17] R. Menig, M. H. Meyers, M. A. Meyers, and K. S. Vecchio, "Quasi-static and dynamic mechanical response of *Haliotis rufescens* (abalone) shells," *Acta Materialia*, vol. 48, no. 9, pp. 2383–2398, 2000.
- [18] M. Sarikaya, K. E. Gunnison, M. Yasrebi, and I. A. Aksay, "Mechanical property-microstructural relationships in abalone shell," *MRS Proceedings*, vol. 174, pp. 109–116, 1989.
- [19] B. L. Smith, T. E. Schäffer, M. Vlani et al., "Molecular mechanistic origin of the toughness of natural adhesives, fibres and composites," *Nature*, vol. 399, no. 6738, pp. 761–763, 1999.
- [20] F. Song, A. K. Soh, and Y. L. Bai, "Structural and mechanical properties of the organic matrix layers of nacre," *Biomaterials*, vol. 24, no. 20, pp. 3623–3631, 2003.
- [21] A. Lin and M. A. Meyers, "Growth and structure in abalone shell," *Materials Science and Engineering: A*, vol. 390, no. 1-2, pp. 27–41, 2005.
- [22] K. Katti, D. R. Katti, J. Tang, S. Pradhan, and M. Sarikaya, "Modeling mechanical responses in a laminated biocomposite," *Journal of Materials Science*, vol. 40, no. 7, pp. 1749–1755, 2005.
- [23] Y. Sun, Z. Yu, Z. Wang, and X. Liu, "Novel protective covering to enhance concrete resistance against projectile impact," *Construction and Building Materials*, vol. 96, pp. 484–490, 2015.
- [24] S. T. Quek, V. W. J. Lin, and M. Maalej, "Development of functionally-graded cementitious panel against high-velocity small projectile impact," *International Journal of Impact Engineering*, vol. 37, no. 8, pp. 928–941, 2010.
- [25] M. Mastali, M. Ghasemi Naghibdehi, M. Naghipour, and S. M. Rabiee, "Experimental assessment of functionally graded reinforced concrete (FGRC) slabs under drop weight and projectile impacts," *Construction and Building Materials*, vol. 95, pp. 296–311, 2015.

Review Article

Design of Blast-Loaded Glazing Windows and Facades: A Review of Essential Requirements towards Standardization

**Martin Larcher,¹ Michel Arrigoni,² Chiara Bedon,³ J. C. A. M. van Doormaal,⁴
Christof Haberacker,⁵ Götz Hüsken,⁶ Oliver Millon,⁷ Arja Saarenheimo,⁸ George Solomos,¹
Laurent Thamie,⁹ Georgios Valsamos,¹ Andy Williams,¹⁰ and Alexander Stolz⁷**

¹ European Commission, Joint Research Centre, European Laboratory for Structural Assessment (ELSA), 21027 Ispra, Italy

² Faculty of Engineering, Department of Civil Engineering and Architecture, University of Trieste, 34127 Trieste, Italy

³ ENSTA Bretagne, IRDL FRE No. 3744, 29806 Brest Cedex 09, France

⁴ TNO Prins Maurits Laboratory, P.O. Box 45, 2280AA Rijswijk, Netherlands

⁵ Bundeswehr Technical Centre for Protective and Special Technologies (WTD 52), 83458 Schneizdreuth, Germany

⁶ BAM Federal Institute for Materials Research and Testing, Unter den Eichen 87, 12205 Berlin, Germany

⁷ Fraunhofer Institute for High-Speed Dynamics, Ernst Mach Institute, EMI, Eckerstraße 4, 79104 Freiburg, Germany

⁸ VTT, Vuorimiehentie 3, 02150 Espoo, Finland

⁹ CEA-Gramat, 46500 Gramat, France

¹⁰ Home Office Centre for Applied Science and Technology, Horsham RH12 4WX, UK

Correspondence should be addressed to Martin Larcher; martin.larcher@jrc.ec.europa.eu

Received 22 April 2016; Accepted 30 June 2016

Academic Editor: Dimitris Rizos

Copyright © 2016 Martin Larcher et al. This is an open access article distributed under the Creative Commons Attribution License, which permits unrestricted use, distribution, and reproduction in any medium, provided the original work is properly cited.

The determination of the blast protection level of laminated glass windows and facades is of crucial importance, and it is normally done by using experimental investigations. In recent years numerical methods have become much more powerful also with respect to this kind of application. This paper attempts to give a first idea of a possible standardization concerning such numerical simulations. Attention is drawn to the representation of the blast loading and to the proper description of the behaviour of the material of the mentioned products, to the geometrical meshing, and to the modelling of the connections of the glass components to the main structure. The need to validate the numerical models against reliable experimental data, some of which are indicated, is underlined.

1. Introduction

The recent terrorist attacks have shown that explosions could result in a massive failure of windows as seen in the terrorist attack in Oslo in 2011 (Figure 1). Glass is used in modern architecture widely as a part of facades often in combination with a steel substructure. However, glass is in general also the most fragile part of a structure and its failure results in splinters that could seriously injure persons inside the building. The windows of critical buildings and in general of critical infrastructure can be strengthened (and their protection increased), for example, by using laminated glass. This kind of intervention and the resulting enhanced protection

can be identified in Figure 1, where some windows in the 5th floor have not failed.

The particular vulnerability of glass is shown in the investigation of the Oklahoma City attack by Norville et al. [1]. In this study, a very large risk zone has been identified, where windows fail and their splinters could potentially injure people. Concerning explosion-induced injuries, the risk due to the primary blast effects on humans (Figure 2) is already described quite well by several authors [2]. However, this is not yet the case for secondary blast effects, which are due to the fragments propelled with high velocities and strike the human body. A relevant example of large scale explosion in a dense urban environment is the explosion of the AZF factory



FIGURE 1: Terrorist attack in Oslo in 2011, failure of windows (from [5]).

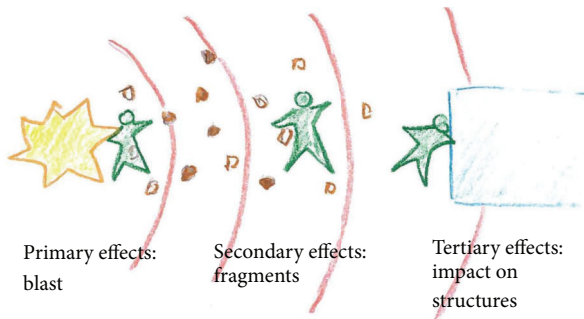


FIGURE 2: Blast effects on humans (green), explosion (yellow), fragments (brown), and blast wave (red).

in Toulouse, France, in 2001, where more than 3000 people were injured, mainly by splinters [3]. This is an area of interest and of intense research. A straightforward procedure for assessing the additional risk due to the splinters as part of the secondary blast effects is currently under development [4].

(1) Numerical Simulations on Blast-Loaded Glass Systems. Several numerical investigations with various models concerning laminated glass have been conducted. Müller and Wagner [6] have shown that a layered shell element can represent the failure behaviour of laminated glass quite well. Simplified models are given by Timmel et al. [7] and Sun et al. [8] that apparently do not represent all failure mechanisms of laminated glass.

Some authors (Zhang and Hao [9], Bennison et al. [10], and Hidallana-Gamage et al. [11]) have presented 3D models with solid elements which allow use of a detailed material law for the interlayer. The number of degrees of freedom in this modelling increases rapidly. Examples and calculations with failure criteria of conventional glass are shown, for example, by Müller and Wagner [6] and Burmeister [12].

Several additional effects concerning laminated glass windows have also been investigated numerically. According to Zhang and Hao [9], the influence of the boundary

conditions is very big. Therefore, a detailed modelling of the connection between the glass and the rigid structure, to which the window or facade is connected, is essential. The possible delamination of the laminated glass is investigated by Pelfrene et al. [13] using a combined shell-solid model. It is found that, depending on the polyvinyl butyral (PVB) interlayer, delamination could have a significant influence on the failure behaviour.

The classification and design of blast-loaded windows is performed, as a rule, by experimental investigations. Zhang et al. [14] present some preliminary PI-formulas that can be used for a predesign. The formulas are derived by using parametric studies with finite element simulations. However, since the design of such protection is often security relevant, there is no information about the degree of incorporation of such numerical design in engineering practice. As described below, numerical simulations could replace some of the expensive experimental work and could add further possibilities concerning parametric studies.

(2) Existing Standards for Blast-Resistant Glass Windows. The European Committee for Standardization (CEN) published the first standards for testing blast-resistant glazing in 2001. These include a European standard (EN) for testing security glazing alone (EN 13541:2012) and a suite of standards for testing complete systems like windows, doors, and shutters (EN 13123-1:2001, EN 13123-2:2004, EN 13124-1:2001, and EN 13124-2:2004). Currently, there are no standards for testing glazed facades. EN 13541:2012 considers only a single pane of glass with a single fixed size in a rigid frame under prescribed tests and boundary conditions. EN 13123-1:2001 and EN 13123-2:2004 consider the whole window system and permit it to be tested at its real size and with its real frame, thus producing more realistic results. These standards make provision for testing with a shock tube and arena testing with small charges. The United States (US) government General Service Administration (GSA) published a test protocol for glazing in 2003 (GSA-TS01:2003), which permits testing by shock tube or range test. The International Organisation for Standardization (ISO) published in 2007 the standard ISO 16933:2007. This is largely based on the EN standards. It extends the test conditions to allow the use of large charges in range tests and it also includes additional small charges to encompass the GSA test requirements. A parallel standard (ISO 16934:2007) covers shock-tube testing.

(3) Objectives and Open Challenges. Apparently, no standardized procedure is defined on how numerical approaches could be used to support the design of laminated glass or windows. Despite the fact that numerical simulations of blast-loaded windows or facades could present many difficulties, numerical simulations are currently employed in order to design such kind of structures. Thus, in order to reduce possible faults and misinterpretations, a standardized procedure for numerical simulations would be helpful. This work presents elements in order to draw a standardized procedure in the future.

In this direction, this review paper is structured in the following way. Current design tools of blast-loaded glass

structures are first described in Section 2, both in a classical way and in respect of the possible consistent use of numerical simulations. The procedure of a numerical simulation in that field is then described in Section 3, where the definition of critical parts of such simulation is included. The validation and the possible assessment of the performance of blast-loaded glazing systems are then presented in Section 4. Finally, some conclusions and a presentation of possible next steps towards standardization are given in Section 5.

2. Design of Blast-Loaded Windows

The design of the protection of critical infrastructure (in particular where glass elements are of concern) against terrorist attacks is usually done along the following lines:

- (i) The first step is to determine scenarios. This is a joint decision of the owner or stakeholder and the designer. Risk assessment could be an appropriate tool for defining and choosing possible scenarios. An indication is given, for example, by the North Atlantic Treaty Organization's (NATO) Standardization Agreement (STANAG) 2280 [21].
- (ii) The next step is to calculate the corresponding loads on the structure by identifying the worst case scenario. This can be done for some cases by simple formulas for the blast wave propagation, by using, for example, the Kingery-Bulmash equations [22] and the Kinney and Graham's equation [23] or by using series of abacus proposed in Unified Facilities Criteria such as UFC 3-340-2 [24]. A comparison of these equations with experimental data is done by Bogosian et al. [25]. The situation may be much more complicated in urban environment since the blast propagation is not any more spherical. Numerical simulations may then be necessary and adequate to calculate the possible loading of a structure, as shown in [26].
- (iii) The call for tender must include the specifications in order to protect the windows or facades against the blast load. This means that maximum pressure and impulse values must be specified and the way to provide evidence of meeting these requirements must be defined. Several possibilities (numerical, experimental) can be taken into account, as shown in [27].
- (iv) The tenderer will in most of the cases consult a specialized design office that can provide the evidence (based on product specifications, experiments, or calculations) that a particular windows system is indeed protecting against the specified maximum loading.

2.1. Numerical Simulation for Blast-Loaded Windows. Even if there are several open questions in numerical simulations for blast-loaded laminated glass, there are strong reasons that they could help in the engineer's work. The interaction between numerical simulations and their verification, validation, and the approval of a design by experiments can be described as shown in Figure 3.

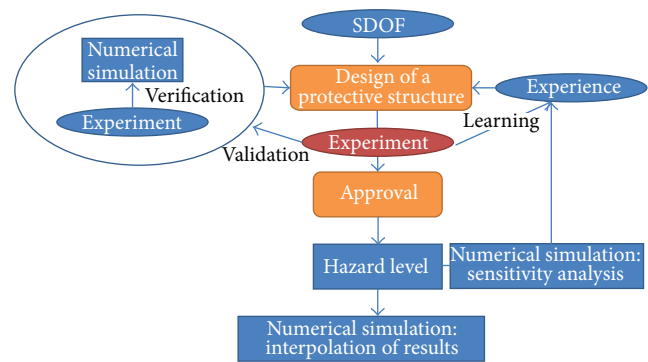


FIGURE 3: Interaction between numerical simulations and experiments for the approval of protective structures using laminated glass.

Several other arguments can also be cited for employing numerical simulations in the protection design involving glass products.

Numerical simulations can help to *understand the behaviour of the structure*. While detailed experimental investigations are not easy to perform, numerical simulations can close that gap. Numerical simulations may help to develop new kind of materials or structures. These structures can be tested numerically before expensive experiments are conducted. Numerical simulations can help to investigate the different *parameters of the windows for the design*. When a set of experiments is conducted either to demonstrate the protection of the window or to validate the numerical simulation, the simulation can then be used to investigate, for example, other sizes of the glass sheets. In this way, experimental results can be extended to similar configurations by numerical simulations. Hence also the number of field experiments can be reduced by using numerical simulations. While an experimental investigation captures mainly one scenario or even only one pressure-time curve representing that scenario, numerical simulations can be used to investigate a *multiplicity of threat scenarios*. The place of the charge and its size can be varied easily to see the influence of those parameters. Also much larger structures can be taken into account, like whole facades, and different types of facades could be tested, such as with steel-frame or cable-net supporting structures. Further, experimental investigations must be designed in advance to know the possible failure modes. Numerical simulations can support this process either to *design a shock tube for testing windows* or for *designing the substructure* for laminated glass in case of *arena tests*.

Undoubtedly, experimental research is needed in order to understand the physical phenomena when choosing the appropriate modelling techniques and material laws. Further dedicated material tests are needed to obtain relevant material parameters for the material models.

Apart from the more sophisticated finite element techniques, another numerical method is given by the single-degree-of-freedom oscillator method (SDOF), where the window is represented by a single mass and a special stiffness (Fischer [28, 29]). A large number of experimental results are used to get data in order to model the nonlinear stiffness

TABLE 1: Hazard-rating criteria for arena tests according to ISO 16933:2007 [15].

Hazard rating	Hazard-rating description	Definition
A	No break	The glazing is observed not to fracture and there is no visible damage to the glazing system
B	No hazard	The glazing is observed to fracture but the inner, rear face leaf is fully retained in the facility test frame or glazing system frame with no breach and no material is lost from the interior surface; outer leaves from the attack face may be sacrificed and may fall or be projected out
C	Minimal hazard	The glazing is observed to fracture; outer leaves from the attack face may be sacrificed and may fall or be projected out; the inner, rear face leaf shall be substantially retained, with the total length of tears plus the total length of pull-out from the edge of the frame less than 50% of the glazing sight perimeter Also, there are no more than three rateable perforations or indents anywhere in the witness panel and any fragments on the floor between 1 m and 3 m from the interior face of the specimen have a sum total united dimension of 250 mm or less; glazing dust and slivers are not accounted for in the hazard rating If by design intent there is more than 50% pull-out but the glazing remains firmly anchored by purpose-designed fittings, a rating of C (minimal hazard) may be awarded, provided that the other fragment limitations are met; the survival condition and anchoring provisions shall be described in the test report
D	Very low hazard	The glazing is observed to fracture and significant parts are located no further than 1 m behind the original location of the rear face; parts are projected any distance from the attack face towards the blast source Also, there are no more than three rateable perforations or indents anywhere in the witness panel, and any fragments on the floor between 1 m and 3 m from the interior face of the specimen have a sum total united dimension of 250 mm or less; glazing dust and slivers are not accounted for in the rating
E	Low hazard	The glazing is observed to fracture, and glazing fragments or the whole of the glazing falls between 1 m and 3 m behind the interior face of the specimen and not more than 0.5 m above the floor at the vertical witness panel Also, there are 10 or fewer rateable perforations in the area of the vertical witness panel higher than 0.5 m above the floor and none of the perforations penetrate more than 12 mm
F	High hazard	Glazing is observed to fracture and there are more than 10 rateable perforations in the area of the vertical witness panel higher than 0.5 m above the floor, or there is one or more perforations in the same witness panel area with fragment penetration more than 12 mm

properties of the spring. Obviously the SDOF method cannot replace experimental investigations for a more complex design.

2.2. Expectations from Numerical Simulations. European, ISO, and American testing standards for laminated glass windows (e.g., [15]) define a hazard level that is assessed and measured by the damage state of the glass pane and the position of the glass fragments that are found after the experiment behind the glass pane. More details can be found in US General Services Administration [30] and ISO standard [15] (Table 1) and also in [29, 31].

With respect to these criteria, scientific and technical literature has shown that numerical simulations can be used with confidence to determine the failure of the laminated glass and its interlayer and may be useful to approximate the launch conditions of the splinters [4]. The bearing capacity and the glazing damage level of the window of full window systems and their components could also be adequately determined by numerical simulations. However, the prediction of the formation and development of splinters or slivers of

blast-loaded laminated glass has until now not been accurate enough and is a challenge for numerical simulations. Also the splinter velocity and dispersion behind the window cannot be determined numerically.

2.3. Selection of Representative Load Scenarios. The loading scenario depends on the specific protection requirements and local conditions. Detailed instructions for defining loading scenarios are given in national regulations or must be discussed with the infrastructure operator/owner or the responsible authorities. Attack scenarios to be considered in designing a structure are usually expressed in terms of equivalent mass of Trinitrotoluene (TNT) and stand-off distance, for example, the distance between the structure to be designed and the postulated explosion source. An indication of the size of the charge can be taken from [21]. Different TNT equivalents for other explosives like, for example, pentaerythritol tetranitrate (PETN), are given by [32].

In general, numerical simulations are able to handle an almost arbitrary loading scenario for the structural element considered. Taking these capabilities concerning loading into

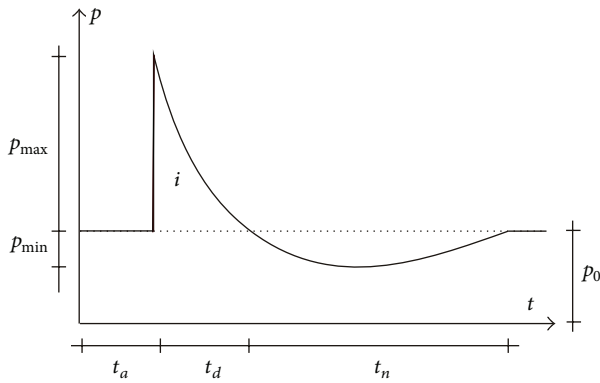


FIGURE 4: Pressure history for a free-field air-blast wave.

account, it is important to ensure that the modelled scenarios can be compared to the experimental results. For this, it would be necessary to capture the actual loading of the structural component examined with the same logic as in the experiments. Therefore, it is recommended to record in each simulation the resulting loading pressure and impulse for the considered structural elements, especially in calculations that combine fluid and structures.

2.4. Load Characterisation. Blast waves are typically characterized by a compression phase, called overpressure (fast elevation of pressure above ambient pressure). This peak of overpressure is then followed by rarefaction waves inducing a negative phase during which the pressure falls below the ambient pressure. The compression phase starts with a strong increase in the pressure from the ambient pressure (p_0) to the peak pressure ($p_0 + p_{\max}$) within a timescale of microseconds. Figure 4 shows a simplified form of the pressure history of a blast wave and indicates the relevant parameters. Some more descriptions of the parameters are given in [22, 33, 34]. Of importance for the loading of glass windows is also the negative phase since this could be strong enough to pull fragments that were developed by the positive phase outwards, particularly in combination with rebound effects.

For a blast-loaded structure different loading conditions can be distinguished: impulsive, dynamic, and quasistatic loading (Figure 5). Loads with very short duration (relative to the structure's natural period) are known as impulsive loading, and in laminated glass windows they often result in a shear failure next to the border or at the boundary itself. Loads with longer duration (dynamic loading) tend to cause bending mode failures of glass panels. Only very slowly developed pressures (quasistatic loading) would be simulated by using a static load. For the structure under consideration these loading regimes can be schematically shown in the so-called PI (Pressure-Impulse) diagram (Figure 5).

3. Key Input Parameters for the Numerical Simulation of Glazing Systems under Blast

3.1. Model Discretisation. Model discretisation is based on the transformation of real structural components in a numerical

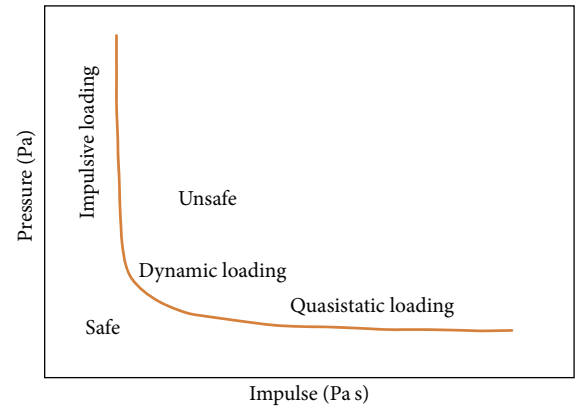


FIGURE 5: PI diagram: impulsive, dynamic, and quasistatic loading.

representation using finite elements. Elements are characterised by three main parameters:

- (i) Element type (and degrees of freedom).
- (ii) Number of nodes/element order.
- (iii) Integration.

Some of the element types that are used in a stress analysis are presented in Figure 6 [35]. One of the main differences between those element types is their geometry. Elements may also be distinguished between solid elements, shell, beam, and truss elements.

Depending on the software used to assess the structural model of the glass system under study, different element types are available and can be employed. The number of degrees of freedom is associated with the element type and is the fundamental variable calculated during the analysis. For stress/displacement simulations the degrees of freedom may be translational and, for shell, pipe, and beam elements, translational and rotational.

Elements may be implemented as linear (first-order) or quadratic (second order) elements depending the number of nodes. Quadratic elements give a higher accuracy but by using more nodes per element. As a rule, the increase of the element order improves the accuracy of the result for the same element size. However, the increase of the element order increases the CPU time (calculation time). Generally, first-order elements perform better concerning wave propagation.

Numerical methods are used to integrate various quantities over the volume of each element. Elements can often be used in full or reduced integration, a choice that can have a significant effect on the accuracy of the element for a given problem. Use of reduced integration can also decrease the needed CPU time. Reduced integration is mainly used in order to reduce the locking of the elements. This could result in hourglass modes that should be avoided.

In modelling a window panel or a facade, the following issues should be taken into consideration:

- (i) The geometrical shape of the window panel.
- (ii) The design of the structure (laminated, multilayered, etc.).

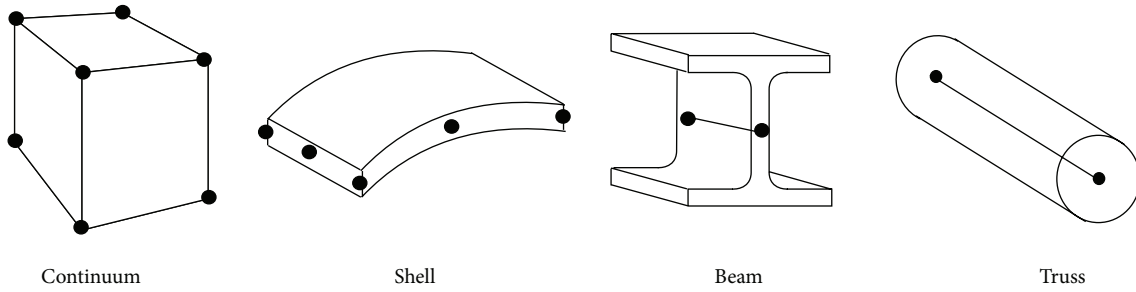


FIGURE 6: Some classical element types [35].

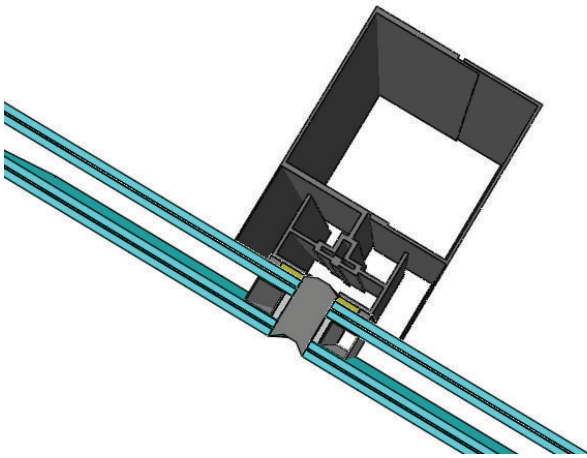


FIGURE 7: Detail of a facade system using laminated glass.

- (iii) The type of solver used to analyse the structure (explicit or implicit time integration).
- (iv) Type of damage studied (brittle failure, delamination, etc.).
- (v) Type of links between the structural components considered.
- (vi) Boundary conditions.

The model discretisation for laminated glass is quite challenging. Several options ranging from single shell elements up to 3D solid elements are presented by Larcher et al. [20]. Depending on the question, a balanced model between accuracy and calculation time should be chosen.

An example of an insulated laminated glass panel and its frame is given in Figure 7. Additional information about simulations of insulated glass facades is given in [36].

3.2. Material Models. The appropriate material models should be chosen to best represent the material behaviour under the examined loading conditions and in compatibility with the model discretisation described in Section 3.1. The mechanical calibration of all window components should be carried out, depending on the glazing system typology, by taking into account the specific damage constitutive behaviour and possible strain rate-dependent phenomena.

Material models for the simulation of laminated glass windows and facades are usually based on the following theories:

- (i) Linear behaviour with brittle failure limit (cracking).
- (ii) Theory of plasticity with plastic flow rule.
- (iii) Damage theory.
- (iv) Viscoelastic and viscoplastic theory.

The choice of an appropriate theory depends on the specific application, that is, on the purpose of the simulation. In general the material model should be as simple as possible but as comprehensive as needed. Complicated material models need many material parameters that are not always available and these models are in addition sometimes more difficult to check.

3.2.1. Glass. Glass is a typically brittle material. A linear elastic representation with failure or erosion criterion works well in most of the cases of technical interest. Sometimes, a plastic part is added in order to fade out the stress in a slower way and to also reduce numerical instability problems if such material model is not physical. The strain rate behaviour of glass is still not sufficiently investigated. First results show that the failure strength increases at very high strain rates [37]. Typical material parameter values for annealed as well as for tempered glass can be taken from [38, 39] and are given in Table 2.

3.2.2. Interlayers. The material model for the PVB interlayer strongly depends on the considered damage level. Its behaviour until the first glass cracking can be assumed to be elastic since the strain is still very small. A more accurate description of the behaviour of the interlayer becomes important especially when the glass is cracked. Also a plastic material law could, for example, represent the loading behaviour under higher strain rates quite well when the unloading behaviour of PVB becomes more viscoelastic. Some values for the interlayer material are given in [20] and in Table 2.

3.2.3. Adhesives and Structural Sealants Joints. Adhesive joints and structural sealants are usually introduced between the glass panels and the metal frames. Literature references are available for their mechanical characterisation, for example, from the producers. In general, adhesives and sealants

TABLE 2: Typical material properties for glass, PVB, and sealant.

Property	Annealed glass	Tempered glass	PVB	Sealant
Uncracked Young's modulus [Pa]	$7.0e + 10$	$7.0e + 10$	$2.2e + 8$	$1.8e + 5 - 6.2e + 5$
Poisson's ratio [—]	0.23	0.23	0.45	0.49
Elastic stress limit [Pa]	—	—	$11e + 6$	—
Density [kg/m^3]	2500	2500	1100	1000
Failure strain [—]	0.0012	0.00228	2.0	4–4.6
Failure stress [Pa]	$35e6 - 85e + 6$	$196e + 6$	$28e + 6$	$9.4e + 5 - 12e + 5$

of common use in structural glass applications are typically characterised by low modulus of elasticity, limited tensile/shear resistance, and large ultimate strain. The simplest numerical modelling approach for the mechanical description of structural sealants in tension takes the form of equivalent linear elastic materials with brittle behaviour [40]. Some material data for sealants can be taken from data sheets of producers [41–43].

3.2.4. Steel and Aluminium Components. The strain rate effect of aluminium is generally small while that of steel could be high. Depending on the structural configuration, the strain rates in the bearing construction could be smaller. Nevertheless, a Johnson-Cook material law [44] could represent the strain rate and temperature behaviour of many metallic materials. Examples are given in [31].

3.3. Boundary Conditions. For the analysis of the blast response of a glass window or facade, FE numerical models should be properly validated and assessed not only in terms of mechanical characterisation of materials but also by properly taking into account all the main influencing parameters.

Specifically, careful attention should be given to the numerical modelling of each window component (e.g., glass panel, metal framework, and possible adhesive joints between them) and the connection to the building structure [9, 20].

Both geometrically simplified models and computationally detailed models can be used, if properly validated for the specific case. An example of simplified models can be the description of a window in the form of 3D shell elements (glass panels), beam elements (metal frame), and mechanical point connectors (properly calibrated so that they could adequately reproduce the physical interaction between the glass panel and the frame). The same modelling approach can be extended to glazing systems in general, namely, consisting of curtain wall modular units, cable-net systems, and metal point connectors for the glass panels (Figure 8).

The appropriate numerical description of each window component should be suitably checked and validated against simple analytical models or experiments derived from small specimens/single facade components.

Before performing dynamic analyses on full 3D solid FE models, careful consideration should be given to the assessment of the correct description of adhesive joints and/or mechanical connectors. Regarding the boundary conditions of the FE models, the presence of special devices/connection systems or brackets between the glazing window and the structural system (e.g., the concrete slab of a building) should

be properly taken into account, so that the accuracy of the predicted effects due to the design blast load on glass as well as the maximum reaction forces transmitted to the substructure can be ensured.

3.4. Load Application. The numerical approaches can be divided into two main groups: coupled and uncoupled calculation approaches. A coupled approach may be needed in a case where the structure-fluid interaction is substantial, for example, in the case of a very flexible structure, isolated glass, fragment trajectories, and openings in the glass. In general, the loading definition is based on the TNT-equivalent method. In any case, the notion of TNT equivalent must be used carefully: the method for determining the TNT equivalent, the charge geometry, and the range of validity must be specified [46].

3.4.1. Uncoupled Approach. Pressure caused by blast waves can be calculated according to the theory of normal and oblique shock wave reflection, where the parameters of the spherical blast wave are estimated from empirical equations or diagrams (e.g., Kinney and Graham [23], Kingery and Bulmash [22]). These load functions can be employed if there are no alterations of the propagating blast wave between the detonation point and the studied structure (due to terrain anomalies, other obstructions, etc.). Clearly this method considers exclusively the dynamic behaviour of the structure (and not the surrounding air), and its advantage is the much lower computational cost.

3.4.2. Coupled Approach. More comprehensive explosion simulations use an Arbitrary Eulerian-Lagrangian (ALE) simulation scheme. In ALE the explosive and surrounding air are modelled using an Eulerian approach, typical in fluid mechanics. The behaviour of both gaseous materials is modelled using Equation-of-State (EOS) models that relate the pressure to the density of the material and internal energy. For air, this is typically the ideal gas law and for explosives, such as TNT, a Jones-Wilkins-Lee (JWL) model can be used [29]. The structure subjected to the blast loads is modelled using the traditional Lagrangian approach. The coupling between the Eulerian and Lagrangian elements is included, so that the solid Lagrangian structure occupies Eulerian space and pressures on the interface act as loads on the solid structure. In comparison to the uncoupled approach, the results may describe the blast propagation much better as soon as the elements are small enough. Especially, in case of multiple reflections, channelling or shadowing the coupled approach must

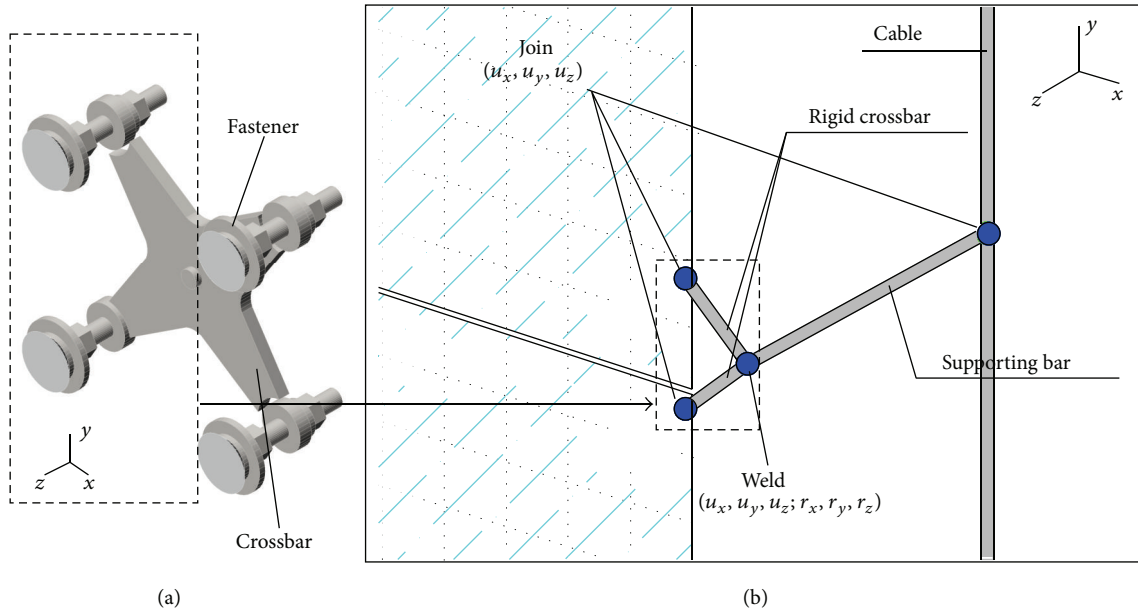


FIGURE 8: Example of point-supported glass panel. (a) Typical “spider” connector and (b) corresponding geometrically simplified FE model [45].

be used. The calculation time of this procedure is in general much longer since it depends on the detonation process that has a very short characteristic time.

3.5. Sensitivity Study for Essential Calculation Parameters. The topic of sensitivity study is broad and can cover a lot of aspects. This section focuses on some important parameters to be analysed such as

- (i) mesh size definition and shape of the elements,
- (ii) parameters for material modelling.

3.5.1. Mesh Size Definition and Shape of Element. Some recommendations have been written in [29, 31], and Table 3 presents typical parameters to be checked before and during the simulation. Most numerical codes provide their own quality checks that might help engineers to design the numerical model.

After the element quality check, a mesh sensitivity study should be performed by using models with different mesh refinement and comparing the main results, such as failure location and size, maximum deflection of the structure, and maximum strain (plastic strain) value. At least two different mesh refinements should give similar results in order to minimise mesh sensitivity.

Another way to guide the mesh generation is to evaluate where the highest stress values occur and then to verify that the mesh size is able to model the gradient of these stresses. If the gradient is too steep, it can generate a wrong estimation of maximum stress value. A general example of mesh convergence is given in [47].

An example of local discretisation is given below, representing a blast-loaded laminated glass plate similar to

the experiment of Kranzer et al. [18]. The simulation is done by using EUROPLEXUS [48] in the same way as proposed by Larcher et al. [20] using layered elements (linear) through the thickness. The glass plate is clamped between two steel frames, as defined by ISO 16933, where elastic stripes are placed between the steel frame and the glass. The element sizes, the number of elements, and the calculation time are given in Table 4. The results obtained (Figures 9 and 10) show that the coarsest mesh results in a different displacement history. This may be due to the extended boundary conditions for the coarsest mesh where the elastic stripe is wider. Only the finest mesh manages to represent the failure behaviour of the laminated glass as indicated by the experiment. The displacement history is also quite different for the finest mesh size in respect to the coarser mesh sizes, especially in the rebound phase.

3.5.2. Parameters for Material Modelling. The choice of a material model defines the number of input parameters. For example, for a purely elastic material (such as glass) with a stress limit, the material parameters needed for the analysis would be

- (i) Young’s modulus,
- (ii) Poisson’s ratio,
- (iii) density (due to dynamic structure response),
- (iv) stress elastic limit.

In many cases, the number of material parameters is much bigger. For example, the number of parameters for the Johnson-Cook plasticity model [44] (strain rate and temperature-dependent model including failure) is generally six.

TABLE 3: Mesh conformity recommendations for shell and solid elements (see also [16]).

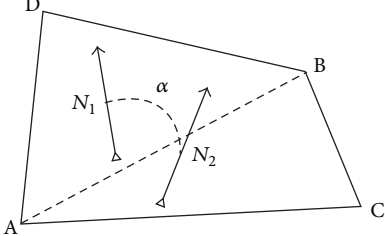
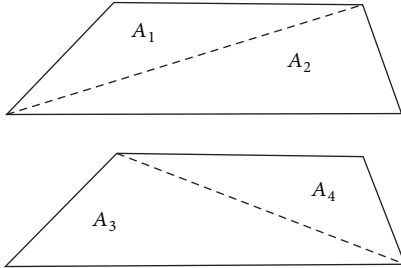
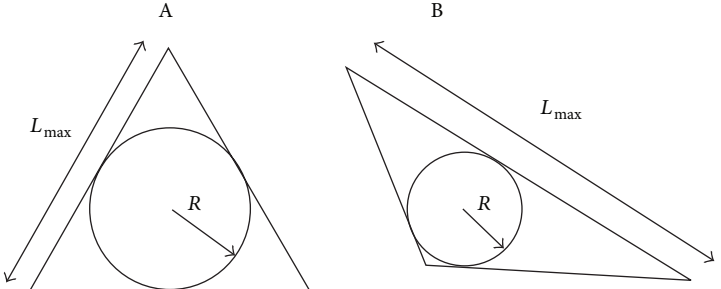
Mesh	Description
Mesh uniformity	It is admitted that mesh is as homogenous as possible; in case of mesh size modification, size of two adjacent elements should not differ more than 1.5 times (ratio of element size)
Minimum number of integration points through the thickness of a shell element	In case of linear material model, three integration points may be sufficient; in case of nonlinear deformation, number of integration points should be seven or more In case of layered structure, the number of integration points should follow previous rule per layer
Skewness measures the deviation of an element's angles α_i from 90° for quadrilateral elements and 60° for triangular elements	Quadrilateral: $\text{Skew} = \sum_{i=1}^4 (90 - \alpha_i)$ Triangular: $\text{Skew} = \sum_{i=1}^3 (60 - \alpha_i)$
Warp N_1, N_2 : perpendiculars to the element surface of the triangles by cutting the quadrilateral α : angle between the perpendiculars Measuring the deviation in an element face from a maximum allowable planar warp	
Taper A_i : areas of the triangles by cutting the quadrilateral $A_a = 0.25 \times (A_1 + A_2 + A_3 + A_4)$ $ (A_i - A_a)/A_a > 0.5$	
Aspect ratio should be chosen as it is defined for the element type	The ratio of the maximum element edge length to the minimum length (it might also be the thickness)
Stretch: (example for triangular element) Stretch = $(R/L_{\max})_{\text{actual}} * (L_{\max}/R)_{\text{target}}$ A: target, B: actual	

TABLE 4: Mesh sensitivity analysis for a blast-loaded laminated glass.

Element size [m]	Number of elements	Calculation time [s]
0.1	63	8
0.05	396	33
0.025	1280	233
0.0125	5120	1923
0.00625	20480	13821
0.003125	81920	95635

Typically, the more “advanced” the material model is, the more the input parameters needed are.

In order to evaluate the influence of each material parameter, it is useful to determine the degree of uncertainty of the value of the material parameter. Then, an option is to generate a sensitivity analysis on each material parameter in order to check its influence on the results.

Different mathematical approaches can be used in order to solve this type of problem. Based on an iterative process, several simulation codes provide a numerical approach to conduct this type of analysis (optimisation problem).

3.6. Failure, Fracture, and Erosion. As soon as the after-breakage behaviour must be modelled, the failure mechanisms of the glass, the interlayer, and the framing become important. The failure behaviour of glass is brittle. The failure

TABLE 5: Blast-loaded laminated glass experiments published in the open literature.

Source	Glass type/plies thickness	Panel size [m]	Blast wave source	Charge (equivalent) [kg]	Distance [m]	Failure
Morison et al. [17]	Float/3 mm	1.25×1.55	Solid explosive	60 TNT	12	Interlayer
Kranzer et al. [18]	Float/3 mm	1.1×0.9	Solid explosive/shock tube	0.5/0.25/0.125 PETN	5.75/3.7/2.0	Glass
Hooper et al. [19]	Float/3 mm	1.5×1.2	Solid explosive	15 C4	10/13	Interlayer
Morison et al. [17]	Float/3 mm	1.25×1.25	Shock tube	100/500 TNT	31/65	Interlayer
Larcher et al. [20]	Tempered/6 mm	1.1×0.9	Shock tube	820–4500	45–83	Glass/interlayer
Zhang and Hao [9]	Float/3 mm, 6 mm	1.5×1.2	Solid explosive	10/20	7.2–12.3	Glass/interlayer/boundary

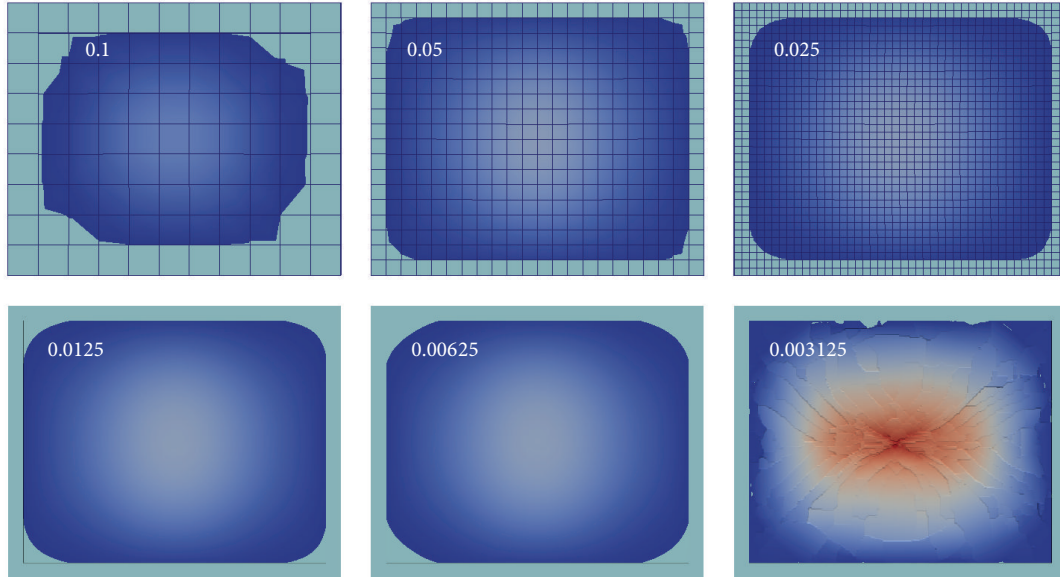


FIGURE 9: Displacement at 10 ms for different element sizes.

results in fracture of the material, and numerically several methods can be applied in order to describe such effect. Most appropriate in the explicit finite element method is the erosion. Elements where the failure criterion is reached are removed from the element table and are not any more considered in the calculation. The removed mass must be controlled or moved to the neighbouring elements. The crack width is defined by the element size and therefore either small elements must be used from the beginning of the simulation or additional element splitting methods or adaptivity [49] can be used. Other possibilities are given by the element-free Galerkin method or extended finite element method (XFEM) or direct splitting of the elements.

4. Validation and Assessment of Performance

4.1. Validation of Numerical Models. The numerical method and the material model should be validated by experimental data. This validation should include the following:

- (i) Basic material tests are, namely, intended for the proper mechanical characterisation of glass and the other window components (e.g., interlayers in presence of laminated glass and frames, adhesive joints, and mechanical connectors). Basic material testing would be appropriate even if this is in most cases neither possible nor cost efficient. Data from literature

TABLE 6: Hazard-rating criteria for arena tests according to ISO 16933:2007 [15].

Hazard rating	Hazard-rating description	Definition	Example of interpretation of numerical results
A	No break	The glazing is observed not to fracture and there is no visible damage to the glazing system	No failure in the glass; that is, there is elastic behaviour of the glass; some very small failed zones near the boundary conditions may occur
B	No hazard	The glazing is observed to fracture but the inner, rear face leaf is fully retained in the facility test frame or glazing system frame with no breach and no material is lost from the interior surface; outer leaves from the attack face may be sacrificed and may fall or be projected out	Both glass plies could fail in reaching their stress limit; small strains in the interlayer, no large plastic (permanent) deformation of the window at the end of the simulation (this way the delamination should be small)
C	Minimal hazard	The glazing is observed to fracture; outer leaves from the attack face may be sacrificed and may fall or be projected out; the inner, rear face leaf shall be substantially retained, with the total length of tears plus the total length of pull-out from the edge of the frame less than 50% of the glazing sight perimeter and so on	Both plies fail; failure of the interlayer; distinction between class C and the higher ones could perhaps be possible using the velocity of the fragments and their trajectories
D	Very low hazard	The glazing is observed to fracture and significant parts are located no further than 1 m behind the original location of the rear face; parts are projected at any distance from the attack face towards the blast source and so on	Both plies fail; failure of the interlayer; distinction between class C and the higher ones could perhaps be possible using the velocity of the fragments and their trajectories
E	Low hazard	The glazing is observed to fracture, and glazing fragments or the whole of the glazing falls between 1 m and 3 m behind the interior face of the specimen and not more than 0.5 m above the floor at the vertical witness panel and so on	Both plies fail; failure of the interlayer; distinction between class C and the higher ones could perhaps be possible using the velocity of the fragments and their trajectories
F	High hazard	Glazing is observed to fracture and there are more than 10 rateable perforations in the area of the vertical witness panel higher than 0.5 m above the floor, or there is one or more perforations in the same witness panel area with fragment penetration more than 12 mm	Both plies fail; failure of the interlayer; distinction between class C and the higher ones could perhaps be possible using the velocity of the fragments and their trajectories

or from the manufacturers of the products could replace the material tests.

- (ii) Structural tests: the individual glazing window components (glass pane, frame, and connectors), as well as their corresponding structural interaction, should be sufficiently validated.
- (iii) A mesh sensitivity study: it must be performed, as outlined above, in order to validate the model.

The objective of a nonlinear analysis is to simulate the structural behaviour and to determine the structural resistance. Such task can also be formulated as a prediction of the most probable resistance, which would then be the mean value of ultimate resistance. Therefore, the mean resistance is chosen as a reference for safety assessment by nonlinear analysis.

The uncertainty due to random variation of material properties (and possibly of other parameters of resistance) can be described by the random variation of resistance. In addition a model uncertainty must be included separately.

4.2. Examples for Validation Experiments from Literature. In order to validate numerical models experimental data are needed. Appropriate experiments are not often available in advance. Table 5 includes some sets of experiments, published in the open literature, which could be used for the model development and validation in this field.

4.3. Assessment of Performance. The interpretation of the results can be done in several ways. A damage parameter or failure limit together with an erosion criterion can identify

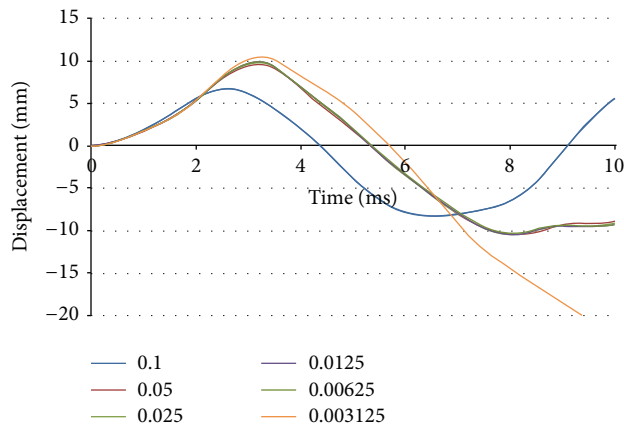


FIGURE 10: Displacement history for different mesh sizes, for a blast-loaded laminated glass, boundary condition according ISO 16933.

cracks in the glass, in the interlayer, or in the other structural components. A simulation resulting in a completely undamaged state can be identified as a full protection, without any glass splinters in the interior. Assuming a model that can represent the failure of the interlayer is available, for simulation resulting in an undamaged interlayer, it can be stated that the interior of the room is protected from major glass splinters. Also the window failure can be distinguished between shear failure near the window borders and bending failure in the middle of the pane. Finally, point connectors may have a different local failure mechanism. The interacting force between anchors/links and the surrounding structures should also be checked in order to avoid their failure.

4.4. Numerical Simulation Domains of Application regarding Actual Standards. Table 1 shows the hazard levels that are normally established experimentally. They represent in a way the formation and projection of splinters or fragments behind a laminated glass window. The fragmentation of laminated glass cannot yet be represented very well by numerical simulations. Therefore, with regard to hazard levels, numerical simulations can only be seen as a supplement to the experimental investigations.

Concerning specifically the hazard levels in ISO 16933:2007 [15], an idea of proposal for interpreting numerical simulation results and of corresponding them to the hazard levels A, B, and C can be drawn, as indicated in Table 6. Eventual developments of calculation methods and models should enable more reliable results and their assignment to higher hazard levels, too.

5. Conclusions

A review has been made on the abilities of numerical simulations to assess blast-loaded laminated glass windows and facades and to be used under certain circumstances to determine related hazard levels.

As emphasised, special attention should be given to the validation of numerical models, since the choice of loading

conditions, material parameters, and boundary configurations could have strong influence on the results. In particular, this review paper presents the first steps of an ongoing activity towards European standardization in that field. The next step would be to further elaborate these findings and discuss them with the responsible technical committees of the relevant EN and ISO standards.

Competing Interests

The authors declare that they have no competing interests.

Acknowledgments

The research leading to these results received funding from the European Union within the European Reference Network for the Critical Infrastructure Protection (ERNICIP) project hosted at the Joint Research Centre (JRC), European Commission, Via E. Fermi 2749, Ispra, Varese (VA), Italy.

References

- [1] H. S. Norville, N. Harvill, E. J. Conrath, S. Shariat, and S. Mallonee, "Glass-related injuries in Oklahoma City bombing," *Journal of Performance of Constructed Facilities*, vol. 13, no. 2, pp. 50–56, 1999.
- [2] M. Larcher, R. Forsberg, U. Björnstig, A. Holgersson, and G. Solomos, "Effectiveness of finite element modelling of damage and injuries for explosions inside trains," *Journal of Transportation Safety & Security*, vol. 8, supplement 1, pp. 83–100, 2015.
- [3] G. Balssa, G. Panofre, J. F. Hurstel, J. Bez, C. Capdevielle, and V. Sciortino, "Explosion de l'usine AZF de toulouse: description des lésions prises en charge au titre d'accident du travail par la Caisse primaire d'assurance maladie de la Haute-Garonne," *Archives des Maladies Professionnelles et de l'Environnement*, vol. 65, no. 6, pp. 463–469, 2004.
- [4] G. Valsamos, F. Casadei, M. Larcher, and G. Solomos, "Implementation of flying debris fatal risk calculation in EUROPLEXUS," Tech. Rep. JRC94805, Joint Research Centre, Publications Office of the European Union, Luxembourg, Luxembourg, 2015.
- [5] Johannesen, <https://www.flickr.com/photos/nhd-info/5980529033/in/photostream>.
- [6] R. Müller and M. Wagner, "Berechnung sprengwirkungshemmender Fenster- und Fassadenkonstruktionen," *Der Bauingenieur*, vol. 81, no. 11, pp. 475–487, 2008.
- [7] M. Timmel, S. Kolling, P. Osterrieder, and P. A. Du Bois, "A finite element model for impact simulation with laminated glass," *International Journal of Impact Engineering*, vol. 34, no. 8, pp. 1465–1478, 2007.
- [8] D. Sun, F. Andrieux, A. Ockewitz, H. Klamser, and J. Hogenmüller, "Modelling of the failure behaviour of wind-screens and component tests," in *Proceedings of the 5th European LS-DYNA Users Conference*, May 2005.
- [9] X. Zhang and H. Hao, "Fragmentation characteristics of tempered glass windows under air blast wave," in *Proceedings of the 3rd International Conference of Protective Structures (ICPS '15)*, Newcastle, Australia, 2015.
- [10] S. J. Bennison, A. Jagota, and C. A. Smith, "Fracture of glass/poly(vinyl butyral) (Butacite) laminates in biaxial flexure,"

- Journal of the American Ceramic Society*, vol. 82, no. 7, pp. 1761–1770, 1999.
- [11] H. D. Hidallana-Gamage, D. P. Thambiratnam, and N. J. Perera, “Design guidance for blast-resistant glazing,” *Journal of Architectural Engineering*, vol. 21, no. 3, Article ID 4015003, 2015.
 - [12] A. Burmeister, “Moderne fassaden-explosionsschutz,” in *Glas im konstruktiven Ingenieurbau*, Hochschule München, Munich, Germany, 2008.
 - [13] J. Pelfrene, J. Kuntsche, S. Van Dam, W. Van Paepegem, and J. Schneider, “Critical assessment of the post-breakage performance of blast loaded laminated glazing: experiments and simulations,” *International Journal of Impact Engineering*, vol. 88, pp. 61–71, 2016.
 - [14] X. Zhang, H. Hao, and G. Ma, “Parametric study of laminated glass window response to blast loads,” *Engineering Structures*, vol. 56, pp. 1707–1717, 2013.
 - [15] ISO 16933:2007/cor1, “Glass in building-explosion-resistant security glazing-test and classification for arena air-blast loading,” 2008.
 - [16] SDRC, *IDEAS Simulation: Finite Element Modelling User's Guide*, Siemens Product Lifecycle Management Software, 2014.
 - [17] C. Morison, M. Zobec, and A. Franceschet, “The measurement of PVB properties at high strain rates, and their application in the design of laminated glass under bomb blast,” in *Proceedings of the International Symposium on Interaction of the Effects of Munitions with Structures (ISIEMS '07)*, Orlando, Fla, USA, September 2007.
 - [18] C. Kranzer, G. Gürke, and C. Mayrhofer, “Testing of bomb resistant glazing systems. Experimental investigation of the time dependent deflection of blast loaded 7.5 mm laminated glass,” in *Proceedings of the Glass Processing Days*, Tampere, Finland, June 2005.
 - [19] P. Hooper, J. Dear, B. Blackman, D. Smith, D. Hadden, and R. Sukhram, “Strength of structural silicone glazing joints under blast loading,” in *Proceedings of the Department of Defense Explosives Safety Board Seminar*, Palm Springs, Calif, USA, August 2008.
 - [20] M. Larcher, G. Solomos, F. Casadei, and N. Gebbeken, “Experimental and numerical investigations of laminated glass subjected to blast loading,” *International Journal of Impact Engineering*, vol. 39, no. 1, pp. 42–50, 2012.
 - [21] NATO, *STANAG 2280: Design Threat Levels and Handover Procedures for Temporary Protective Structures*, NATO, 2008.
 - [22] C. N. Kingery and G. Bulmash, “Airblast parameters from TNT spherical air burst and hemispherical surface burst,” Tech. Rep. ARBRL-TR-02555, Defence Technical Information Center, Ballistic Research Laboratory (BRL) at Aberdeen Proving Ground, Maryland, Md, USA, 1984.
 - [23] G. F. Kinney and K. J. Graham, *Explosive Shocks in Air*, Springer, Berlin, Germany, 1985.
 - [24] United States Department of Defense, *Unified Facilities Criteria*, UFC 3-340-2, United States Department of Defense, Virginia, Va, USA, 2008.
 - [25] D. Bogosian, J. Ferritto, and Y. Shi, “Measuring uncertainty and conservatism in simplified blast models,” in *Proceedings of the 30th Explosives Safety Seminar*, Atlanta, Ga, USA, 2002.
 - [26] M. Larcher and F. Casadei, “Explosions in complex geometries—a comparison of several approaches,” *International Journal of Protective Structures*, vol. 1, no. 2, pp. 169–196, 2010.
 - [27] M. Larcher, A. Stolz, L. Rüdiger, and M. Steyerer, “Statische Ersatzlasten und ‘Ingenieurverfahren,’” in *BauProtect*, N. Gebbeken, K. Thoma, and M. Klaus, Eds., pp. 117–130, Universität der Bundeswehr München, 2012.
 - [28] K. Fischer and I. Häring, “SDOF response model parameters from dynamic blast loading experiments,” *Engineering Structures*, vol. 31, no. 8, pp. 1677–1686, 2009.
 - [29] A. van Doormaal, C. Haberacker, G. Hüsken et al., “Numerical simulations for classification of blast loaded laminated glass: possibilities, limitations and recommendations—ERNICIP Thematic Group: resistance of structures to explosion effects,” Tech. Rep. JRC94928, Publications Office of the European Union, 2014.
 - [30] US General Services Administration, “Standard test method for glazing and window systems subject to dynamic overpressure loadings,” Tech. Rep. GSA-TS01-2003, 2003.
 - [31] A. Stolz, A. van Doormaal, C. Haberacker et al., *Resistance of Structures to Explosion Effects: Review Report of Testing Methods ERNCIP Thematic Area Resistance of Structures to Explosion Effects. Deliverable D1*, Publications Office of the European Union, 2013.
 - [32] D. Hyde, “ConWep, US Army Waterways Experimental Station, US Army,” 1991.
 - [33] M. Larcher, “Pressure-time functions for the description of air blast waves,” Tech. Rep. JRC46829, Joint Research Centre, Ispra, Italy, 2008.
 - [34] V. Karlos, M. Larcher, and G. Solomos, “Analysis of the blast wave decay coefficient in the Friedlander equation using the Kingery-Bulmash data,” Tech. Rep. JRC94784, Joint Research Centre, Ispra, Italy, 2015.
 - [35] K.-J. Bathe, *Finite Element Procedures*, Prentice Hall, Englewood Cliffs, NJ, USA, 1996.
 - [36] R.-B. Deng and X.-L. Jin, “Numerical simulation for blast analysis of insulating glass in a curtain wall,” *International Journal for Computational Methods in Engineering Science and Mechanics*, vol. 11, no. 3, pp. 162–171, 2010.
 - [37] M. Peroni, G. Solomos, V. Pizzinato, and M. Larcher, “Experimental investigation of high strain-rate behaviour of glass,” *Applied Mechanics and Materials*, vol. 82, pp. 63–68, 2011.
 - [38] C. Morison, *The resistance of laminated glass to blast pressure loading and the coefficients for single degree of freedom analysis of laminated glass [Ph.D. thesis]*, Cranfield University, 2007.
 - [39] C. Louter and J. H. Nielsen, “Numerical analyses of the effect of SG-interlayer shear stiffness on the structural performance of reinforced glass beams,” in *Proceedings of the COST Action TU0905 Mid-Term Conference on Structural Glass*, pp. 405–412, April 2013.
 - [40] D. C. Weggel and B. J. Zapata, “Laminated glass curtain walls and laminated glass lites subjected to low-level blast loading,” *Journal of Structural Engineering*, vol. 134, no. 3, pp. 466–477, 2008.
 - [41] Dow Corning, “Product information Dow Corning 895, structural glazing sealant, one-part silicone rubber,” 2011.
 - [42] Bostik, “PrV-70 high strength structural glazing silicone adhesive sealant,” Technical Data Sheet, Bostik Australia, 2008.
 - [43] Henkel, “Pattex SL 690 solyplast-structural glass,” 2012.
 - [44] G. Johnson and W. Cook, “A constitutive model and data from metals subjected to large strains, high strain rates and high temperatures,” in *Proceedings of the 7th International Symposium on Ballistics*, The Hague, Netherlands, 1983.
 - [45] C. Amadio and C. Bedon, “Viscoelastic spider connectors for the mitigation of cable-supported façades subjected to air blast loading,” *Engineering Structures*, vol. 42, pp. 190–200, 2012.

- [46] P. M. Locking, "The trouble with TNT equivalence," in *Proceedings of the 26th International Symposium on Ballistics*, Miami, Fla, USA, 2011.
- [47] L. Champaney and L. Gendre, "Science de l'ingénieur: Raffinement du maillage et convergence," Tech. Rep., 2012.
- [48] Joint Research Centre and Commissariat à l'énergie Atomique et aux énergies Alternatives, EUROPLEXUS, <http://www-epx.cea.fr/>.
- [49] F. Casadei, M. Larcher, and G. Valsamos, "Adaptivity in shell/beam/bar elements in EUROPLEXUS," Tech. Rep. EUR 26697, JRC90456, Publications Office of the European Union, Luxembourg, Luxembourg, 2014.

Research Article

Advanced Concrete Model in Hydrocode to Simulate Concrete Structures under Blast Loading

Guo Hu,¹ Jun Wu,^{1,2} and Liang Li²

¹*School of Urban Railway Transportation, Shanghai University of Engineering Science, Shanghai 201620, China*

²*The Key Laboratory of Urban Security and Disaster Engineering, Ministry of Education, Beijing University of Technology, Beijing 100124, China*

Correspondence should be addressed to Jun Wu; cwewujun@163.com

Received 24 March 2016; Revised 10 May 2016; Accepted 23 May 2016

Academic Editor: Chiara Bedon

Copyright © 2016 Guo Hu et al. This is an open access article distributed under the Creative Commons Attribution License, which permits unrestricted use, distribution, and reproduction in any medium, provided the original work is properly cited.

The formulations of the advanced concrete RHT model adopted in AUTODYN are investigated and numerical studies are conducted to study the RHT model's actual performances under various loading conditions. It is found that using of default values in the RHT model is not able to simulate the realistic behavior of concrete under various loading conditions. Thus modified parameters in the RHT model are proposed to better capture the realistic behavior of concrete under such loading conditions. Furthermore, numerical simulation of normal concrete slabs and multilayer concrete slabs subjected to blast loading is conducted using AUTODYN with both the default and modified RHT parameters. Experimental readings from field blast tests are used to validate the numerical model developed. It is shown that the results from numerical simulations using the modified RHT parameters and the measurements from the field blast test agree well in terms of damage pattern, crater diameter, and acceleration. Hence, it can be concluded that the RHT model with modified parameters can capture the mechanical behavior of concrete structures well. The validated model can be further used to conduct a parametric study on the influence of key parameters (i.e., compressive strength, fracture energy, and thickness) on blast resistance of concrete structure.

1. Introduction

Around the world, one of the major construction materials used for both structural and infrastructural elements is concrete. At present, concerns about the safe living environment and the efficient protective structures and infrastructures are arising. The performance of concrete structures subjected to severe loading such as blast has been extensively studied in the last few decades [1–5]. Concrete is a brittle material which consists of cement paste, aggregates, and admixture (optional). The brittle behavior of concrete and other geomaterials, that is, rock and soil, presents obviously different strengths in compression and tension. Concrete also shows pressure hardening and strain hardening behavior under static loading, as well as strain rate hardening in tension and compression under dynamic loading before it fails. When concrete begins to fail, it gradually loses its loading carrying capacity, and this phenomenon is also called the strain softening [6].

Recently, dedicated research has been devoted to the development of reliable methods and algorithms to accurately analyze behaviors of structures and infrastructures subjected to dynamic loadings. Some techniques such as the explicit numerical analysis codes AUTODYN [7] and LSDYNA [8] are available for the modeling of interactive behavior between blast wave and concrete structures. In AUTODYN, different numerical techniques, such as pure Lagrangian and Lagrangian-Eulerian interaction algorithms, are available to analyze interactive response between the blast wave and concrete structure under blast loading [3, 9, 10].

There are many factors that will influence the reliability of numerical simulation. Among these factors, material model plays a key role because it reproduces the essential physical mechanisms of the material under various loading conditions. There are a number of material models for concrete developed in recent years, such as RHT model [1, 11], the Concrete Damaged Plasticity model (also known as MAT 72R3 model in LSDYNA) [11, 12], and HJC concrete model

[13, 14]. These robust material models are capable of capturing varying concrete material behaviors under different loading conditions. When subjected to dynamic loading such as blast loading or high impact loading, concrete shows highly nonlinear response. Besides, due to the general complexity of the constitutive models, the determination of the parameters (i.e., residual strength, failure strain, and failure criteria in model) also plays an important role in achieving the actual performance of the concrete materials. This requires sufficient understanding of the modeling formulation and the associated considerations.

In this paper, the formation of the RHT model in hydrocode AUTODYN is carefully evaluated and examined through the numerical tests by generating stress-strain relationships of concrete under various stress conditions. Some potential issues of the simulations using the present form of the RHT model are highlighted and discussed. Within the framework of its current formulation, modified RHT parameters are recommended which are able to reproduce more realistic postpeak softening behavior of concrete under tension and compression. Furthermore, the RHT model with both the default and the modified parameter sets is applied to simulate a series of physical tests on a concrete slab and a multilayer concrete slab under blast loading. The simulation results are compared with the experimental observations. The numerical simulation results using modified RHT model are also compared with those using the MAT 72R3 model in LSDYNA. Conclusions are then drawn on the basis of both the material model exploration and the simulations of concrete slab subjected to the blast loading.

2. RHT Concrete Model in AUTODYN

The RHT concrete model is an advanced plasticity model for brittle materials developed by Riedel et al. [1] from Ernst Mach Institute. This model takes into account some robust features, such as pressure hardening, strain hardening, strain rate hardening, strain softening, and third invariant dependence. In stress space, three pressure-dependent surfaces, elastic limit surface Y_{elastic} , failure surface Y_{failure} , and residual surface Y_{residual} (as shown in Figure 1), are implemented to model material hardening and softening responses properly. The key formation of these three surfaces is discussed in the following sections, and the detailed description of this model can be further referred to in [1, 10, 11].

2.1. Elastic Limit Surface and Prepeak Loading Surface. The elastic limit surface Y_{elastic} dominates the elastic stresses. With the increase in stresses, strain hardening takes place until the failure surface Y_{failure} is reached (as P_1 to P_2 in Figure 1). Y_{elastic} surface is obtained by scaling down from Y_{failure} surface, which can be expressed using the following equation:

$$Y_{\text{elastic}} = Y_{\text{failure}} \times F_{\text{elastic}} \times F_{\text{cap}}, \quad (1)$$

where the scaling factor F_{elastic} is the ratio of elastic tensile stress ($f_{t,\text{elastic}}$) or compressive stress ($f_{c,\text{elastic}}$) over the respective ultimate strength (f_t for ultimate tensile strength or f_c for ultimate compressive strength) along a radial path.

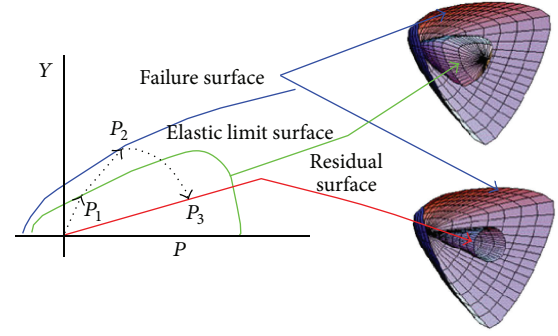


FIGURE 1: RHT three strength surfaces [1].

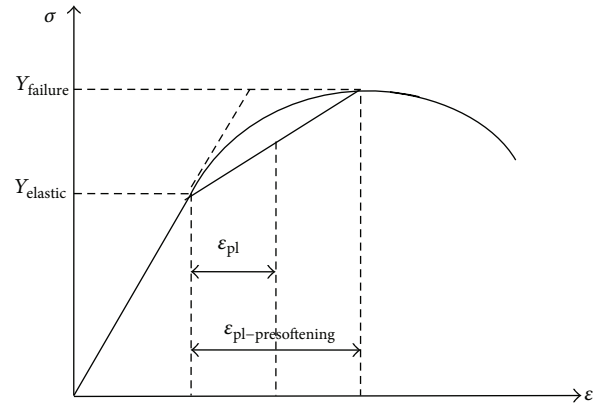


FIGURE 2: Bilinear strain hardening in RHT model [1].

Considering the fact that concrete initiates the inelastic behavior under tension at around 50~80% and under compression at about 30% of the respective maximum strength [10, 15], F_{elastic} in (1) varies linearly with pressure between the value related to uniaxial tension and that related to uniaxial compression [10]. The parabolic cap function F_{cap} is used to ensure the consistency between inelastic volumetric and deviatoric stresses [11].

The prepeak loading surface $Y_{\text{pre-peak}}$ is subsequently defined through interpolation between the elastic Y_{elastic} and failure surface Y_{failure} using the hardening slope. This can be seen in Figure 2 in the case of uniaxial compression, from which the equation can be expressed as

$$Y_{\text{pre-peak}} = Y_{\text{elastic}} + \frac{\epsilon_{\text{pl}}}{\epsilon_{\text{pl-presoftening}}} (Y_{\text{failure}} - Y_{\text{elastic}}), \quad (2)$$

where the definitions of ϵ_{pl} and $\epsilon_{\text{pl-presoftening}}$ are shown in Figure 2. From the figure, it is shown that ϵ_{pl} is the plastic strain before the failure strength; $\epsilon_{\text{pl-presoftening}}$ is the total plastic strain, and it can be determined by the secant modulus between the elastic limit surface and the failure surface.

2.2. Failure Surface. In the RHT model, the failure surface Y_{failure} can be expressed as a function of hydrostatic pressure p , Lode angle θ , and strain rate $\dot{\epsilon}$:

$$Y_{\text{failure}} = Y_{\text{TXC}}(p) \times R_3(\theta) \times F_{\text{rate}}(\dot{\epsilon}), \quad (3)$$

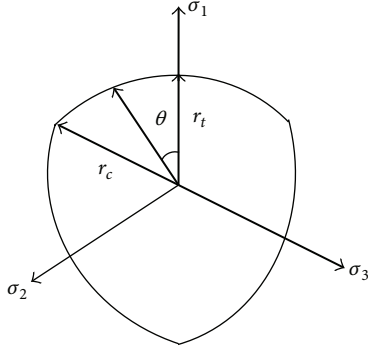


FIGURE 3: Typical deviatoric cross section of strength surfaces [10].

where $Y_{\text{TXC}}(p)$ represents the compressive meridian, and it can be expressed as

$$Y_{\text{TXC}}(p) = f_c \times \left(A \times \left(\frac{p}{f_c} - \text{HTL}^* \right)^N \right) \quad \text{for } p \geq \frac{f_c}{3}, \quad (4)$$

$$Y_{\text{TXC}}(p) = 0 \quad \text{for } \frac{p}{f_c} < \text{HTL}^*.$$

In (4), f_c denotes the uniaxial compressive strength of the material; A and N are two constant model parameters without dimension; HTL^* is the hydrotensile stress normalized by the compressive strength f_c ; $F_{\text{rate}}(\dot{\epsilon})$ represents the dynamic increase factor (DIF) as a function of the strain rate $\dot{\epsilon}$. Equation (3) indicates that the failure surface Y_{failure} is established via rotation of the compressive meridian around the hydrostatic axis. By multiplying $R_3(\theta)$ to the compressive meridian, the shear and tension meridians in the stress space can be taken into account in the failure surface. Thus, $R_3(\theta)$ can be written as [15]

$$R_3(\theta) = \frac{r}{r_c} = \frac{2(1 - \psi^2) \cos \theta + (2\psi - 1) \sqrt{4(1 - \psi^2) \cos^2 \theta + 5\psi^2 - 4\psi}}{4(1 - \psi^2) \cos^2 \theta + (1 - 2\psi)^2} \quad (5)$$

in which $\psi = r_t/r_c$ (refer to Figure 3). The Lode angle θ is a function of the second and third deviatoric stress invariants, and it can be obtained by

$$\cos 3\theta = \frac{3\sqrt{3}}{2} \frac{J_3}{J_2^{3/2}}. \quad (6)$$

Figure 3 illustrates a typical shape of the deviatoric section plane of a strength surface. It should be noticed that for the concrete material the deviatoric section typically transits from a triangular shape at a low pressure (brittle material) to a circular shape at a high pressure (ductile materials) [15].

2.3. Residual Surface and Postfailure Surface. In order to represent the strength of the completely crushed concrete

material, an independent residual strength surface is used in RHT model and can be expressed as [11]

$$Y_{\text{residual}} = f_c \times B \times \left(\frac{p}{f_c} \right)^{M_1}, \quad (7)$$

where B and M_1 are two constant parameters without dimension, and they can be determined from curve fitting of the experimental data. These two parameters (B and M_1) determine the residual strength of concrete material, which will be shown in the following section.

After failure is initiated, a damage model is used for strain softening which considers the gradual loss of the load carrying capacity of concrete after reaching its ultimate tensile or compressive strength. This postfailure surface Y_{fracture} can be achieved by linear interpolation from the failure surface Y_{failure} to the residual surface Y_{residual} (as P_2 to P_3 in Figure 1 and (8)) and incorporation of a damage factor D (see (9)). One has

$$Y_{\text{fracture}} = Y_{\text{failure}} + D \times (Y_{\text{failure}} - Y_{\text{residual}}), \quad (8)$$

where the damage parameter D is defined as [10]

$$D = \int_0^{\epsilon_p} \frac{d\epsilon_p}{D_1 (p^* - \text{HTL}^*)^{D_2}} \quad \text{for } D_1 (p^* - \text{HTL}^*)^{D_2} > e_{f\min} \quad (9)$$

$$D = \int_0^{\epsilon_p} \frac{d\epsilon_p}{e_{f\min}} \quad \text{for } D_1 (p^* - \text{HTL}^*)^{D_2} \leq e_{f\min}$$

in which $p^* = p/f_c$ is the normalized pressure variable and $d\epsilon_p$ is the plastic strain increment. From the equation, it can be observed that the damage factor D is dependent on the normalized pressure p^* , the shape parameters D_1 and D_2 , and minimum failure strain $e_{f\min}$ (in Section 3, $e_{f\min}$ is classified into two types: one is $e_{t,f\min}$ for minimum tensile failure strain and the other is $e_{c,f\min}$ for minimum compressive failure strain). A proper selection of parameters D_1 , D_2 , and $e_{f\min}$ is crucial in order to obtain a reasonable postpeak softening behavior of the concrete material. The default values of these three parameters in RHT model are found to be problematic in some cases [9, 10], and hence modifications will be proposed in the following section.

3. Numerical Test

To test the actual crack softening behavior of the RHT model in tension and compression, single element tests are conducted to evaluate stress-strain relationship of the element under various stress conditions. The detailed single element simulation approach can be found in [10].

3.1. Tension Softening. In the RHT model, the hydrotensile failure criteria are the default tension failure criteria which means if the value of the tensile stress in an element falls below a specified limit, tensile failure is assumed to occur. At the same time, the tensile failure strain is predefined in the

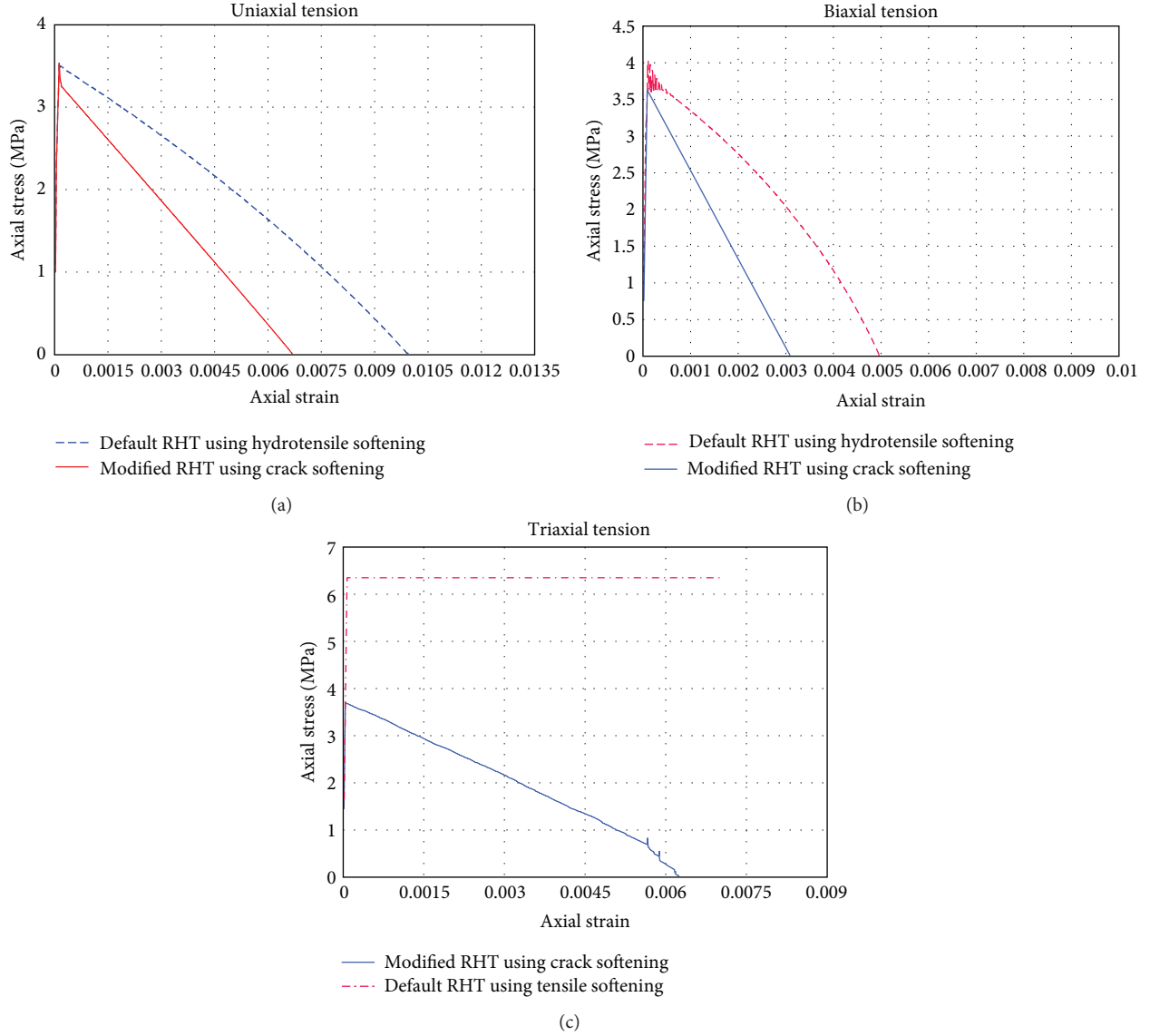


FIGURE 4: Comparison of tensile stress-strain curves generated by RHT model.

hydrotensile failure criteria (the default tensile failure strain $e_{t,fmin} = 0.01$), which indicates that the failure tensile stress and failure strain are not changed with varying element sizes, and hence the value of the fracture energy is greatly mesh-dependent. These phenomena can be clearly explained by (10) in AUTODYN [7]:

$$e_{t,fmin} = \frac{2 \times G_f}{\sigma_t \times L_{eq}}, \quad (10)$$

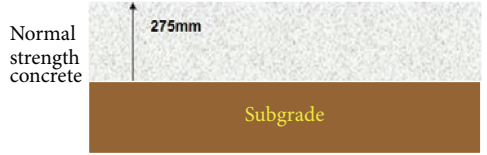
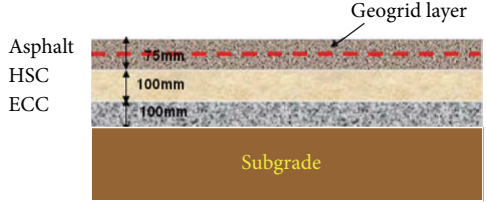
where $e_{t,fmin}$ is the tensile failure strain, σ_t is the tensile failure stress, G_f is the fracture energy, and L_{eq} is the characteristic length of the element. In AUTODYN 3D, L_{eq} is the diameter of a sphere having the same volume as the three-dimensional element [7].

In (10), it is obvious that, for given tensile failure strain and tensile failure stress, the fracture energy of a bigger element size could be larger than that of a smaller element

size. However, it is well known that the fracture energy is an important parameter for the simulation of tensile softening behavior of brittle material, and hence a fracture energy value is usually specified in the numerical model. In current study, the crack softening failure criteria [7, 17] are employed to model the tensile softening behavior with consideration of the fracture energy. The crack softening failure criteria adopt a linear softening law, in which, after the peak tensile stress σ_t , a constant strength degradation rate occurs with respect to the cracking strain. Hence the tensile failure stress (σ_t) and the fracture energy (G_f) are given as input parameters in the crack softening failure criteria. During the cracking process, the discrete crack width (w) is smeared out over a certain distance, which is normally equal to the characteristic length of the element L_{eq} . The crack strain can also be calculated by (10).

Figure 4 reports the simulation results of the single element under various stress conditions adopting the default

TABLE 1: Cross section of pavement slabs tested in field blast tests.

Test ID	Sample	Cross section
T1	Normal concrete slab	
T2	Multilayer concrete slab	

hydrotensile failure criteria and the crack softening failure criteria. After comparison between two failure criteria, it is found that using the default hydrotensile failure criteria tends to show an unrealistically descending process in the strain softening range for tension. For example, for a uniaxial tension test shown in Figure 4(a), the final failure strain is on the order of 0.01, which is more than one order of magnitude higher than the generally observed tensile failure strain from physical tests [15]. However, when adopting the crack softening failure criteria, the RHT model presents more realistic performance in the tensile failure strain under various stress conditions as shown in Figure 4. This modification is also more suitable for simulation of damage pattern of concrete materials under blast loading which will be shown in another application example in Section 4.

3.2. Compression Softening. Shear cracks usually appear after the yield limit is reached. Beyond the yield limit, the concrete exhibits softening behavior with yield stress and stiffness degradations. Such plastic behavior of concrete, to be more specific, the compression softening behavior, has to be considered into the constitutive model. Figure 5(a) shows that the concrete adopting the default RHT parameters possesses a higher residual strength of 21 MPa in the postpeak domain which is unreasonable in the low pressure regime. To make the concrete model more realistic, two steps have been taken to obtain reasonably the residual strength and the failure strain. Firstly, the residual yield stress should be changed [5]. From the formula of the residual surface, it is found that both B and M_1 control the final residual strength. After a few trials, the values for B and M_1 of 1.1 and 0.9, respectively, are proposed to replace the default values of 1.6 and 0.61, respectively. With such modification, the residual yield stress decreases significantly, and this improves the concrete material behavior in the low pressure regime. It is also observed that the compressive failure strain of concrete using the default RHT model parameters is around 0.01 as shown in Figure 4(a), which is much larger than the realistic value. Thus, the following step is used to adjust the compressive failure strain and the damage parameter D . Based on (9), it is found that compressive failure strain $e_{c,fmin}$ affects

the total failure strain under the lower pressure ($\leq (1/3)f_c$). Therefore, $e_{c,fmin}$ is adjusted to be 0.001 which gives a total strain value of around 0.1% in uniaxial compression and is more reasonable compared to the experimental results [6]. The damage parameter D controls the rate of accumulated damage. For the failure behavior under compression, the parameter D_1 controls the shape of the softening branch after the peak strength. In this study, D_1 is changed to 0.02 and D_2 remains unchanged based on numerical tests.

Figures 5(a) and 5(b) present the stress-strain curves of a single element in uniaxial and biaxial compressive tests based on numerical simulation using modified RHT parameters. It is observed that the material with the modified RHT parameters can properly reproduce the behavior of the concrete under both uniaxial and biaxial compressions. Figure 5(c) shows the stress-strain curve of the triaxial compression tests with different confinement pressures based on numerical simulation adopting the modified RHT parameters. It is observed that the peak strength is enhanced with the increase of the confinement. This represents a realistic behavior of concrete in triaxial compression as observed in experimental data [15].

4. Validation of the Modified RHT Model

In order to further investigate the applicability of the RHT model with modified parameters in the analysis of concrete structures under severe dynamic loading, the RHT model is used to simulate full scale field blast tests on a normal concrete slab and a multilayer concrete slab. The simulation results are then compared with the experimental observations. A brief introduction of the field blast tests of the normal concrete slab and the multilayer concrete slab is given below and more details can be found in [16].

4.1. Field Blast Test Configuration and Instrumentation. Two samples are tested in the field blast test, that is, one normal concrete slab sample and one multilayer concrete slab sample. The details of the cross sections of these two slabs are given in Table 1. The multilayer concrete slab is made of Asphalt Concrete (AC), High Strength Concrete (HSC), and

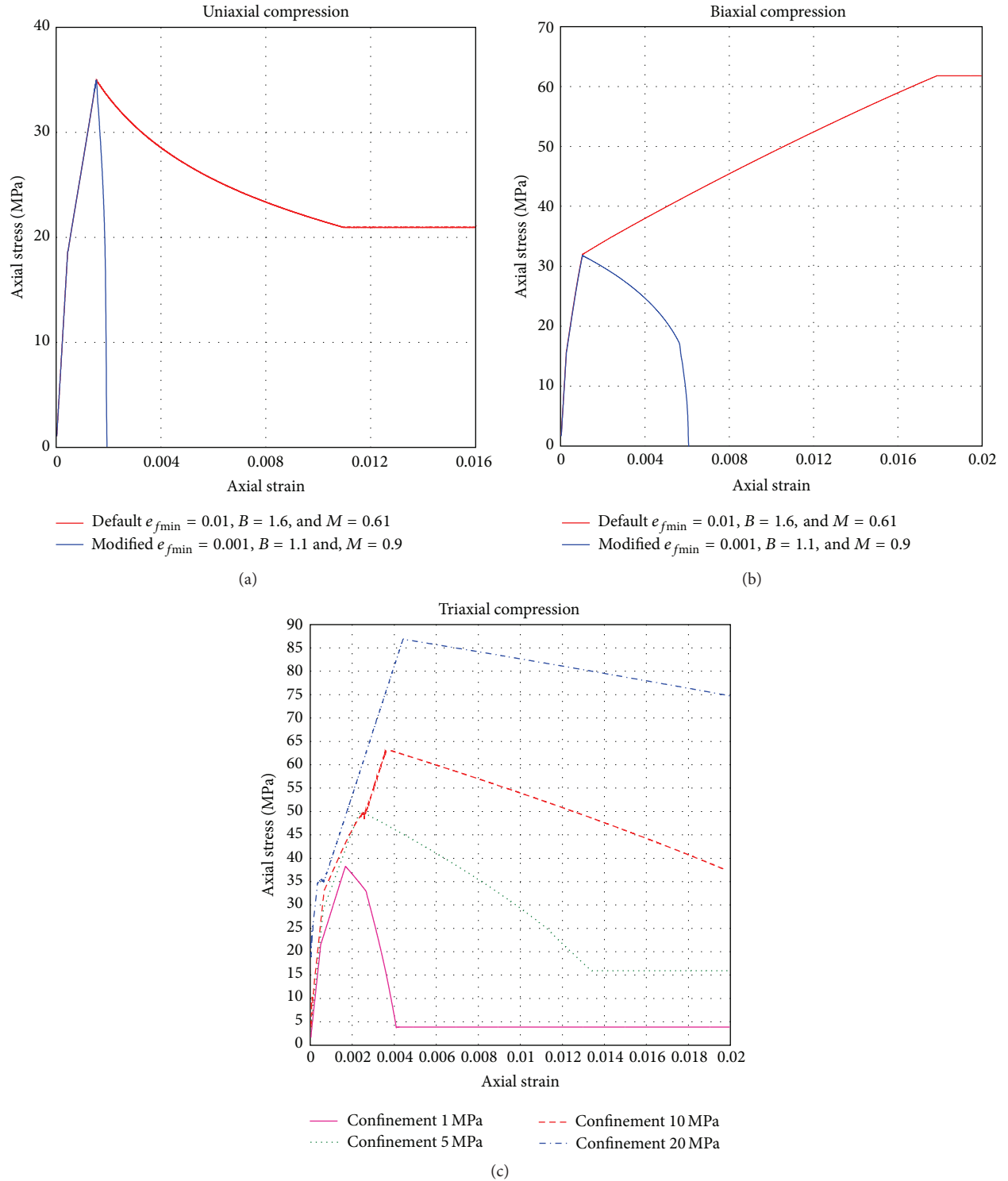


FIGURE 5: Comparison of compressive stress-strain curves generated by RHT model.

Engineered Cementitious Composites (ECC) from the top to bottom. Each slab is subjected to one blast detonation. A bomb equivalent to 7.3 kg TNT charge is placed with its center of gravity about 170 mm above the center of the slab surface. These two samples are cast at site with the dimension of 2.8 m in both length and width and 0.275 m in thickness.

Figure 6 shows the completed normal concrete slab and multilayer concrete slab with four anchors each. The anchors are used to fix the slab to the ground. Standard tests of material properties are conducted for each material cast, and the results are summarized in Table 2. The geogrid used to reinforce the AC layer in this study is the Polyfelt Microgrid

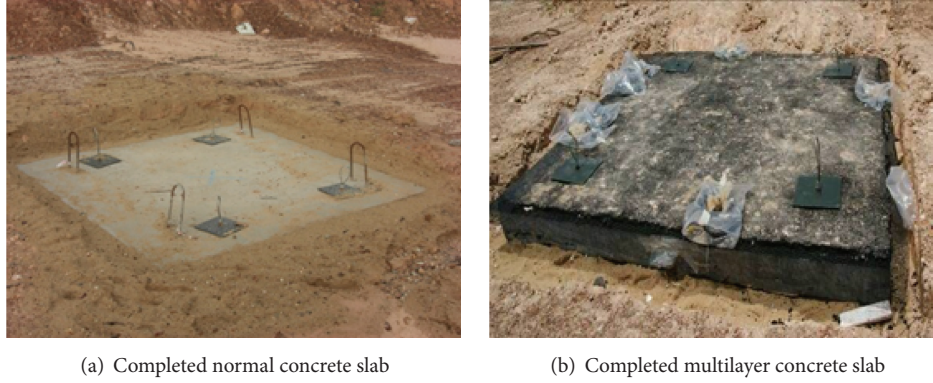


FIGURE 6: Normal concrete and multilayer slabs before blast tests.

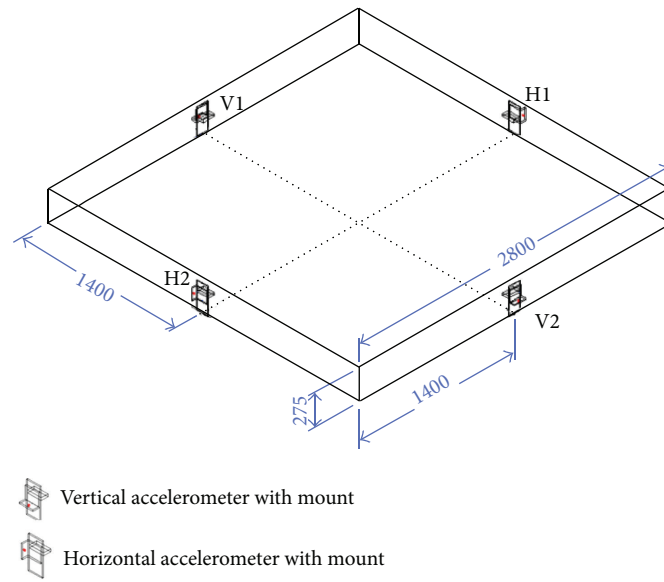


FIGURE 7: Layout of instrumentation for blast tests.

TABLE 2: Properties of materials cast for field blast test.

Material	Compressive strength (MPa)	Tensile strength (MPa)	Elastic modulus (GPa)	Poisson's ratio
Asphalt	4.6	0.7	0.598	0.35
HSC	55	4.35	33	0.20
ECC	64	5	18	0.22
Normal concrete	40	3.5	27	0.20

MG-100 with bidirectional tensile strength of 100 kN/m and it has an aperture size of 7 mm.

Various instruments are installed onto the slabs to measure the responses of the pavement slabs during the blast. Figure 7 shows the instrumentation installed on the slab. Four accelerometers are installed at the middle of each side of the slab to measure the vertical (V1 and V2 in Figure 7) and horizontal acceleration (H1 and H2 in Figure 7). The

accelerometers are mounted on steel frames casted together with the slab. The measurement results of the field blast tests will be discussed and compared with the numerical simulation results in the following section.

4.2. Validation 1: Normal Concrete Slab Subjected to Blast Load

4.2.1. Numerical Model. A 3D numerical model is established to model the normal concrete slab subjected to blast loading as shown in Figure 8. A quarter of the slab is modeled considering symmetry. In the model, the initial detonation and blast wave propagation are modeled using an axis-symmetric 2D model. Before the blast wave reaches the slab, the blast wave distribution is remapped into a 3D model. The foundation soil has a dimension of 825 mm in thickness and 2800 mm in length and width. Eight-node hexahedron Lagrange element with one-point gauss integration is used to represent the concrete slab and foundation soil. The interaction between the slab and foundation soil is considered using a contact algorithm. In AUTODYN, the penalty-based

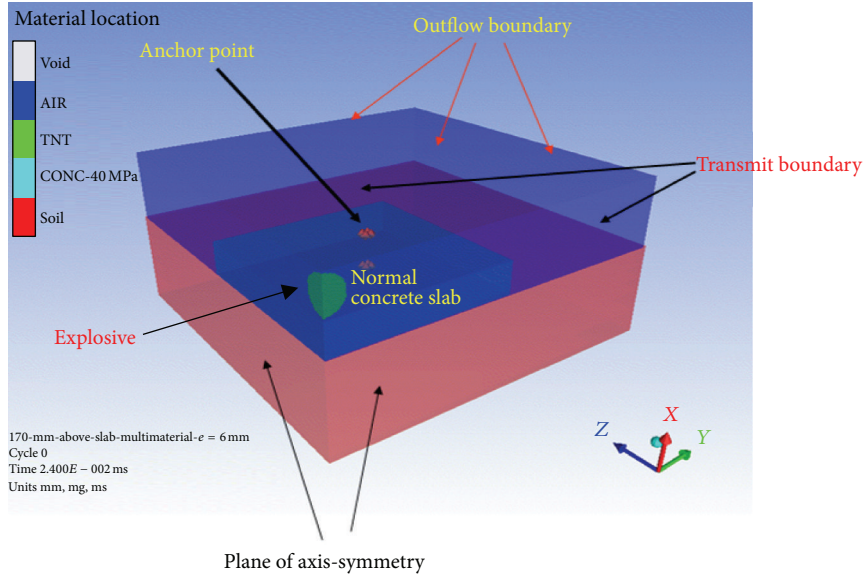


FIGURE 8: 3D numerical model of the normal concrete slab subjected to blast loading.

contact is used to detect the penetration between the “slave” surface and “master” surface. When a penetration is found, a force proportional to the penetration depth is then applied to resist the penetration. Thus the interface force could be calculated based on the elastic spring theory [7].

The air and blast waves are modeled using Euler elements. The blast loading acting on the concrete slab can be achieved by performing the interaction between the Lagrange elements and the Eulerian elements. The Lagrange elements apply geometric constraints on the Eulerian elements, while the Eulerian elements provide a pressure boundary to the Lagrange elements. In order to make Lagrangian and Eulerian elements interact effectively, it is important for the Eulerian element size to be equal to or smaller than the Lagrangian element size. Hence, mesh convergence analysis using the sizes of 9 mm, 8 mm, 7 mm, and 6 mm and 5 mm, 4 mm, and 3 mm for Eulerian elements is performed in current study. The size of Lagrangian elements is fixed to be 10 mm for the convergence study. Note that 3 mm is the smallest possible size for Euler elements using the computer resource available. During the convergence study, the pressure and impulse exerted on the center part of the slab are monitored and compared. After the convergence study, it is found that the size of 4 mm for Eulerian elements and 10 mm for the Lagrangian elements in current model is preferred considering the optimum CPU time and computer resource.

The boundary condition for air is outflow which allows the air to flow out. For the foundation soil, transmit condition is employed to simulate the semi-infinite space. The anchors on the slab are simulated as fixed points in the 3D model. The RHT model with modified parameters is employed to simulate the concrete slab subjected to blast loading, and an elastic-plastic Drucker-Prager model [15] is employed to simulate the foundation soil. The parameters of the air, foundation soil, and normal concrete are given in Tables 3–5, respectively.

TABLE 3: Air parameter.

Parameter	Value
Equation of state (EOS)	Ideal gas
Adiabatic exponent r	1.4
Density ρ (g/cm ³)	1.225×10^{-3}
Initial conditions (ref. energy mJ/mg)	12.068×10^{-3}

TABLE 4: Parameter of foundation soil.

Parameter	Value
Density (g/cm ³)	2.1
Bulk modulus (MPa)	166
Shear modulus (MPa)	77
Poisson's ratio	0.3
Yield stress (MPa)	0.766
Friction angle (°)	26

4.2.2. Results and Discussion. Figures 9(a) and 9(b) show the damage patterns of the concrete slab in the numerical model using default parameters and those using the modified RHT parameters in comparison with those in the field blast test as shown in Figure 9(c). Much smaller craters and less severe damage cracks are observed in the numerical simulation using the default RHT parameters than those observed after the field test. Such findings indicate that using the default RHT parameters could largely underestimate the damage pattern of the concrete slab under blast loading in terms of the cracks and the crater diameter. The concrete slab simulated using default RHT parameters appears to behave in a substantially ductile manner. This echoes the findings in the single element tests using the RHT model with the default parameter values. When adopting the modified RHT parameters, the damage and failure models of the concrete

TABLE 5: Parameters of normal concrete in the RHT model.

Parameter	Value
Compressive strength, f_c (kPa)	$4.000e + 04$
Shear modulus, G (kPa)	$1.670e + 07$
Tensile strength (f_t/f_c)	$1.000e - 01$
Shear strength (f_s/f_c)	$1.800e - 01$
Damage constant, D_1	$2.000e - 02$
Damage constant, D_2	$1.000e + 00$
Minimum strain to failure, $e_{c,fmin}$	$1.000e - 03$
Residual shear modulus fraction	$1.300e - 01$
Tensile failure	Principal stress
Tensile failure stress (kPa)	$4.00e + 03$
Fracture energy (J/m^2)	80
Crack softening	Yes

TABLE 6: Acceleration reading from field test and numerical model for normal concrete slab.

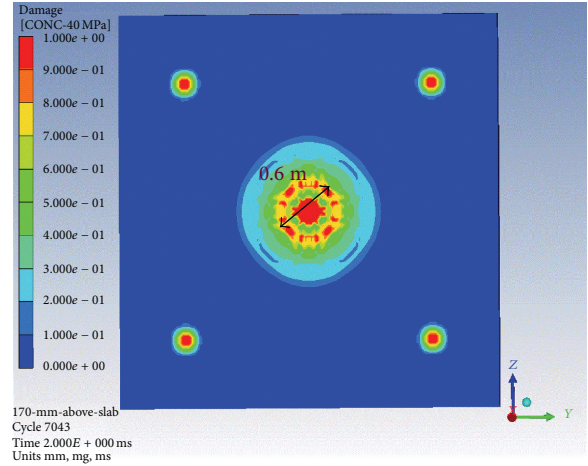
	Field test	Numerical model	Deviation from field test
Max. vertical acceleration (m/s^2)	22,820	24,382	6.8%
Max. horizontal acceleration (m/s^2)	14,820 60,450 *Not perfectly symmetrical	44,843	—

*Max. horizontal acceleration.

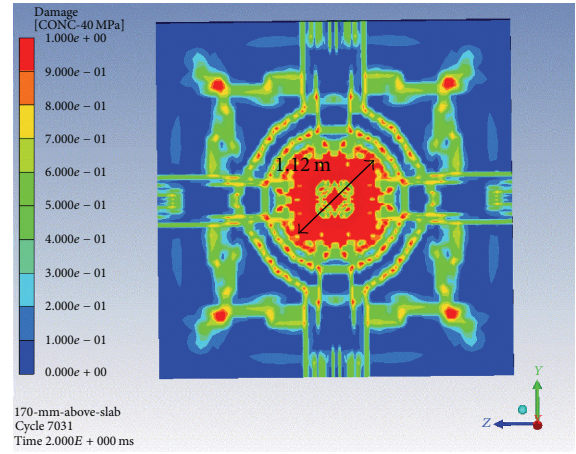
slab in the numerical analysis are comparable with the experimental results in terms of the crater diameter and the crack pattern as shown in Figures 9(b) and 9(c).

The damage pattern of the normal concrete slab simulated using the modified RHT parameters is then compared with that using MAT 72R3 model in LSDYNA [8]. The detailed numerical model using the MAT 72R3 material model in LSDYNA can be referred to in [16]. Numerical simulation results using the MAT 72R3 model are given in Figure 10. Figures 9(b) and 10 indicate that the damage patterns of the concrete slab simulated using both material models are almost the same. However, the crater diameter predicted by the MAT 72R3 model is smaller than that by the modified RHT model and that observed after the field blast test. This is possible that different blast simulation method and different mesh sizes are adopted for the numerical model in LSDYNA. Considering that there are 20 parameters that need to be determined in the MAT 72R3 model which makes it time consuming to establish a reliable numerical model, the RHT model with modified parameters is more suitable for the simulation of concrete structures under blast loading for quick damaged assessment.

Table 6 reports the results of vertical and horizontal acceleration of the concrete slab obtained from both the field measurement and numerical model. It is found that the variation of the vertical acceleration between the values from the field test and numerical simulation is around 6.8%, and the numerical simulation predicts a higher vertical acceleration



(a) Damage pattern with default RHT model



(b) Damage pattern with modified RHT model



(c) Physical damage of normal concrete slab after blast event

FIGURE 9: Damaged situations for normal concrete slab after blast loading.

than the value measured in the field blast test. However, in view of the inherent variation in the field blast tests, a prediction of 6.8% deviation of the numerical simulation results from field blast test results can be considered as acceptable. For the horizontal acceleration, two different readings were obtained from the accelerometers because the

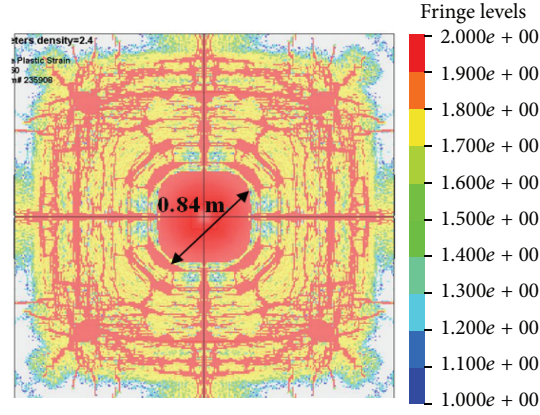


FIGURE 10: Damaged pattern of normal concrete slab using MAT 72R3 model [16].

TABLE 7: Parameter of asphalt material using Drucker-Prager model.

Parameter	Value
Density (g/cm^3)	2.3
Bulk modulus (MPa)	770
Shear modulus (MPa)	259
Poisson's ratio	0.35
Yield stress (MPa)	4.6
Friction angle ($^\circ$)	38

charge is not perfectly placed at the center above the slab. It can be observed from the table that horizontal acceleration predicted in the numerical simulation is right the average of the two measured acceleration values.

4.3. Validation 2: Multilayer Concrete Slab Subjected to Blast Load

4.3.1. Numerical Model. The dimension and mesh size of multilayer concrete slab in numerical simulation are the same as those in the normal concrete slab. The parameters used for the air and foundation soil are the same as those given in Tables 1 and 2. The numerical model for the multilayer concrete slab is shown in Figure 11. The thickness of each material is consistent with that used in the field blast test as stated in Section 4.1, that is, 100 mm for the ECC layer, 100 mm for the HSC layer, and 75 mm for the reinforced asphalt layer. The boundary condition and the location of detonation are the same as those in the case for normal concrete slab model, which are detailed in Section 4.2.

Laboratory tests [18] indicate that the geogrid enhances tensile strength of a material if the geogrid is added. Thus, in current numerical model, the asphalt layer is modeled with greater stiffness and tension strength in order to take into account the inclusion of the geogrid. The parameters used for the asphalt material are given in Table 7. For High Strength Concrete (HSC), the approach of the RHT model with modified parameters is used to simulate the material with consideration of high compressive strength. The RHT model with modified parameters is also employed to simulate

TABLE 8: Parameters of HSC in the RHT model.

Parameter	Value
Compressive strength, f_c (kPa)	$5.500e+04$
Shear modulus, G (kPa)	$1.900e+07$
Tensile strength (f_t/f_c)	$1.000e-01$
Shear strength (f_s/f_c)	$1.800e-01$
Damage constant, D_1	$4.000e-02$
Damage constant, D_2	$1.000e+00$
Minimum strain to failure, $e_{c,fmin}$	$1.000e-02$
Residual shear modulus fraction	$1.300e-01$
Tensile failure	Principal stress
Tensile failure stress (kPa)	$5.50e+03$
Fracture energy (J/m^2)	150
Crack softening	Yes

TABLE 9: Parameters of ECC in the RHT model.

Parameter	Value
Compressive strength, f_c (kPa)	$6.400e+04$
Shear modulus, G (kPa)	$7.300e+06$
Tensile strength (f_t/f_c)	$1.000e-01$
Shear strength (f_s/f_c)	$1.800e-01$
Damage constant, D_1	$4.000e-02$
Damage constant, D_2	$1.000e+00$
Minimum strain to failure, $e_{c,fmin}$	$1.000e-02$
Residual shear modulus fraction	$1.300e-01$
Tensile failure	Principal stress
Tensile failure stress (kPa)	$7.00e+03$
Fracture energy (J/m^2)	4000
Crack softening	Yes

the ECC material with consideration of its high compressive strength and superior ductile property. The parameters of the HSC and ECC material are given in Tables 8 and 9, respectively.

4.3.2. Results and Discussion. The results of damage patterns of the multilayer concrete slab after the blast in the numerical simulations are shown in Figures 12(a) and 12(b).

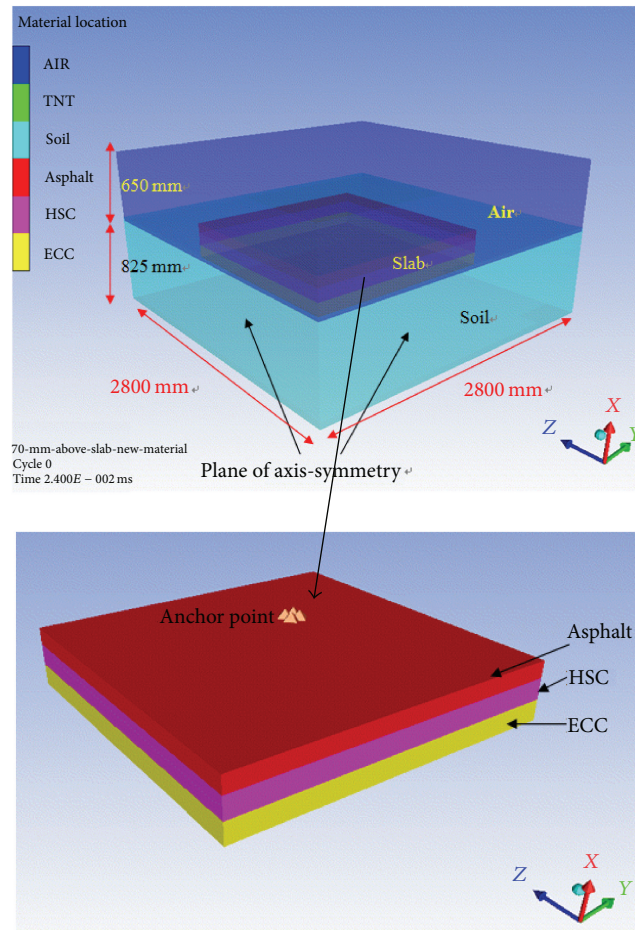


FIGURE 11: 3D numerical model of the multilayer concrete slab subjected to blast loading.

Figures 12(c) and 12(d) present the damage patterns after the field test. In the field test, the asphalt layer breaks into a few fragments after the blast, while in the numerical simulation, only a centralized crater is produced and no fragment is observed. This could be because the Drucker-Prager model may not be suitable for the simulation of fragmentation. Further, it should be noted that the AC layer is mainly destroyed by the combination of the high temperature and blast pressure as observed in the field blast test. An advanced material model for asphalt with consideration of the temperature effect should be explored in future study.

After removing the asphalt layer, the damage pattern of the HSC layer in the field test is shown in Figure 12(d). The damage pattern of the HSC layers in the numerical simulation is illustrated in Figure 12(b). The diameter of the crater is around 0.7 m in the field test, and it is 0.75 m in the numerical simulation. These two results are close to each other. The damage pattern of the HSC layer simulated using the modified RHT parameters is also compared with that using MAT 72R3 model in LSDYNA as shown in Figure 13 [16]. It is observed that the results from the simulations using both material models are comparable in terms of the damage pattern and crater diameter. Hence, the modified RHT model

TABLE 10: Acceleration from field test and numerical model for the multilayer concrete slab.

	Field test	Numerical model	Deviation from field test
Max. vertical acceleration (m/s^2)	35,400	33,518	5.3%
Max. horizontal acceleration (m/s^2)	18,690 36,640 *Not perfectly symmetrical	39,540	—

*Max. horizontal acceleration.

can represent the real behavior of the concrete slab under blast loading.

Table 10 reports the results of the vertical and horizontal acceleration of the multilayer concrete slab obtained from both the field measurement and numerical simulation. The vertical acceleration from the numerical simulation is quite close to that measured after the field test with a small deviation of 5.3%. The two horizontal acceleration readings

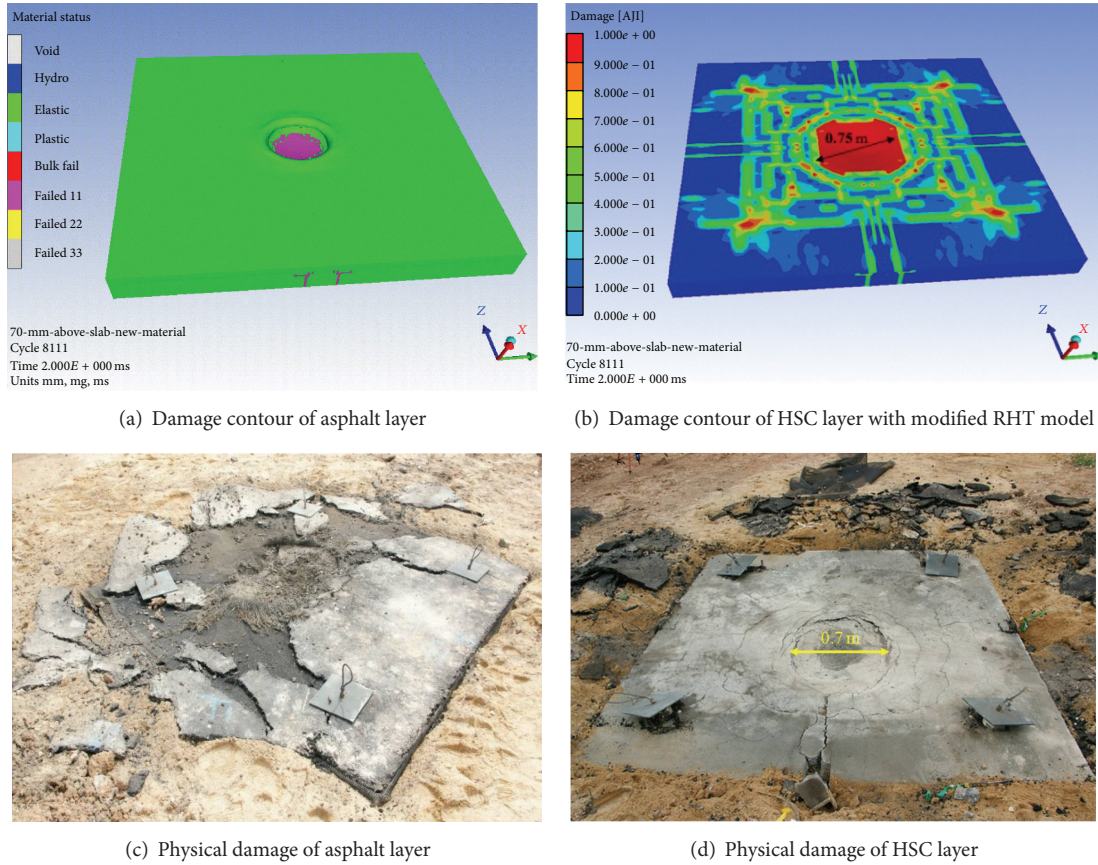


FIGURE 12: Damage pattern of multilayer concrete slab after blast loading.

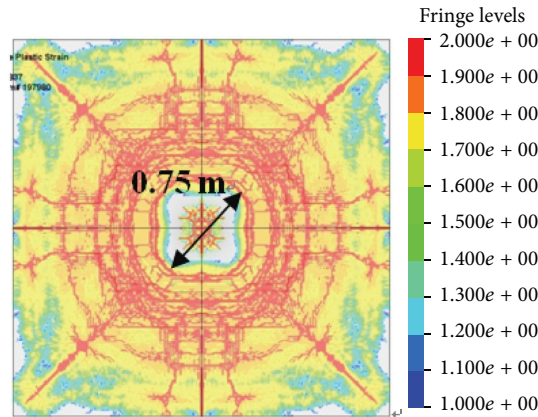


FIGURE 13: Damage pattern of HSC layer using MAT 72R3 model [16].

on two sides are not the same because the charge is not perfectly located at the center above the slab.

5. Conclusion

This paper intensively studies the equation of the RHT model in the hydrocode AUTODYN. It is found that using the default RHT parameters such as hydrotensile failure criteria, residual strength parameters, and failure strain cannot

predict the realistic behavior of concrete material under various loading conditions. Through numerical studies on behavior of concrete material in various loading conditions, the key parameters such as tensile failure criteria, residual strength parameters, and failure strain parameter controlling the behavior of concrete under uniaxial, biaxial, and triaxial tension/compression are discussed, and the modified RHT parameters are proposed to improve the model. Furthermore, numerical simulations of a concrete slab and a multilayer

concrete slab under blast loading are conducted using AUTODYN with both the default and modified RHT parameters. The numerical simulations are validated by field blast test. Based on the numerical simulations, the incorporation of the modified RHT parameters reproduces more realistic structural behavior under blast loading than that of the default RHT parameters. The results in numerical simulations using RHT model with modified parameters agree well with the corresponding field test results including the damage pattern, crater diameter, and acceleration readings. The numerical model using the RHT model with modified parameters is then compared with that of MAT 72R3 in LSDYNA for the normal concrete slab and multilayer concrete slab. It is observed that the predicted damage pattern and crater diameter using the RHT model with the modified parameter and using the MAT 72R3 model show a better comparison with the experimental result. Considering that 20 parameters are needed in MAT 72R3 model which makes it time consuming to establish the numerical model, the RHT model with modified parameters is preferred for the simulation of the concrete structure under blast loading for quick damaged assessment. Hence, it can be concluded that the current numerical model using AUTODYN with modified RHT model could represent more realistic behavior of concrete structures under blast loading. The numerical model developed in this paper can be further used to conduct a parametric study on the influence of key parameters (i.e., compressive strength, fracture energy, and thickness) on blast resistance of concrete structure.

Competing Interests

The authors declare that they have no competing interests.

Acknowledgments

Part of this research is sponsored by the Scientific Research Foundation for the Returned Overseas Chinese Scholars, State Education Ministry of China (Grant no. E262021514), Youth Teacher Training Scheme from Shanghai Education Committee (Grant no. ZZGCD15053), and foundation from Shanghai University of Engineering Science (Grant no. E10501140170).

References

- [1] W. Riedel, K. Thomaand, and S. Hiermaier, "Penetration of reinforced concrete by BETA-B-500-numerical analysis using a new macroscopic concrete model for hydrocodes," in *Proceedings of the 9th International Symposium on Interaction of the Effect Of Munitions with Structures*, pp. 315–322, Berlin, Germany, 1999.
- [2] P. F. Silva and B. Lu, "Improving the blast resistance capacity of RC slabs with innovative composite materials," *Composites Part B: Engineering*, vol. 38, no. 5-6, pp. 523–534, 2007.
- [3] X. Q. Zhou and H. Hao, "Numerical prediction of reinforced concrete exterior wall response to blast loading," *Advances in Structural Engineering*, vol. 11, no. 4, pp. 355–367, 2008.
- [4] W. Wang, D. Zhang, F. Lu, S.-C. Wang, and F. Tang, "Experimental study and numerical simulation of the damage mode of a square reinforced concrete slab under close-in explosion," *Engineering Failure Analysis*, vol. 27, pp. 41–51, 2013.
- [5] R. Castedo, P. Segarra, A. Alañon, L. M. Lopez, A. P. Santos, and J. A. Sanchidrian, "Air blast resistance of full-scale slabs with different compositions: numerical modeling and field validation," *International Journal of Impact Engineering*, vol. 86, pp. 145–156, 2015.
- [6] M. H. Zhang, M. S. H. Sharif, and G. Lu, "Impact resistance of high-strength fibre-reinforced concrete," *Magazine of Concrete Research*, vol. 59, no. 3, pp. 199–210, 2007.
- [7] AUTODYN, Century dynamics, theory manual, 2005.
- [8] LSDYNA, *LSDYNA Keyword User's Manual*, Livermore Software Technology Corporation (LSTC), 2007.
- [9] Z. Tu and Y. Lu, "Modifications of RHT material model for improved numerical simulation of dynamic response of concrete," *International Journal of Impact Engineering*, vol. 37, no. 10, pp. 1072–1082, 2010.
- [10] Z. Tu and Y. Lu, "Evaluation of typical concrete material models used in hydrocodes for high dynamic response simulations," *International Journal of Impact Engineering*, vol. 36, no. 1, pp. 132–146, 2009.
- [11] W. Riedel, N. Kawai, and K.-I. Kondo, "Numerical assessment for impact strength measurements in concrete materials," *International Journal of Impact Engineering*, vol. 36, no. 2, pp. 283–293, 2009.
- [12] L. J. Malvar, J. E. Crawford, and J. W. Wesevich, *A New Concrete Material Model for DYNA3D Release II: Shear Dilation and Directional Rate Enhancements*, Defense Nuclear Agency, Alexandria, Va, USA, 1996.
- [13] M. Polanco-Loria, O. S. Hopperstad, T. Børvik, and T. Berstad, "Numerical predictions of ballistic limits for concrete slabs using a modified version of the HJC concrete model," *International Journal of Impact Engineering*, vol. 35, no. 5, pp. 290–303, 2008.
- [14] T. J. Holmquist, G. R. Johnson, and W. H. Cook, "A computational constitutive model for concrete subjected to large strains, high strain rates, and high pressures," in *Proceedings of the 14th International Symposium on Ballistics*, pp. 591–600, Quebec, Canada, 1993.
- [15] W. F. Chen, *Plasticity in Reinforced Concrete*, McGraw-Hill, New York, NY, USA, 1982.
- [16] J. Wu and S. H. Chew, "Field performance and numerical modeling of multi-layer pavement system subject to blast load," *Construction and Building Materials*, vol. 52, pp. 177–188, 2014.
- [17] R. Clegg, C. Hayhurst, and I. Robertson, "Development and application of Rankine plasticity model for improved prediction of tensile cracking in ceramic and concrete materials under impact," in *Proceedings of the 14th DYMAT Technical Meeting*, pp. 110–118, Sevilla, Spain, 2002.
- [18] J. Wu and X. M. Liu, "Performance of Soft-Hard-Soft (SHS) cement based composite subjected to blast loading with consideration of interface properties," *Frontiers of Structural and Civil Engineering*, vol. 9, no. 3, pp. 323–340, 2015.